Unterschrift des Betreuers

TECHNISCHE UNIVERSITÄT WIEN
Vienna University of Technology

DIPLOMARBEIT

Modeling of the β^+ activity distributions during particle therapy using Monte Carlo methods

Ausgeführt am
Atominstitut
der Technischen Universität Wien

**unter der Anleitung von Univ. Prof. Dr. DI Dietmar Georg
und Ko-Betreuung von DI Hermann Fuchs, PhD
und Mag. Peter Kuess, PhD**

durch
Merim Ćato, BSc
Siegfried-Freiberggasse 10b
2700 Wiener Neustadt

07. Dezember 2017

_____
Unterschrift Student

CONTENT

ACKNOWLEDGEMENTS

ABSTRACT

The verification of the delivered dose during or shortly after particle therapy (PT) with positron emission tomography (PET) is an (practical) approach for in vivo dosimetry [1]. PET imaging is based on the detection of positron-electron annihilation photons. Irradiated tissue during PT leads to nuclear reactions and the production of β^+–emitting radionuclides, creating a 3D activity distribution map. For therapy monitoring, the measured and a predicted activity distribution are compared. Monte Carlo (MC) simulations can accurately describe particle transport and interactions with matter in complex geometries, which makes them an important tool for calculated β^+ activity distributions. In research and clinical studies it is used to develop novel techniques for range verifications in vivo. The open-source simulation platform GATE (Geant4 Application for Tomographic Emission), which encloses the MC based framework Geant4 as well as the computational power, made it feasible to perform complex simulations with patient data.

The accuracy of the simulations strongly depends on the parameter definitions, e.g. physics models definitions, interaction and output properties. In this thesis the influence of simulation parameters e.g. step size, Houndsfield unit (HU) scale, data storage actor and primary particle numbers on the dose and β^+–activity distributions is presented.

The evaluation of the suitable physics model was performed by testing 16 different physic lists. In a simulation a $100 \times 100 \times 400$ mm³ Polymethylmethacrylat (PMMA) phantom was irradiated with a proton beam of 10^6 particles at 110, 140 and 175 MeV, and the data were stored using the *ProductionAndStopping* actor.

The results obtained from the simulations with different physics lists were compared with the experimental results from literature [2]. The most compliant physics list was QGSP_BIC_HP, for all positron emitters and at all energies.

The performed statistical analysis with 0.1 mm and 0.01 mm step size distances revealed a reduction of the uncertainty with increasing primary particle numbers for both step sizes. A reduction from ~7% with 10^5 primary particles to ~2% with 10^6 primary particles per beam, was observed for the 0.1 mm step size simulations. For the 0.01 mm step size

setups, similar but slightly higher results were achieved. Simulations performed with 10^8 primary particles lead to the expected conclusion that the fluctuations of produced positron emitters would decrease compared to lower proton quantities. Resulting from the tendency of reducing statistical uncertainty with increasing primary particle numbers, the variances would be below 2%. Due to longer simulation times and the higher variances for produced positron emitter distributions, the decision felt for 0.1 mm step size. In terms of maximum number of primary particles for complex TP simulations, the highest performed quantity was used, namely 10^8.

Homogenous phantoms (90 × 90 × 300 mm³) were irradiated with a proton beam containing 10^7 particles at 140 MeV. Two different phantom setups were used to evaluate the range uncertainties influenced by the storage actors, namely *ProductionAndStopping* and *CrossSectionProduction* actor. Furthermore, the phantoms consisted of different insert materials with varying thickness, to investigate the behaviour of those actors and the range uncertainties of the produced ^{11}C and ^{15}O particles. Due to the low number of produced ^{10}C particles, the positron emitter was not evaluated.

The comparison of the behaviour of the storage actors, resulted in a favouring of the *CrossSectionProduction* actor over the *ProductionAndStopping* actor. The range uncertainty of the R_{50} distance of produced positron emitters could be visually evaluated for any insert thicknesses. For the *ProductionAndStopping* actor the visual range differences for the R_{50} distance of produced positron emitters were approximately 1 mm. Additionally, the latter actor revealed a relatively higher increment in produced particles in the maximum region.

Two HU tables with different greyscale subdivisions were explored, namely the HU scale from the TP system RayStation and the default HU scale from GATE. The R_{80} and R_{50} values, were compared with the calculated TP in order to analyse the range uncertainties in distal and lateral direction of the beam.

The evaluated R_{80} and R_{50} values in lateral and distal direction of the beam, in relation to the depth dose distribution, were below 3 mm. Other publications like Parodi et.al. and Knopf et.al., revealed deviations of approximately 1–3mm [3] [4] [5] [6]. The HU scale

vi

from the TP system Raystation, compared to the HU scale from GATE, showed lower deviations. In distal and lateral direction the range uncertainty was approximately 0.5 mm lower. This states that HU scales with a greater greyscale subdivision produces more accurate results.

With the final simulation parameters, dose and activity distributions of an irradiated prostate case were visually compared with the calculated TP and the literature. Similarities for the activity distributions were found, but also irregularities, resulting from the export of the Digital Imaging and Communications in Medicine (DICOM) files with RayStation to GATE.

In conclusion the improvement of MC simulations has the potential in PT-PET to increase the prediction and verification of beam applications with β^+–activity distributions in clinical based ion beam therapy. Further simulations are necessary to investigate the behaviour and influence of different simulation parameters in GATE on the reliability of the simulations.

ZUSAMMENFASSUNG

Der Nachweis der abgegebenen Dosis während oder kurz nach der Teilchentherapie (Particle therapy, PT) durch Positron Emission Tomographie (PET), ist eine (praktische) Anwendung in vivo Dosimetrie [1]. PET basiert auf dem Prinzip der Detektion von Photonen die durch die Annihilation von Positron-Elektronen erzeugt wurden. Das durch die Teilchentherapie bestrahlte Gewebe führt zu Nuklearreaktionen und zur Produktion von β^+–emittierenden Radionukliden, welches man als 3D Aktivitätsverteilung messen kann. In der Therapiekontrolle wird die mit dem PET gemessene Aktivitätsverteilung mit einer zuvor berechneten Aktivitätsverteilung verglichen. Monte Carlo (MC) Simulationen sind in der Lage in komplexen Strukturen den Teilchentransport und Interaktionen mit dem Gewebe zu berechnen, weswegen sie ein wesentliches Instrument für die Berechnung der β^+–Aktivitätsverteilung sind. MC Simulationen werden in der Radioonkologie, der Forschung und in klinischen Studien verwendet um neue Techniken für die Reichweitenverifikation in vivo zu entwickeln. Die open-source Simulationsplattform GATE (Geant4 Application for Tomographic Emission), welches das Grundkonzept Geant4, basierend auf MC einschließt, ermöglicht es komplexe Simulationen von Patienten durchzuführen.

Die Genauigkeit der Simulationen hängt von den gewählten Parametern ab. Einige dieser Parameter sind, z.B. Physikalische Modelle, Wechselwirkungsdefinitionen und Ausgabeeigenschaften. Der Einfluss von Simulationsparametern wie Hounsfield Einheit (HE, Engl. Hounsfield Unit, HU), Datenspeicherung der produzierten Teilchen (actor), Wechselwirkungsreichweite (step size) und die Anzahl der Primärteilchen, auf die Dosis und die β^+–Aktivitätsverteilung.

Für die endgültige Bestimmung der korrekten Physikliste war es notwendig 16 verschiedene Physiklisten zu analysieren. Die Simulation bestand aus einem 100 mm × 100 mm × 400 mm³ Polymethylmethacrylat (PMMA) Phantom und wurde mit 10^6 Protonen bestrahlt. Die Resultate wurden mit dem *ProductionAndStopping* actor erfasst.

Die Ergebnisse wurden mit der Literatur verglichen und dadurch ergab sich die

Erkenntnis, dass die QGSP_BIC_HP Physikliste für alle Positron-Emitter und Energien die größte Übereinstimmung erreichte [2].

Die statistische Auswertung der zwei step size Reichweiten, 0.1 mm und 0.01 mm, ergab bei steigender Primärteilchen Anzahl eine Reduktion der statistischen Unsicherheit. Für die 0.1 mm step size Simulationen wurde eine Unsicherheit von ~7% mit 10^5 Primärteilchen bis hin zu ~2% mit 10^6 Primärteilchen festgestellt. Ähnliche, aber leicht erhöhte Unsicherheiten, wurden für die 0.01 mm step size Simulationen gemessen. Verglichen mit niedrigeren Primärteilchen Anzahlen als 10^8, ergab sich wie bereits vermutet, die geringste Fluktuation für Positron-Emitter. Daraus konnte man schließen, dass die statistische Unsicherheit unter Anwendung von 10^8 Primärteilchen, weniger als 2% beträgt. Aufgrund der längeren Simulationszeit und der höheren statistischen Unsicherheit der 0.01 mm step size, fiel die Entscheidung auf die 0.1 mm step size Reichweite in die weitere Anwendung. Die maximale Anzahl an Primärteilchen, nämlich 10^8, wurden für die komplexen Bestrahlungspläne verwendet.

Homogene Phantome (90 × 90 × 300 mm³) wurden mit 10^7 Primärteilchen und einer Energie von 140 MeV bestrahlt. Um dabei festzustellen, welcher actor die passenderen Ergebnisse, im Zusammenhang mit der Reichweitenunsicherheit liefert, wurden verschiedene Phantome und zwei unterschiedliche actors angewendet. Die dabei verwendeten actors waren die *ProductionAndStopping* und *CrossSectionProduction* actors. Um das Verhalten der actors zu messen beinhalteten die Phantome verschieden dicke Schichten aus diversen Materialien. Die ^{10}C Positron-Emitter konnten aufgrund der geringen Anzahl nicht ausgewertet werden.
Beim Vergleich der Verteilungen der beiden actor, fiel die Entscheidung auf den *CrossSectionProduction* actor. Reichweitenunsicherheiten konnten sichtbar mit dem *ProductionAndStopping* actor auf ungefähr 1 mm, während mit dem *CrossSectionProduction* actor alle Materialdicken unterschieden werden konnten. Außerdem wurden deutlich weniger Positron-Emitter für den *CrossSectionProduction* actor in der Zielregion festgestellt.

Der Einfluss auf die Reichweitenunsicherheit wurde durch die unterschiedlich unterteilten Hounsfield Einheiten untersucht. Dabei wurden die Reichweiten, R_{80} und R_{50} im Zusammenhang mit der Dosisverteilung in Distal- und Lateralrichtung des Protonenstrahls, berechnet. Als Referenz diente die Dosisverteilung von dem berechneten Bestrahlungsplan. Für die MC Simulationen wurde die Standard HE Unterteilung von GATE mit der vom Bestrahlungsprogramm RayStation verglichen. Publikationen ergaben einen Reichweitenunterschied von 1–3 mm [3] [4] [5] [6]. Die Resultate der MC Simulationen mit den HE von RayStation, zeigten eine geringere Abweichung als die Ergebnisse mit den GATE HE. In Distal und Lateral Richtung waren die Reichweitenunterschiede ungefähr 0.5 mm kleiner. Das bedeutet, dass Simulationen mit einer präziseren HE Unterteilung, somit auch genauere Ergebnisse erzielen kann.

Mit den endgültig gewählten Parametern, wurden die Dosis- sowie Aktivitätsverteilungssimulationen eines bestrahlten Prostata Patienten, visuell mit dem Bestrahlungsplan, als auch der Literatur verglichen. Ähnlichkeiten und Unregelmäßigkeiten wurden bei den Aktivitätsverteilungen gefunden. Die Unregelmäßigkeiten sind auf den Export der Digital Imaging and Communications in Medicine (DICOM) Daten von RayStation zu GATE zurückzuführen.

Letzten Endes haben MC Simulationen in PT mit PET Verifikation das Potenzial die Genauigkeit der Vorhersagen und Verifikationen, im Zusammenhang mit der β^+- Aktivitätsverteilung, zu verbessern. Weitere Simulationen sind notwendig, um das genauere Verhalten und die Zuverlässigkeit der verschiedenen Simulationsparameter in GATE zu untersuchen.

1   MOTIVATION AND OBJECTIVES

Particle Therapy (PT) in general is an effective method for the treatment of malignant tissue with high energetic particles like protons and carbon ions. The ability to deliver optimal doses to the target volume, while sparing the surrounding tissue, makes PT an important technique in cancer treatment. At the particle therapy center MedAustron, built in Wiener Neustadt, Austria, not only malignant cells can be treated with charged particles, but also provide research opportunities for scientists in a variety of research fields.

Measurements and experiments in PT can be expensive and time consuming, leading to the fact that simulations offer an alternative. With advancing technology and increasing computational power over the past years, simulations in radiation oncology are playing an essential role in clinical and nonclinical fields of applications nowadays. One of these simulations are Monte Carlo simulations (MCS). They are used in codes such as GEANT3 [7], GEANT4 [8], PENELOPE [9] or FLUKA [10], which are widely recognized in high energy physics and as an assisting tool in the design of medical imaging devices or improvement of different elements in a therapy beam line. Other implementations are dose calculations or treatment planning simulations during PT [11]. With GATE (Geant4 Application for Tomographic Emission) an open-source simulation platform, which encloses the GEANT4 library, has been developed specifically for nuclear medicine and offers well described interactions of particles while passing through matter with validated physics models, 3D visualization and sophisticated geometry description [12].

The aim of this work is to create a 3D map of the β^+-activity distribution during particle therapy with protons by using Monte Carlo simulations in GATE, based on treatment plans from the treatment planning system RayStation v4.99.1 by RaySearch Laboratories from Stockholm, Sweden. Another objective is to find a correlation between activity and dose distribution during treatment planning simulation. The results should be used to improve simulations in the field of particle therapy.

2   INTRODUCTION

2.1   HISTORICAL BACKGROUND

There are different approaches to cure patients from invasive cancer cells. The three main types of cancer treatment are surgical therapy, chemotherapy and radiation therapy. The oldest and first treatment is the surgical procedure, where the goal is the removal or palliation of cancerous cells. Until the mid of the 20th century, it was the only treatment procedure, and related to a high mortality rate. The second technique is Chemotherapy. In general, modern cancer treatment is a combination of these techniques with a focus on reducing the damage on the surrounding, healthy tissue and at the same time, increase of efficiency of the treatment [13]. In 1895, Willhelm Conrad Röntgen discovered an invisible radiation generated by gas discharging lamps, causing bariumtetracyanoplatinate screens to fluorescent. Unable to explain this phenomenon he named these rays X-rays. Exposing different materials to those rays he came to the conclusion that the penetration ability strongly depends on the density and the thickness of the material [14]. The first medical treatments with X-rays were carried out from the Austrian physicist Leopold Freund. He laid the foundation for the radiation therapy in 1896 with the treatment of a girl suffering from giant hairy nevus on the back. Managing to cure the girl from her disease, the scientists observed ulcers in the inguinal area caused by the biological side effects of the radiation treatment [15].

After a few decades and with the invention of the first linear accelerators and cyclotrons, scientists were able to accelerate charged particles close to the speed of light. Thus ions came into consideration for medical and research applications. In 1946, Robert Rathbun Wilson used the Cyclotron in Berkeley, USA to measure the depth dose profiles of protons and carbon ions resulting in an increased dose at the end of the particle range. He was the first one who suggested using charged particles for clinical applications [16]. First patients were treated in 1954 with protons and a few years later with helium and neon ions [17]. Modern particle therapy centres mainly uses protons or carbon ions for oncological treatment [18].

2.2 PHYSICAL BACKGROUND

The following sections are based on the literature *Grundlagen der Strahlenphysik und des Strahlenschutze*s by Hanno Krieger [19].

2.2.1 RADIOACTIVE DECAY

Radioactivity is the emission of energy, particles or both by an instable nuclide and can occur naturally or artificial depending on whether the nuclide decayed spontaneously or was influenced by external sources. The radioactive decay is the transition of the initial mother nuclide to the resulting daughter nuclide under emission of radiation. The released energy during this process is the difference of the binding energy per nucleon from the mother nuclide and the daughter nuclide and is called mass defect.

The most common way to visualize the variety of nuclides is the Karlsruhe nuclide chart and can be seen in Figure 1. The squares represent the nuclides with the highest binding energy which are positioned along the so called stability line. N stands for the number of neutrons and Z represents the atomic number. Smaller, stable nuclides have nearly the same amount of protons and neutrons, whereas heavier stable nuclides show a higher amount of neutrons than protons. This is due to the electrical repulsion of the protons and explains the slightly downward curve orientation of the stable nuclides in the diagram (see Figure 1). In Figure 1, in the purple N-Z diagram, arrows show the different types of decay which can occur depending on the neutron-proton ratio. Only in the α – decay, the number of nucleons are changed because of the emitting helium-4-atom and is shown as the parallel arrow pointing downward the stability line, whereas at the β^{+} - decay and β^{-} - decay, a conversion of a proton or a neutron occurs which means that the number of nucleons stays the same, shown as the arrows orthogonal to the stability line (see Figure 1, purple square). Beside these types of decay there are other forms of decay: spontaneous fission, γ – decay and the inner conversion. A more detailed description of these decays is mentioned below.
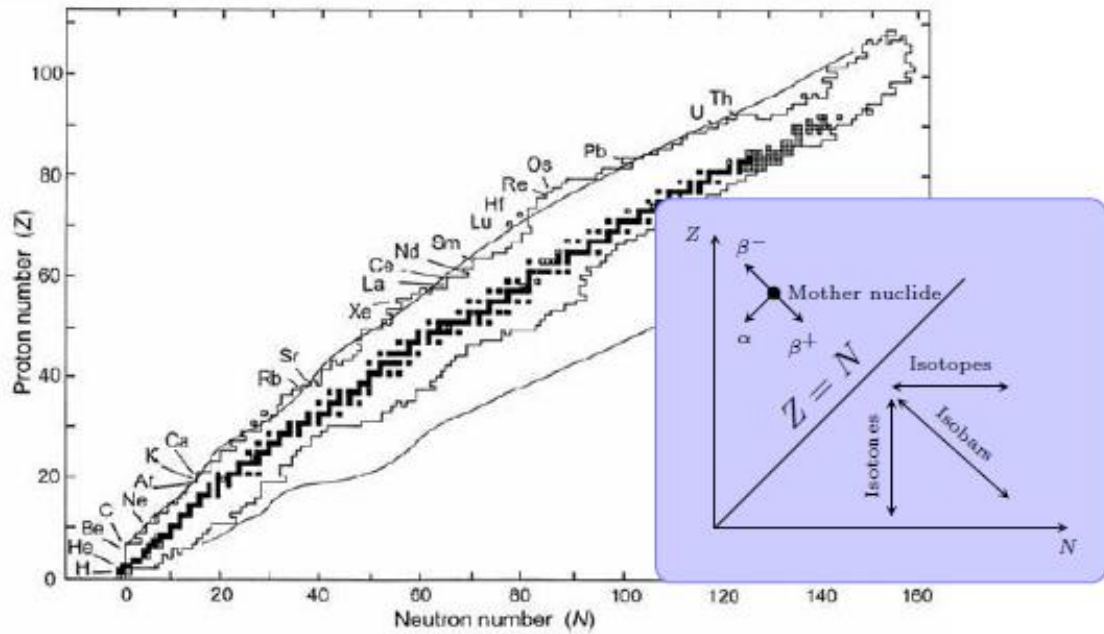
Figure 1: The squares represent stable nuclides and the right diagram shows the different types of decay depending on the N-Z ratio [Figure: Courtesy of A. Hirtl].

2.2.1.1 α Decay

Alpha decay is a process where the initial nucleus emits an alpha particle and its atomic mass and neutron number is reduced by 2. The resulting alpha particle is a double-ionized ^{4}Helium-atom. The alpha decay can be described with the following equation.

$$\ _{Z}^{A}X_{N}^{*} \Rightarrow \ _{Z-2}^{A-4}Y_{N-2}^{*} + \alpha + \text{Energy}$$

(1)

A stands for the atomic mass, X^{*} is the excited mother nuclide and Y^{*} represents the resulting daughter nucleus which can occur as well in an excited state. The energy from that event is used by the alpha particle to leave the nucleus in a quantum mechanic way with the tunnelling effect.

2.2.1.2 β Decay

The β decay is a conversion of neutrons to protons, or vice versa, under emission of charged particles and energy. In both processes the atomic number Z changes, while the mass number A stays the same. The following equations describe the involved particles:

4

$$\beta^--\text{decay:} \qquad n \Rightarrow p + e^- + \bar{v} + \text{Energy} \qquad (2)$$

$$\beta^+-\text{decay:} \qquad p \Rightarrow n + e^+ + v + \text{Energy} \qquad (3)$$

Where *n* is the neutron, *p* the proton, v and $\bar{v}$ stands for the neutrino and anti-neutrino, e^- and e^+ represent the electron and the positron. The electron and positron are also called β particles.

2.2.1.3 ANNIHILATION PROCESS

The interaction between a positron and an electron resulting in two photons is called *electron-positron annihilation.* The kinetic energy and the angle of the emitted photons, depends on the amount of energy the electron-positron pair has before the interaction. If the electron-positron pair only contains the rest energy before the annihilation, then photons at 180° to each other are emitted with 511 keV each, corresponding to the mass equivalent of an electron (see Figure 2 left). Figure 2 on the right side shows how the interaction could result if the electron-positron pair had energies unequal to the rest energy. The importance of this process for PET will be explained in chapter 2.5.
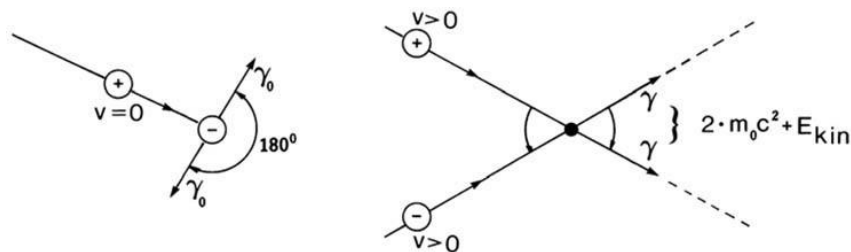
Figure 2: Left: Schematic interaction of a positron and an electron while at rest. Right: Positron and electron contain a certain kinetic energy before the annihilation process results in changing angles to each other and changed kinetic energy of the photons [19].

2.2.1.4 γ DECAY

If a nuclide is in a high energy state, it can release energy to change to a stable and lower energy state. By doing so, electromagnetic radiation or photon radiation is emitted. During the process the mass number does not change.

2.2.2 INTERACTION OF PHOTONS WITH MATTER

Interaction of photons with matter can occur in many ways. The three most important processes are *photoelectric effect, Compton effect* and *pair production.*

The *photoelectric effect* occurs if a photon interacts with an electron from the atomic shell. Figure 3 shows schematically the interaction and resulting process of the photo effect. If the energy from the absorbed photon is high enough, the electron will be able to leave the atomic shell leaving a hole behind (see Figure 3 left). This hole is filled with an electron from the outer shell under emission of a characteristic photon (see Figure 3 right). The kinetic energy E_{kin} of the emitted electron results from the difference of the incident photon energy E_γ and the electron binding energy E_b:

$$E_{kin} = E_\gamma - E_b$$

(4)
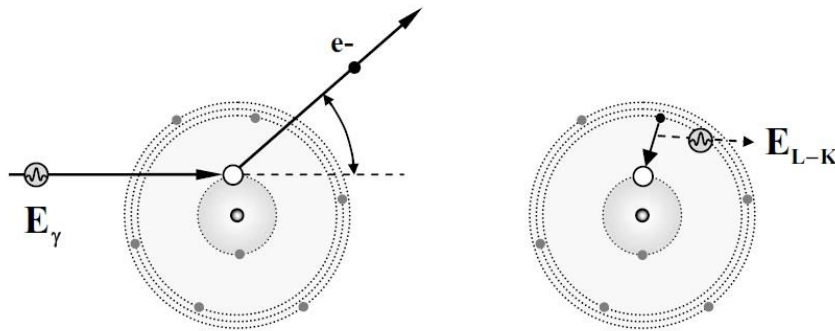
Figure 3 Illustration of the photoelectric effect: An electron which absorbs the energy of an incident photon leaves the atom and a hole behind. Right: Outer electron filling the hole created by the photon-absorption under emission of a photon *[19]*.

The *Compton effect* describes the interaction of a photon with a weak bounded electron. Unlike the photoelectric effect, the energy of the photon is not fully absorbed. This means that some of the photon's energy and momentum remains while the rest of it is transferred to the electron. In Figure 4 the interaction and scattering angle of the photon φ and electron ϑ are illustrated.

If photons interact with the strong Coulomb field of a nucleus, they can spontaneously create a positron-electron pair. This effect is called *pair production* and can be seen on the left side of Figure 5. Only if the energy of the photon is above 1022 keV, which is twice the energy of the rest mass of an electron, the process can occur. The resulting kinetic energy after the process is

$$E_{kin} = E_\gamma - 2m_0c^2 = E_\gamma - 1022 \ keV$$

(5)

whereas m_0 stands for the rest mass of an electron and positron.
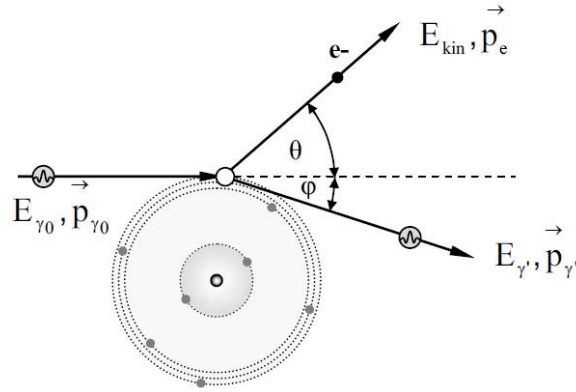
Figure 4: Schematic illustration of the Compton effect with the resulting energy and angle separation of the emitted electron and photon *[19]*.
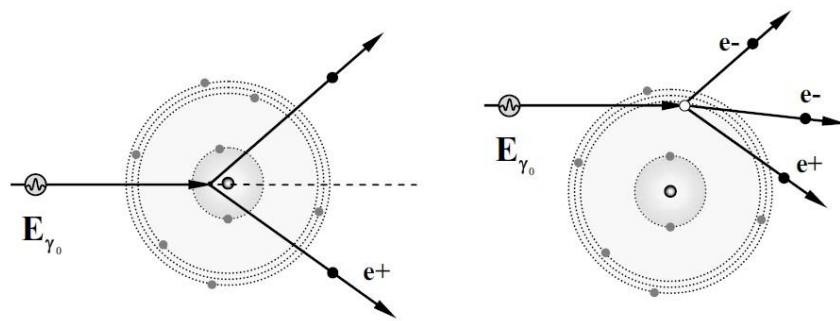
Figure 5: Left: Pair-production effect occurring by interaction with the Coulomb field. Right: Interaction of a photon with the Coulomb field of an electron resulting in a triplet production *[19]*.

In some cases *pair production* can occur in the Coulomb field of the outer shell electrons (see Figure 5 right). The small mass of the electron causes a triplet production whereas the electron itself participates in this reaction. Unlike the Pair Production, the triplet

production needs at least 4 times the rest energy of an electron. The inverse process to the pair production is the annihilation process of an electron-positron pair.

2.2.3 INTERACTION OF IONS WITH MATTER

Using particles like protons or carbon ions for cancer treatment reveals many advantages over conventional photon therapy. Photons deposit nearly their whole energy shortly after interaction with matter and then decrease in an exponential course. In contrast, protons and heavier particles have the characteristic to travel deeper and deposit most of their energy at the end of their range (see Figure 6), in the so called Bragg-peak. The energy loss per unit path length, while traveling through matter is called stopping power and can be described by the Bethe-Bloch formular. The formula in relativistic form by is shown below:

$$-\frac{dE}{dx} = 2\pi N_A r_e^2 m_e c^2 \rho \frac{Z_T}{A_T} \frac{Z_P^2}{\beta^2} \left[\ln \left(\frac{2m_e \gamma^2 c^2 \beta^2 W_{max}}{I^2} \right) - 2\beta^2 - \delta - 2\frac{C}{Z_T} \right] \qquad (6)$$

with

N_A=Avogadro constant
r_e=electron radius
m_e=electron mass
c=speed of light
ρ=density of the absorber
Z_T, A_T =atomic number and atomic mass of the absorber
Z_P=atomic number of projectile
β =velocity of particle in units of the speed of light
γ=Lorentz factor
W_{max}=maximum energy transfer
I=mean excitation potential
δ=Density correction
C=shell correction
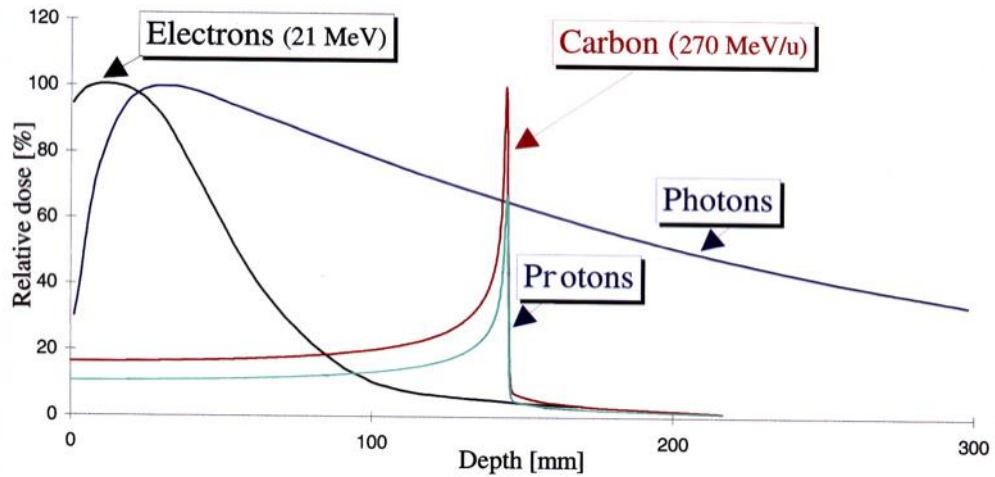
Figure 6: Bragg-peak plots of different particles. Similarities between carbon ions and protons such as electrons and photons. Fragmentation tail of carbon ion beams around 150 – 200 mm after the Bragg-Peak [20].

Besides the interaction of ions with electrons of the target material, interactions with the target nuclei can occur as well. This leads to nuclear fragmentation and the thus results in fragments which are partially β⁺-emitters. Depending on the origin of the fragmentation process, it can be separated into target fragmentation and projectile fragmentation. Heavier ions than protons, produce due to projectile fragmentation, lighter ions which have a high penetration ability and approximately the same velocity as the incident ions. The range of the fragmentation particles scales with A/Z^2 leading to higher ranges for particles with lower Z and is known as the fragmentation tail after the Bragg-peak (see Figure 6). For ions A ≤ 6, like protons, only target fragmentation is possible leading to absence of a fragmentation tail. The probability of an ion to undergo a nuclear fragmentation process is described by the isotope production cross section and particle fluence. Figure 7 shows schematically a fragmentation process and Table 1 the most appearing β⁺-emitters.
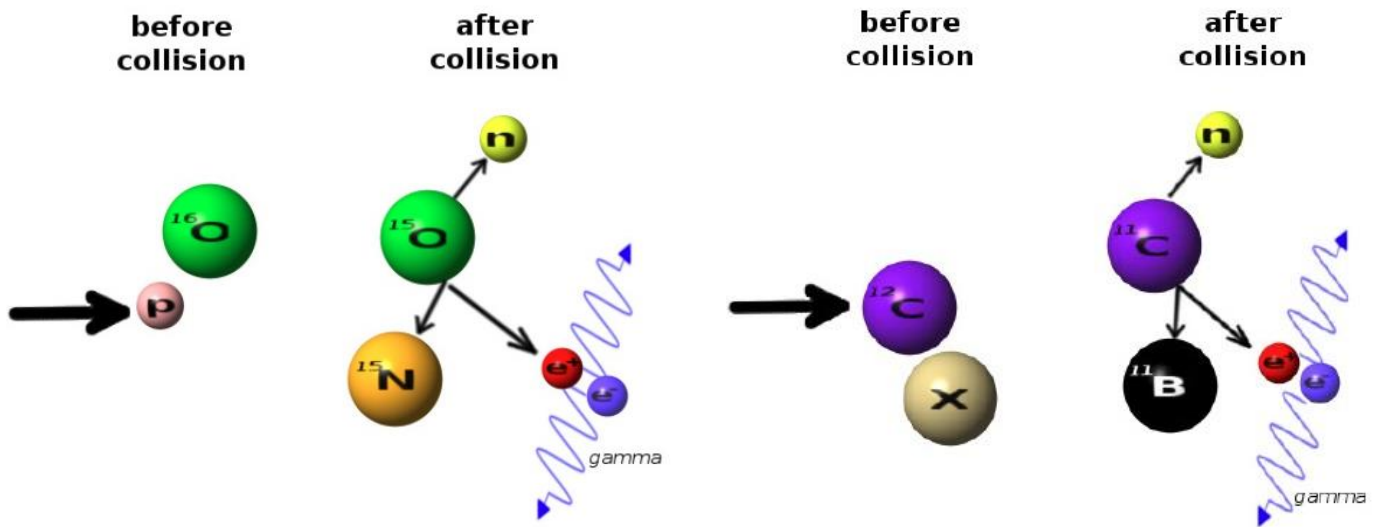
Figure 7: Left: Illustration of target fragmentation of a proton colliding with a ^{16}O. The result is a neutron and a ^{15}O fragment which emits a positron by undergoing β^+-decay to form ^{15}N. Right: ^{12}C colliding with a target particle creating a ^{11}C fragment and a neutron. The ^{11}C, β^+-decays to ^{11}B and emits a positron. In both processes the positron annihilates with an electron and forms two gamma photons [21].

β^+-emitter	$T_{1/2}$
^{11}C	20.28 min
^{15}O	2.03 min
^{13}N	9.96 min
^{10}C	19.3 s
^{8}B	770 ms
^{9}C	126.5 ms
^{14}O	70.59 ms
^{12}N	11.0 ms
^{13}O	8.58 ms

Table 1: Half-lives of the most common β+-emitters in particle therapy.

2.3 RADIOTHERAPY

Radiotherapy can be separated into two modalities: external beam therapy and brachytherapy [22]. In brachytherapy radioactive sources are placed within or in close proximity to the tumor, to produce desired dose distributions. Whereas in external beam therapy the tumor is irradiated by an external beam, e.g. with a source, spatially separated from the patient.

2.3.1 CONVENTIONAL PHOTON THERAPY

Conventional photon therapy uses high energetic photons or electrons for treatment of malignant cells or sometimes for benign lesions. The production of therapeutic X-rays is done by accelerating electrons up to MeV range with a linear accelerator aiming at a metal plate, creating via Bremsstrahlung a specific spectrum. Afterwards, the X-ray beam is flattened and narrowed down, in respect to the energy spectrum and beam shape, with collimators and filters to achieve a more precise and equally energetic beam (see Figure 8). The absorption curve of photon beams (see Figure 6) show a steep increment behind the surface and reaches shortly after, the maximum in dose deposition. This is the so called build-up region, which ends afterwards as an exponential decrease. Target volumes are irradiated from multiple directions due to the fact that photon beams have unequal ranges, caused by photon-matter interaction processes like photo effect, Compton scattering or pair production.

In RT it is important to distinguish between the desired target volume and organs at risk (OAR) which are sensitive to radiation. The aim is to minimize all unnecessary irradiations for the OAR while at the same time maximize the energy deposition in the target volume. The nomenclature and methodology of target volume specifications is defined in the International Commission on Radiation Units and Measurements (ICRU) reports 50/62 and can be divided into three volumes [23] [24]. The smallest volume is the Gross Tumor Volume(GTV). The GTV is the known tumor volume that is palpable or visible. With the GTV and/or additional subclinical microscopic malignant tissue the Clinical Target Volume (CTV) is formed. The last target volume is the Planning Target Volume (PTV). It contains the GTV and CTV, and is used as a geometrical concept for the

treatment planning and evaluation purpose. It contains an additional margin around the CTV, to ensure that the prescribed dose will actually be absorbed by the whole CTV. For the verification of the location of the target volume and OAR, an imaging technique has to be applied. This can be done by computer tomography (CT), magnetic resonance imaging (MRI) and positron emission tomography (PET). Furthermore, treatment planning can be applied on the data.

The Hounsfield unit (HU) is a grey-scale, which expresses CT numbers in a standardised and convenient form, and is related to the density of the material. It is obtained from the measured attenuation coefficients of a certain tissue and water. The scale is typically in the range of -1000 to 3000, where air has the value of -1000, water 0 and bone 300 to 3000. A greater subdivision of the scale allows it to display between different less dense objects on the computer screen.

Nowadays therapies are carried out by conformal radiotherapy, intensity modulated radiotherapy (IMRT) or image guided radiotherapy (IGRT). Simple shaped tumors can be treated with conformal RT, which consist of different shaped beams originating from several directions. The beams are shaped by a multi leaf collimator to create a contour of the PTV for each direction. Overlapping of the different beams leads to the desired dose distribution in the PTV. For more complex shaped volumes, an IMRT and IGRT can be utilized. Like the conformal RT, they use a multi leaf collimator for the contour of the target volume. Additionally, changes in intensity of the radiation are applied. With IMRT and IGRT the undesired dose for the surrounding healthy tissue can be limited. The difference between those two techniques is that, in IGRT additional CTs are performed before or during the treatment. Superimposition of the CTs lead to information about movements of the tumor and therefore increment in accuracy, regarding the radiation. The downsides are longer treatment time, higher exposure to radiation and cost.
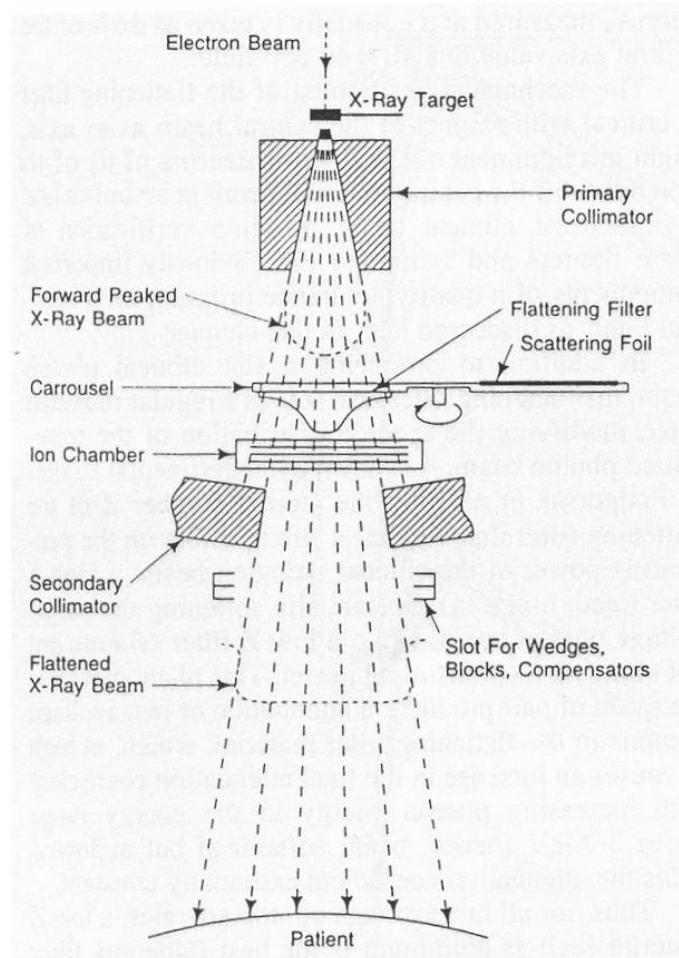
Figure 8: General setup of a treatment head from a linear accelerator for RT [25].

2.3.2 PARTICLE THERAPY (PT)

Particle therapy in general is the application of particles heavier than electrons for the treatment of malignant tissue located in the patient's body. Compared to conventional external RT, ions deposit the energy at a finite range, while delivering a minimum dose to the surrounding healthy tissue and OAR outside the PTV (see Figure 6). Most commonly used particles are protons and carbon ions, which share a superior depth dose distribution compared to photons. Nevertheless, different ions species with different masses reveal different physical characteristics such as, beam broadening, relative biological effectiveness, linear energy transfer etc.

The following chapter gives a brief introduction to the biophysical properties in PT, comparison between the main particles used for treatments and a short introduction to beam delivering techniques.

2.3.2.1 BIOPHYSICAL PROPERTIES IN PARTICLE THERAPY

Energy deposited by a particle traveling through matter can be measured by the linear energy transfer (LET), generally in units of keV/µm, and is closely related to the stopping power. The stopping power can be seen as a material property, whereas the LET as loss of energy of the particle. LET is not a constant parameter, because the charge and energy of a particle change while traveling through matter. However, it's a widely used quantity for the classification of induced damage by ions.

The oxygen enhancement ratio (OER) indicates the influence of ionizing radiation on tissue depending on its oxygen fraction. It is the ratio of the dose needed in oxygenated and low oxygenated tissue to achieve the same biological effects. With increasing LET the OER decreases, leading to an advantage for ions with a high LET in PT [26].

$$ OER = \frac{D_{hypoxia}}{D_{air}} \tag{7} $$

Different particles with the same dose deposited, lead to different biological effects. With the relative biological effectiveness (RBE), the particles can be categorized relatively to a reference radiation, resulting with the same biological effect.

$$ RBE = \frac{D_{ref}}{D_{ion}} \Big|_{\text{same biol. effect}} \tag{8} $$

The RBE rises with increasing LET and reaches its maximum at approximately 100-200 keV/µm. Above dese energies, the RBE decreases. This is known as *overkill effect,* because more dose is deposited than needed.

14

2.3.2.2 PROTONS AND CARBON IONS

Current particles in clinical use are protons (^{1}H) and carbon ions (^{12}C). There are a few notable physical and biophysical differences between carbon ions and protons. The RBE value for protons is close to photons, whereas for ions heavier than helium an increment can be observed [27] [28]. The RBE for carbon ions varies between 1 and 3. Another difference is the 1%-15% smaller OER for carbon ions [26] over protons in hypoxic regions.

Comparing the beam dose profiles in lateral and longitudinal direction more variance can be seen (see Figure 9). Important observations are decreasing Bragg-peak height with increasing beam energy, or peak to plateau ratio, and broadening of the Bragg-peak. This phenomenon is called range straggling and effects protons more than carbon ions. It is caused by unequal number of collisions of particles in a monoenergetic beam resulting in deflections of the particles. Although a proton is barely deflected by an electron while passing through matter, multiple deflections can still cause a deviation. The spreading in lateral direction can be observed with increasing beam energies. Obviously carbon particles are not as much affected by this phenomenon like protons.

Another noticeable difference in dose distributions results from the fragmentation tail (see Figure 10), located after the Bragg-peak. As already described in chapter *2.2.3*, for ions with A ≤ 6 no fragmentation tail can be observed, whereas for heavier particles additionally projectile fragmentation takes place. Nevertheless, the range of the fragmentation tail increases with increasing beam energy and has to be considered during PT.

The benefits of carbon ions over protons are sharper lateral and longitudinal edges as well as a higher LET/RBE value. On the other hand, the higher and varying LET/RBE value, makes planning of physical dose distributions significantly more complex than for protons. Another important aspect is the fragmentation tail, which has to be included in the treatment plan to avoid undesired dose depositions in healthy tissue. Significantly more patients are treated with protons than carbon ions, which results from higher

costs, higher uncertainty in terms of RBE and higher risk of late normal tissue damage due to higher RBE, for carbon ions over protons in particle therapy [29].
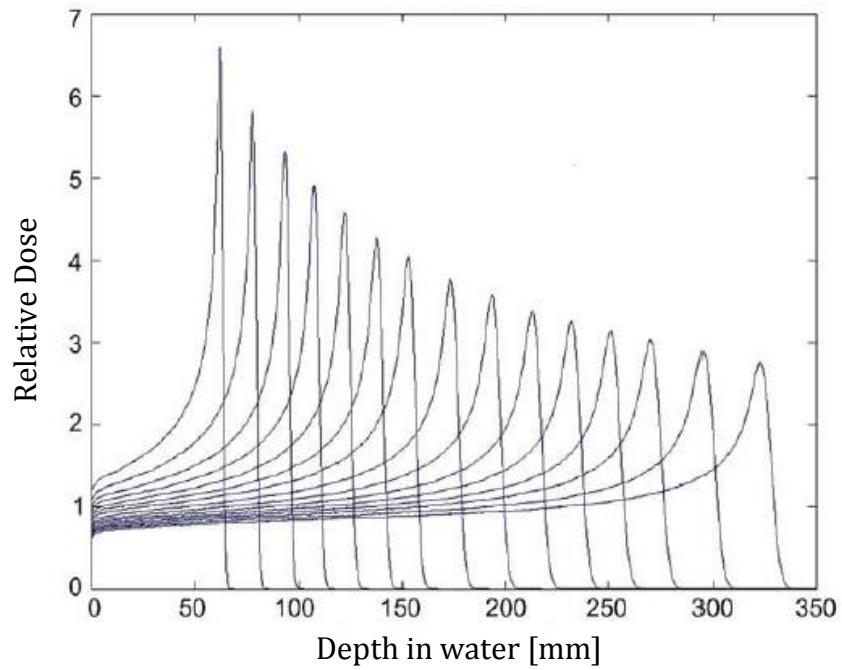
Figure 9: Decreasing Bragg-peak height with increasing energy of the particle beam *[30]*.
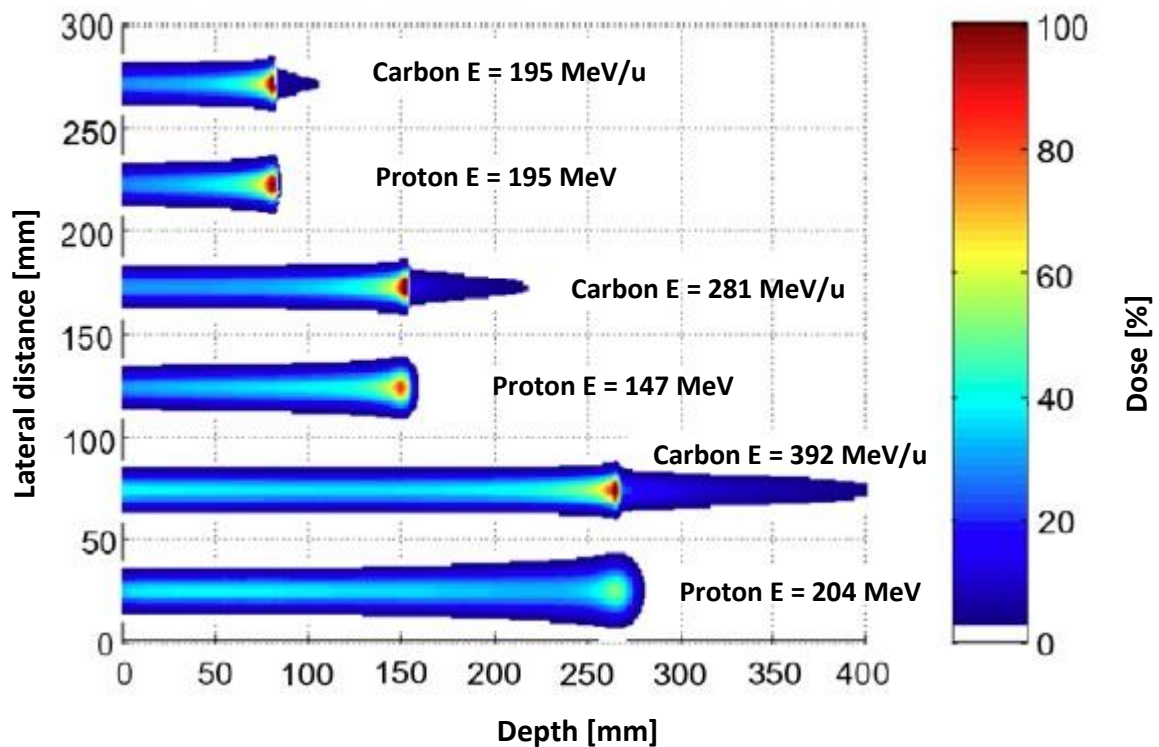
Figure 10: Measurements with proton and carbon ion beams showing different dose distributions at different energies. Increasing fragmentation tails for carbon ion beams and increasing spread out for proton beams at higher energies can be observed *[30]*.

2.3.2.3 PARTICLE THERAPY WORKFLOW

The general workflow for PT can be described in 5 steps; immobilization, data acquisition, treatment planning, simulation and irradiation. The workflow is the same for radiotherapy and photontherapy.

Reducing the motion of the patient through immobilization, the efficiency and occupation time of the treatment room can be improved. This can be done by fixing the patient with a thermoplastic mask or with vacuum bags e.g. for pelvic tumors. Additionally, available robotic positioning systems help to increase the accuracy. After the fixation of the patient, CT, MRI or PET scans are acquired. Thus, data for the determination of the target volume and sensitive organs are collected, which is essential for the planning phase. The radiation oncologist uses the data to place contours of the

target volume and different organs in the treatment planning system. The required dose and irradiation fields can be then simulated based on the contours, taking into account the irradiation timing. For the treatment, the patient has to be moved to the treatment room. Normally, the patients walk to the room by themselves, where another positioning verification has to be done. The treatment can be carried with different modalities depending on the complexity of the treatment plan, more specifically the shape of the target volume.

2.3.2.4 BEAM DELIVERY TECHNIQUES IN PARTICLE THERAPY

A single monoenergetic particle beam is not able to cover the required treatment volume, therefore a batch of multiple Bragg-peaks at different energies is used. This is the so called, spread-out Bragg-peak (SOBP) which can be used in treatments (see Figure 11). The main techniques for particle delivery are passive scattering technique and scanning beam technique.
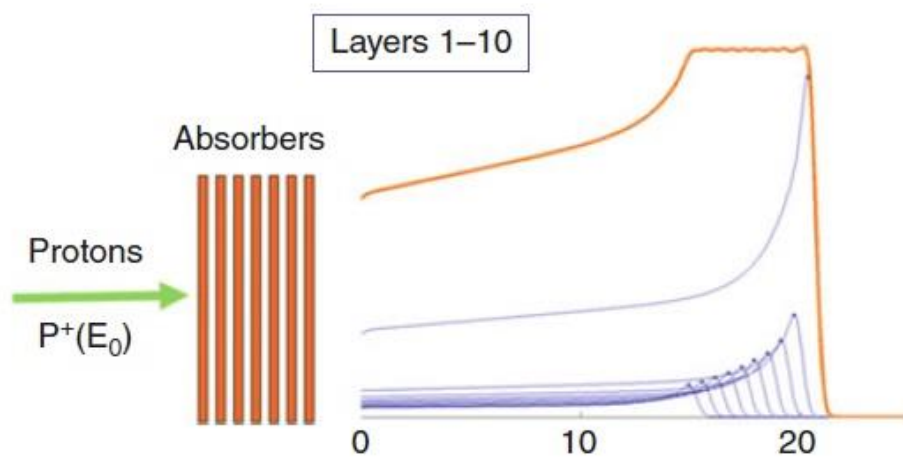
Figure 11: Adding up particle beams at different energies (blue line) to cover the treatment volume with the SOBP (orange line) *[31]*.

The passive scattering technique uses collimators and scattering material to shape the beam into the contours of the target volume. With different range modulators a Gaussian-shaped beam profile and the required longitudinal spread or SOBP-shape is formed (see Figure 12). The advantages of the passive scattering technique over the scanning beam technique are for example lower costs, more reliability, dosimetry less

18

difficult and organ motion consideration is less critical. Furthermore, for each patient a special formed scattering block has to be designed to achieve the desired dose distribution.
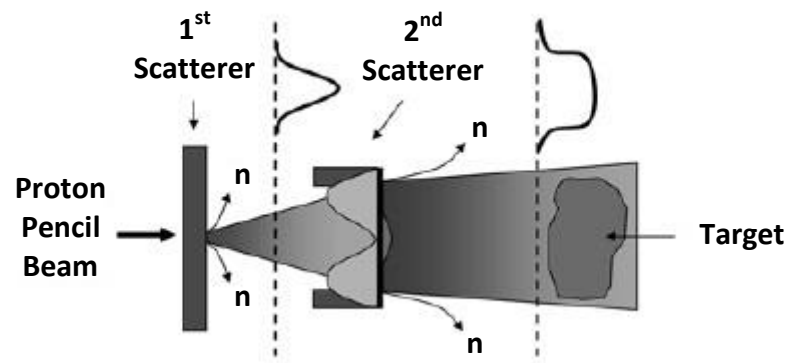
Figure 12: Passive scattering technique use collimators and range shifters to create the desired target volume *[32]*.

Active scanning uses magnets to deflect the beam in lateral direction on specific voxels in the target volume. The voxels are irradiated at different energies to achieve the desired shape of the SOBP in longitudinal direction (see Figure 13). Voxels in the most distal region of the target are first irradiated, proceeding to the more proximal voxels. More and more facilities are using active scanning systems nowadays due to the fact that nearly every shape can be irradiated while minimal non-target dose is deliverd. Logistically it offers another advantage, namely that only magnets have to be adjusted instead of the scattering material or filters.
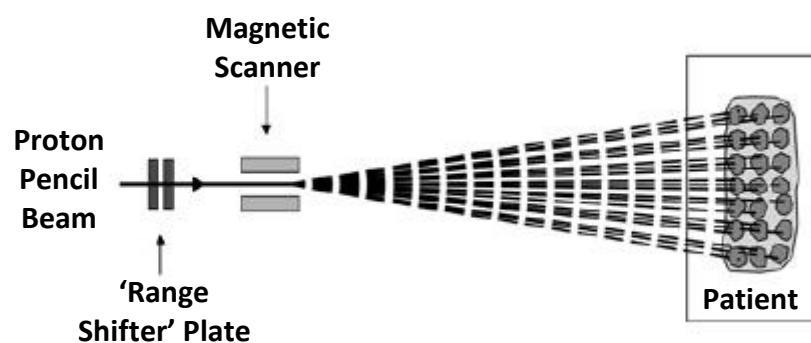
Figure 13: Active scanning uses magnets to deflect the particle beam on the different voxel spots *[32]*.

Nowadays most treatment facilities use intensity modulated radio therapy with ions as treatment modality. As already described for photons in chapter *2.3.1,* the principle is

the same for ions. Only with active scanning it is possible to use IMRT with ions in PT. The combination of active scanning and intensity modulation, voxels at specific energies can be irradiated [33]. IMRT in general describes the number and delivery of fields, which superimposed lead to an overall homogeneous dose distribution in the target volume. Whereas, doses deposited to the healthy surrounding tissue is kept at a minimum.

2.4 PET – POSITRON EMISSION TOMOGRAPHY

The basic principle of positron emission tomography in nuclear imaging is the detection of a photon-pair resulting from the annihilation of an electron-positron collision. These electron-positron pairs can be produced by injecting radiopharmaceutical substances intravenously or by irradiating the patient with ions such as protons or ^{12}C ions. With the resulting e^+ emitters, metabolic activity can be visualized. In nuclear imaging these radiopharmaceutical substances are called tracer. They can be distinguished by their half-life and participation in metabolic processes. The most common used tracer in PET is the 2-deoxy-2-[^{18}F]fluoro-D-glucose ([^{18}F]-FDG), due to his analogy to glucose and therefore elevated uptake from cancer cells [34] [35].

An important component of the PET scanner system is the scintillating material, which detects the emitted photons and converts it to photons. Important properties of scintillating materials in PET are the stopping power for 511 keV photons, scintillation decay time, light output and energy resolution [36] [37]. Nowadays most used scintillating materials are composed of Bismuth Germinate (BGO) [38], Lutetium Oxyorthosilicate (LSO) [39] or Thallium (Tl) added to Sodium Iodine (NaI) [40]. In Table *2* the major attributes of the materials is listed.

Connected to the scintillating crystal is a photo multiplier tube (PMT) which converts and amplifies the light photons to an electrical pulse. Ideally each crystal would be connected to a single PMT to achieve a high resolution but this would be impractical and expensive. A solution is to cut a single detector crystal into several smaller crystals and connect these crystals to a bundle of PMT's, which is called a detector block. Thus the

20

number of used PMT is reduced and light guides for the light photons, preventing them to overrun to neighbouring crystals, are created, keeping the resolution in a viable range (see Figure 14).
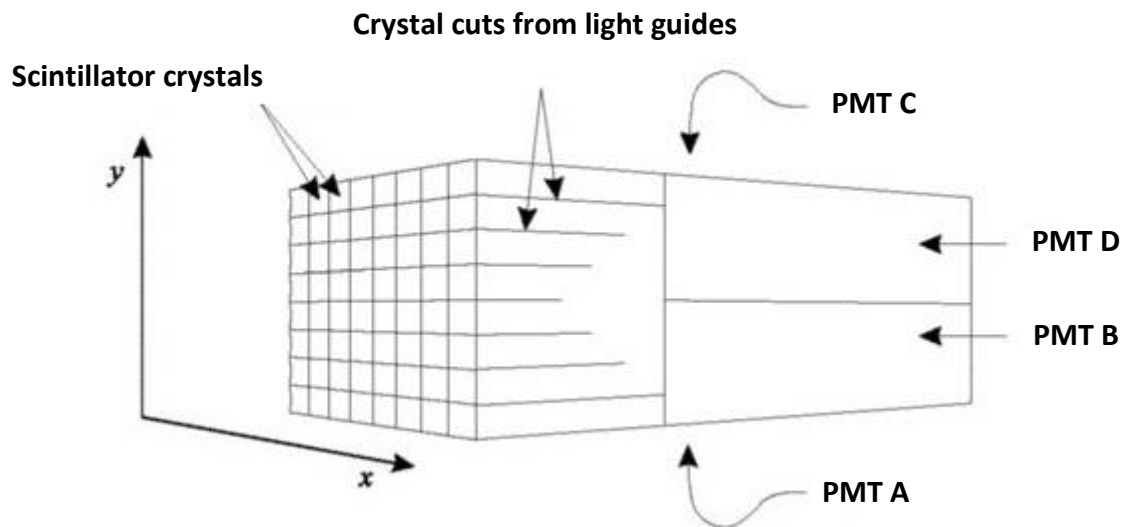
Figure 14: Block detector design of a conventional PET. Cuts in the scintillating material are used as light guides for the light photons. Scintillating crystals are attached to 4 PMT *[41]*.

Most common PET scanners are designed as full- ring systems composed of several rings, whereas each ring consists of a number of detector blocks. Another type of scanner is the partial-ring scanner system. One major difference between those scanners is that the partial-ring scanners have to rotate during a scan to achieve a full 360° measurement [42] [43].

During a scan several impulses originate from incident photons that are registered by the detectors and are combined by a coincidence circuitry to a signal. Coincidences, which are basically detected photon pairs, can be divided into: true, scattered, random and multiple coincidences, depending on the interaction with their surrounding until reaching the detector. Scattered coincidences result from deflection of photons in the patient body. Photon pairs which are falsely considered as related pair are called random coincidences and if several photons are detected at the same time, it is called multiple coincidence. Only true coincidences are considered as a valid signal and can be seen schematically in Figure 15.
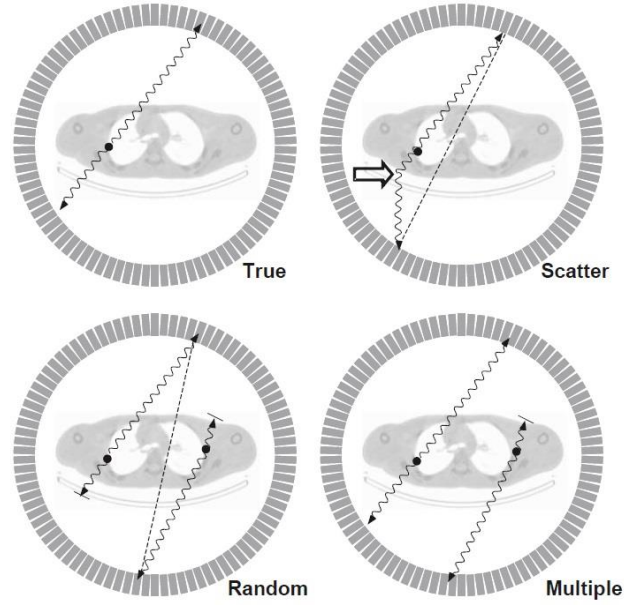
Figure 15: Interaction with matter during emission of the photons can lead to a wrong coincidence. Only true coincidences are accepted as a valid signal *[44]*.

Properties	NaI(Tl)	BGO	LSO
Atomic number	50	74	66
Density (gm/cm³)	3.7	7.1	7.4
Decay time (ns)	230	300	40
Photon yield per keV	38	6	29
Light output	100	15	75
Lin. attu. coef. (cm-1)	0.35	0.96	0.87
Energy resolution (% at 511 keV)	6.6	20	10

Table 2: Physical properties of different scintillators used for PET applications *[37]*.

To display the resulting raw data as a 2-D matrix, a sinogram can be used. A sinogram is the plot of the vector coordinates $S(s,\varphi)$ of an activity in a PET scan (seeFigure 16). The vector $S(s,\varphi)$ results from the imaginary line between the detected photon pair and is called line of response (LOR).
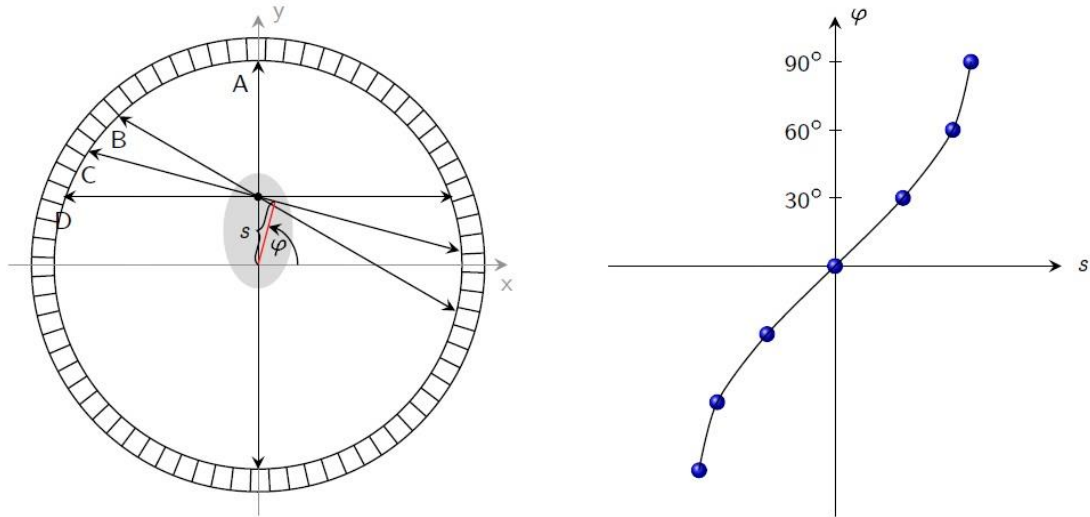
Figure 16: Left: Different LORs detected by the scanner shown as A,B,C and D arrows. Right: Connecting the different coincidence data points S(s,φ) with each other to gain a sinogram [Figure: Courtesy of A. Hirtl].

2.5 PARTICLE THERAPY WITH POSITRON EMISSION TOMOGRAPHY VERIFICATION (PT-PET)

PT with PET verification is mainly applied in clinical trials or nonclinical experiments and is a popular non-invasive monitoring application for dose delivery [3] [6][45][46][47][48] [49]. As already explained in the previous chapter, the principle is to use β^+-emitters to visualize the radiotracers produced by nuclear fragmentation by the therapeutic beam, in the human body with diagnostic PET after or during irradiation. The ion beam leaves a footprint of radiotracers in the beam path, which is imaged by the PET scanner. Another purpose of PET is the verification of particle range and field lateral position, during or after PT. The coincidences resulting from the annihilation process of an electron-positron pair can be used to monitor the activity distribution of positron emitters. Thus, the activity distribution can be seen as a conformation of interaction between treatment beam and target as well as information about the pathway of the beam. The direct evaluation of the delivered dose from the positron emitter distribution is not possible, due to the fact that both distributions result from different physical processes. The workflow is to compare the activity distribution of the PET measurements with expected distributions from, e.g. MC simulations, or reference images. The main resulting, and in

this thesis focusing, positron emitters are ^{11}C and ^{15}O [50], because of the long half life time and high production number during PT (see Table 1).

2.5.1 PT-PET Range Verification Setup

Depending on the setup of the PT-PET system, one can differentiate between in-beam PET, in-room PET and off-line PET [51] (see Figure 17). The **in-beam** PET configuration has the ability to measure positron emitters during the treatment. This means that the system is capable of measuring the positron emitters which are produced right from the start of irradiation. The drawback of the in-beam PET system is the geometrical arrangement of the double-head PET itself. This leads to a reduction of the image quality. Simultaneous irradiation and detection would probably lead to interaction between the (horizontal) beam line and the PET itself. This is why the PET has to be arranged in a limited angle geometry leading to artefacts in the images [52]. Another drawback is the high costs of such a system. Higher image quality and a more cost efficient PT-PET configuration is the **in-room** PET system. Right after irradiation the activity is measured in the same room without repositioning of the patient. This means that a conventional PET system can be used. The disadvantage of this detection system is the lack of detection of valuable positron emitters from the beginning, a slightly poorer determination of range modification based on the treatment plan and the occupation of the treatment room due to the PET measurement. The last detection arrangement is the **off-line** PET/CT. The irradiation and the measurement of the activity distribution are carried out in separate rooms, normally with a standard diagnostic PET, which leads to a longer workflow time per patient. A repositioning of the patient is normally necessary, except if a sophisticated shuttle system is installed. Another drawback is the lack of information about particle ranges of two nearly opposite irradiation fields as well as the high signal-to-noise ratio. Because of the time gap between irradiation and imaging, activities of different irradiation fields are hard to differentiate. On the other side, off-line PET/CT detection systems are cheap and have good results for single irradiation fields [51].
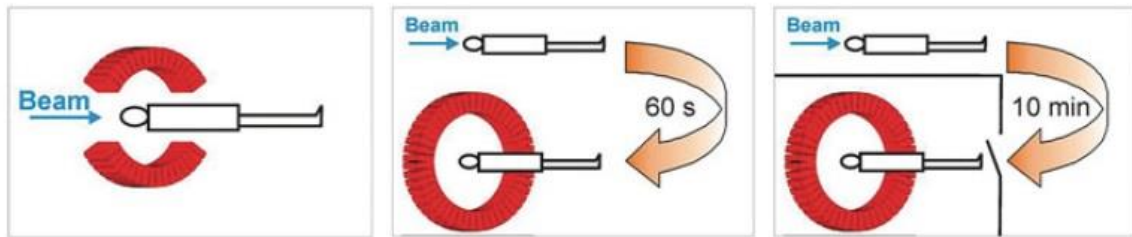
Figure 17: Three different PT-PET systems. Left: in-beam PET; simultaneous irradiation and monitoring. Middle: in-room PET; activity measurement shortly after irradiation in the same room. Right: off-line; activity measurement in a separate room after irradiation [53].

2.5.2 PT-PET WORKFLOW

The additional steps in a typically PT-PET workflow compared to the standard procedure of PT contain the simulation of the a β^+ activity distribution using MC simulations [8] [6] [54][55] [56] based on the patients' treatment plan and irradiation time structure, as well as the actual measuring of the produced activity in the patients using a dedicated PET scanner. Subsequently, the simulation, after image reconstruction, is compared with the PET measurement (see Figure 18) [57]. A dissimilarity can lead to a correction of the TP, re-positioning of the patient, or tackling other occurring problems, such as mucous-filled sinuses or intraintestinal gas pockets. Otherwise the fraction is classified as valid and further treatment fractions can be performed as planned. Figure 19 shows a simplified flowchart of PT-PET, more precisely the decision process for fraction initiation.

Another alternative PT-PET workflow is to measure the activity at each session and compare it with the activity distribution from the first measurement without using any MCS at all (see Figure 20). If a reduction or changing of the anatomical structures are observed, the treatment plan has to be recalculated before the next fraction [58]. This workflow implies a correction dose deposition in the first treatment fraction, as this acts as the benchmark for all subsequent PET measurements.

Common PT-PET treatments are carried out with multiple irradiation fields, which is why the patient or the gantry angle has to be adjusted after each field. The time consumption of the previous discussed PT-PET range verification systems can be seen in Figure 21. It is clearly visible that the In-beam PET is the fastest method, because no repositioning during one treatment session is needed. As already mentioned before, PET measurements only provide valid results during or after the irradiation of the first field, if there are two opposite fields. The most time consuming workflow is the Off-line PET system, because of the spatially divided treatment and PET scanning room. However, this does not count as irradiation time. It is additional time for the patient to be relocated out of the treatment room, into the scanning room. Also, it is the one with the least amount of effort regarding the treatment. Additionally, to the time which is

needed to transport the patient to the PET room a low dose CT has to be carried out for the positioning and attenuation correction.
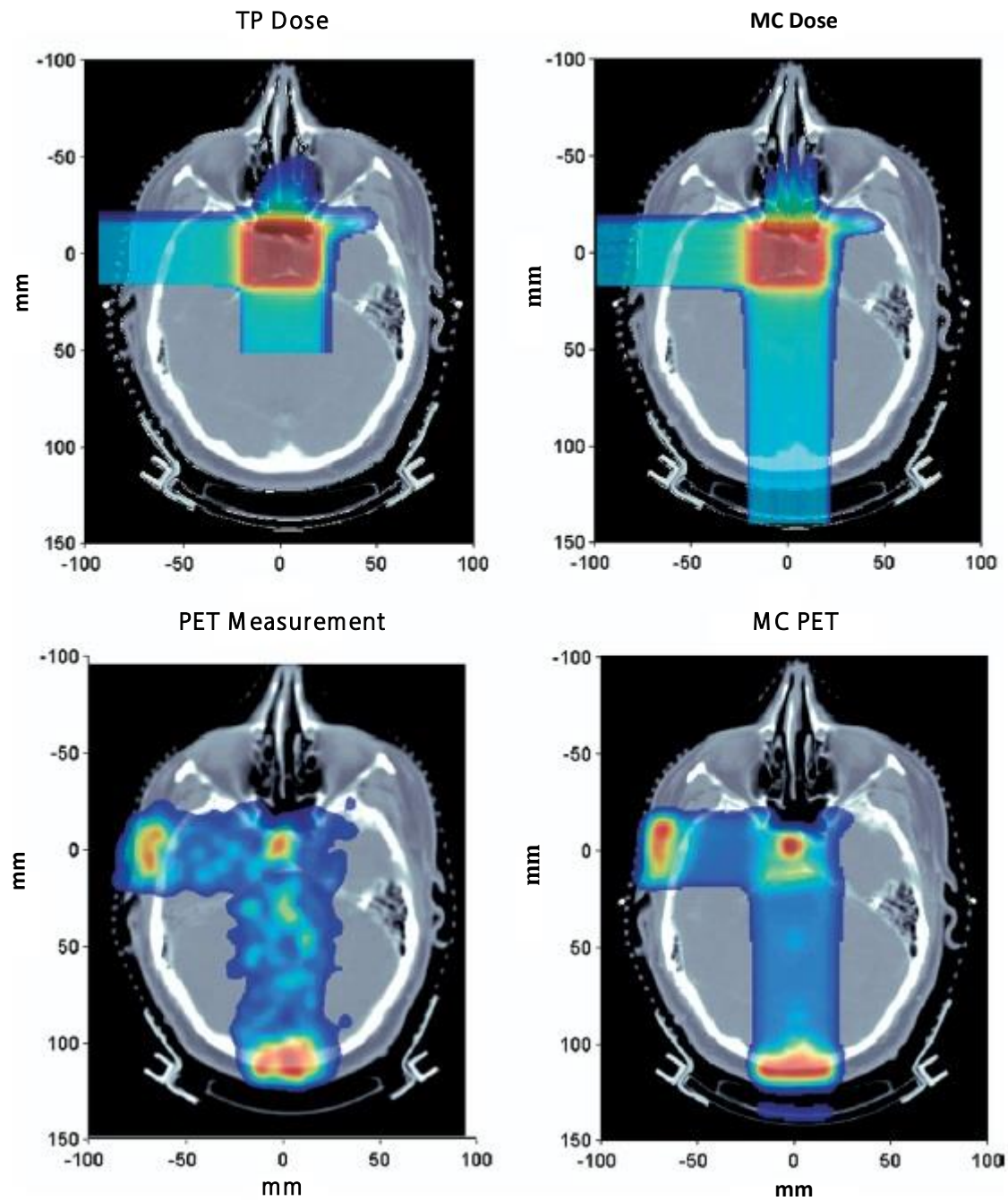
Figure 18: Comparison of a TP and MCS. Top: Dose distribution of the TP and MCS. Bottom: Activity distribution of PET measurements and MCS *[6]*.
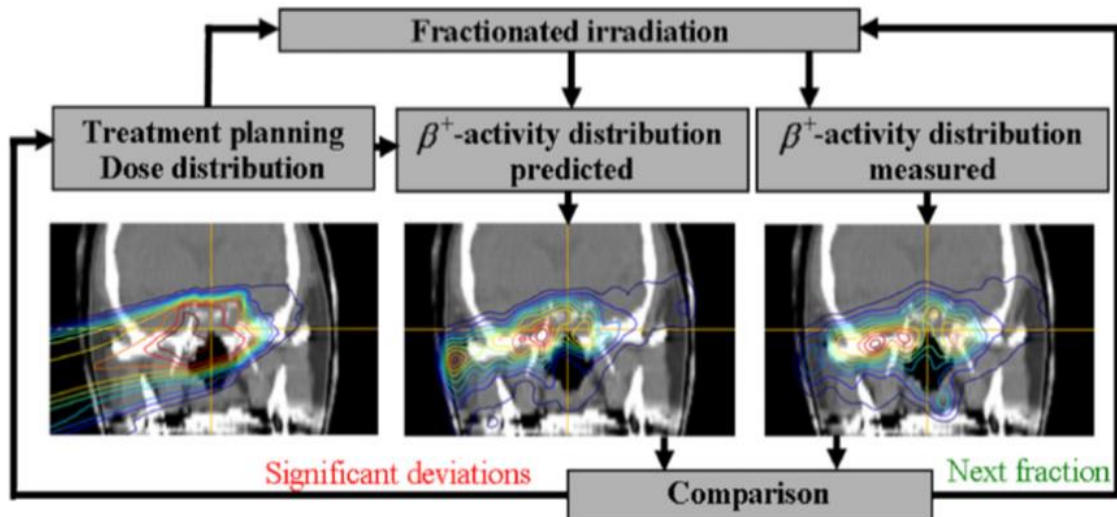
Figure 19: Workflow of a PT-PET showing superimposed dose and activity distributions onto a CT. Simulated prediction of the β⁺ activity distribution is compared with the measured distribution. Next fraction is initiated if the comparison shows no significant deviations [59].
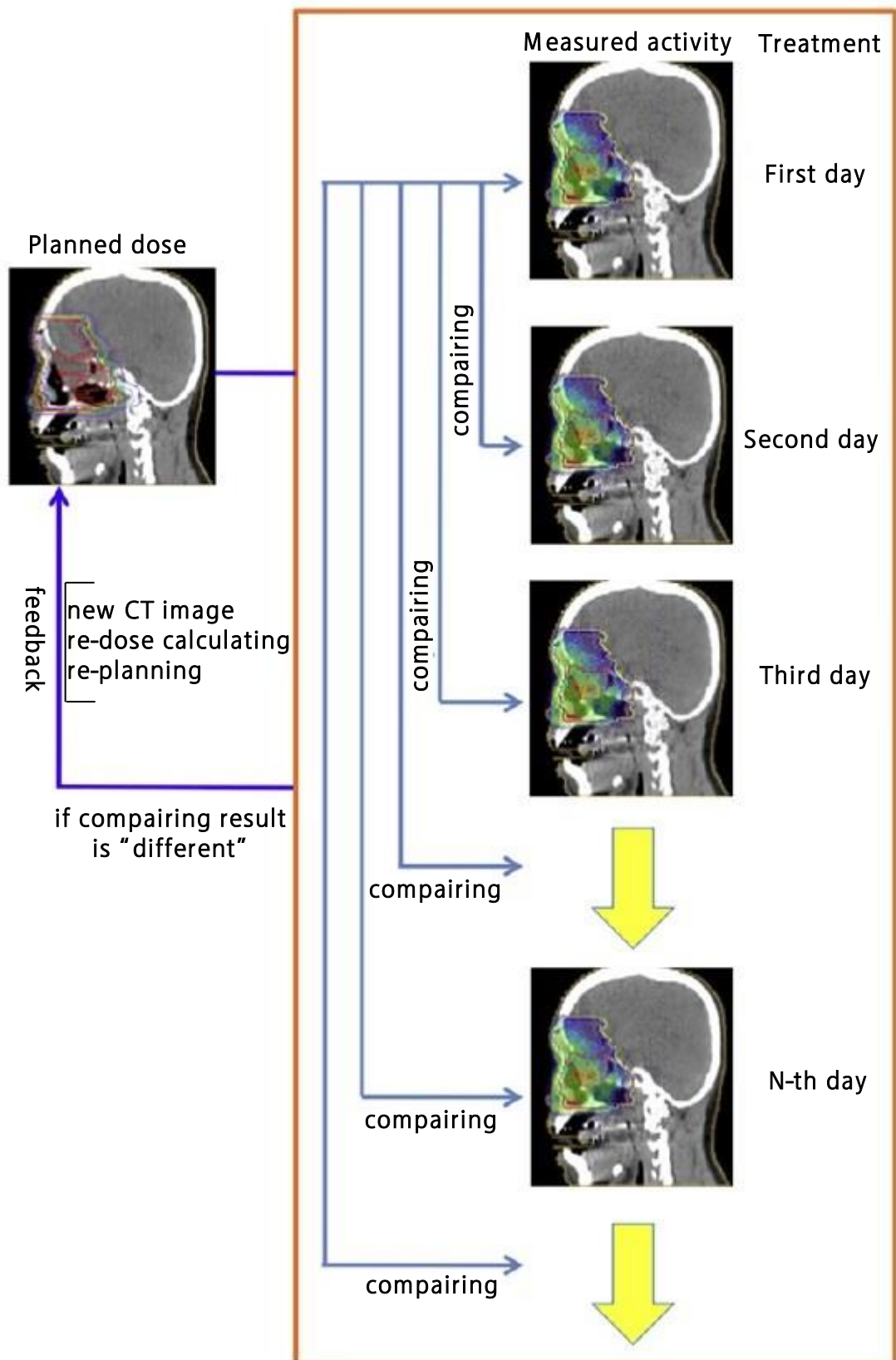
Figure 20: Flow diagram of a PT-PET workflow. Comparison of CTs after each scan in order to re-calculate the plan *[58]*.
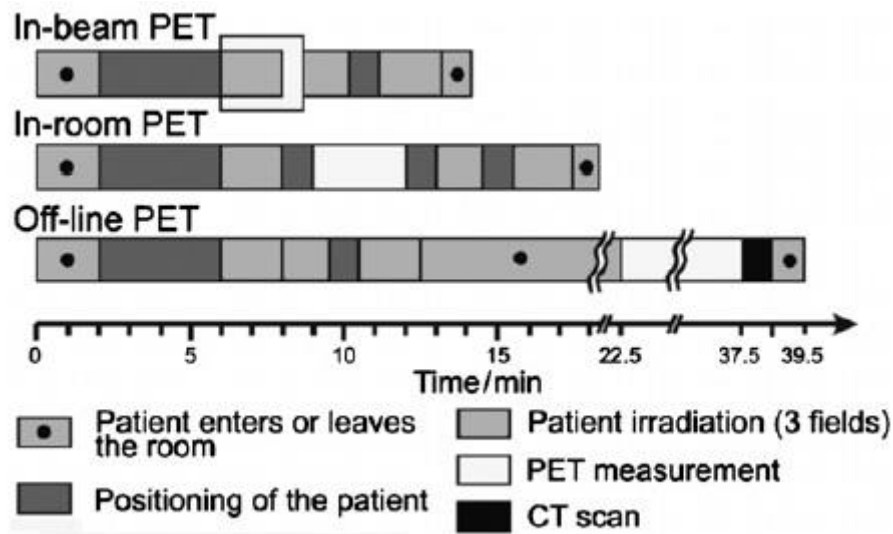
Figure 21: Schematic comparison of different workflows showing the time consumption *[59]*.

2.5.3 OVERVIEW OF INSTITUTES EXPLORING PT-PET

Heidelberg Ion-Beam Therapy Center (HIT), Heidelberg, Germany

In May 2004 the construction of the HIT started and was finished in November 2009. About 3 years later the implementation of the first 360° ^{12}C gantry was finished, thus a highly precise and efficient treatment of radioresistant tumors was possible. Since 2009, over 1000 patients have been treated. At full capacity approximately 750 patients per year can be treated, by using intensity modulated scanning technique, protons and/or carbon ions for particle treatment and robotic-table positioning. The synchrotron allows the use of carbon ions with 430 MeV/u [60][61] [62]. The HIT has a full-ring SIEMENS Biograph mCT installed in close proximity to the treatment rooms, which is used as an off-line PET/CT system [63].

Heavy Ion Medical Accelerator (HIMAC), Chiba, Japan

The construction of the HIMAC started in 1988 and was finished in 1993. First clinical studies with carbon ions started shortly afterwards and until 2011 approximately 6000 patients were treated. In the same year the new 3D scanning irradiation treatment was initiated, improving the treatment of moving targets. Till December 2015, approximately

30

10000 patients have been treated and the facility has the capacity to treat 800 patients per year by accelerating ions at 430 MeV/u in the horizontal and vertical treatment rooms and 400 MeV/u in the gantry room [64] [65]. Additionally, the center has the capability to use an in-beam PET with a partial ring detector system for research purposes, as well as an off-line PT-PET setup, using a SIEMENS ECAT HR+ PET [58] [66].

GSI Helmholtzzentrum für Schwerionenforschung, Darmstadt, Germany

The GSI was the first facility in Europe which was able to perform ion-beam therapy with carbon ions. It was also the first facility worldwide which successfully implemented intensity modulated ^{12}C ion beam therapy into the treatment site. In 1997 the first patient treatments started and till 2008 over 400 patients were treated with ^{12}C. A geometrically improved PET scanner has been developed at the GSI, making it possible to simultaneously monitor and perform treatments with carbon ions. Thus, the first experiments with an in-beam PET monitoring system were performed. This proved the capability of the new designed double head PET scanner for quality assurance during ion beam therapy. The double head detector was built from an ECAT EXACT PET scanner. The new facility used a magnetically swept, pencil like heavy ion beam of varying energies to irradiate the target volume, which was at that time an outstanding feature in PT [52] [67] [68] [69].

MedAustron, Wiener Neustadt, Austria

In December 2016 the particle therapy facility MedAustron started to treat patients. It is one of the most advanced treatment facilities in Europe. In full operational mode, approximately 1200 patients per year are planned to be treated. Compared to other facilities, the synchrotron at MedAustron is relatively small with a diameter of 20m. Additionally, the facility will able to produce protons with energies up to 800 MeV/u, which can be used for research applications, and carbon ions with energies up to 400 MeV/u for the treatment. Patient positioning is performed by a robotic positioning system. Besides the treatment rooms, the facility offers the possibility for scientists to use a dedicated radiation room for research purposes. A Phillips Gemini TF PET/CT

scanner can be used for PT-PET measurements after the patient was irradiated [70][71][72][73] [74].

3 MATERIALS AND METHODS

3.1 MONTE CARLO TOOLKIT GATE

The open-source toolkit GATE is developed by the international OpenGATE collaboration and is a common framework for Monte Carlo simulations since 2004. Originally created for the assistance of single photon emission computed tomography (SPECT) and PET, it was later on extended for radiation therapy applications as well [75]. GATE encloses the MC based framework Geant4, allowing a user-friendly setup for the development of simulations. It is a macro language and easy to adopt for nuclear physic scientists and other field of applications [76].

The architecture of GATE consists of a layer structure, which is based on Geant4 (see Figure 22). The developer layer defines which tools can be used and determine how and what a developer can do. It consists of the core and application layer, which are essential base classes. In the core layer physics interactions, event generation, and visualization is defined, as well as the GATE virtual clock, important feature for time management. Thus, this layer is essential for the basic mechanism definitions. The second developer layer, the application layer, uses base classes from the previous ones to model specific geometric objects or physical processes. The development of new features for GATE applications, are carried out in this layer. In the user layer, predefined scripts can be used by the user or a command interpreter, to work interactively. Due to the fact, that each class contains specific extensions and therefore an easy scripting language, the end-user does not need any C++ knowledge.
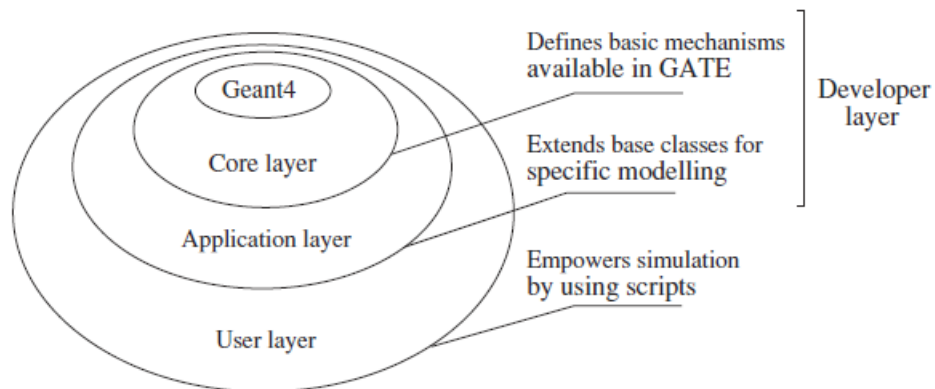
Figure 22: Architecture of the GATE structure *[77]*.

3.2 MATLAB

Matrix **lab**oratory (MATLAB) by The MathWorks Inc. Natick, MA, USA, is a fourth generation programming language implemented in a numerical analysis environment for technical computing and was developed in 1984 [78]. It is used for numeric calculations, data analysis, visualization, algorithm programming, software development and other fields of application, based on MATLAB scripting language [79]. The extensive library, predefined functions and objective-orientated programming, make technical programming more efficient and easier. Interfacing with other programming languages offers the user to work with special programs in their specific language and couple them in MATLAB. It can be used either interactive with the command window or with text files containing the code.

MATLAB is capable of working with matrices and matrix operations, and with its graphical operations it became an impactful tool in image processing [80]. Furthermore, it can process Digital Imaging and Communications in Medicine (DICOM) files, the standardized image format for medical images. The feasibility to handle DICOM files offers an alternative for medical image processing [81].

3.3 GATE SIMULATIONS

In this thesis, GATE v7.1 with Geant4.10.2 was used for all simulations.

First, simulations with polymethylmethacrylat (PMMA) phantoms for the verification of the proper physical models were performed. Second, phantoms with varying material thicknesses were used to measure the change in β^+-activity and dose distributions. At the end, more complex treatment planning simulations of a prostate patient were carried out. The data analysis and data processing was performed, using MATLAB version 9.0.0.341360 (R2016a).

3.3.1 BASIC PARAMETERS IN GATE

GATE simulations are very sensitive to different parameter settings, such as *SetCutInRegion* and *SetMaxStepSizeInRegion* or readout parameters, which effects

simulation time and precision. The *SetCutInRegion* parameter determines a value below which no secondary particles are created. This threshold is set for charged particles processes, such as ionization and Bremsstrahlung, to avoid infrared divergence. The value is set as a distance, which is internally converted to an energy threshold for different materials [82]. The default setting in GATE is 1 mm and was set to 0.1 mm in this thesis. The *SetMaxStepSizeInRegion* determines the distance between two processes and can be considered as a fixed distance. Reducing this value leads to an increment in simulation time, due to the fact that more processes for one particle can occur until reaching its endpoint.

Other important parameters are readout parameters, also called actors. They are used to collect data from interactions of particles with matter in simulations. Depending on the type of actor, energy deposition, dose deposition or number of created particles can be stored. In general, actors are attached to a volume and can be set to collect data in different formats, after a specific time or a number of events, different resolution or the voxel size.

3.3.2 PHYSICS LISTS AND DOSE & ACTIVITY DISTRIBUTIONS

The so called, physics lists in GATE are predefined physical models which can be selected depending on the area of application. They are essential in simulations for the nuclear and electromagnetic interaction processes and production of particles. Single handedly chosen physical models can be used for simulation, but due to the complexity and variety, it is recommended to use one of the predefined physics lists provided by GATE. As an example, a commonly used physics list in proton beam therapy is called "QGSP_BIC_HP_EMZ", where QGSP stands for Quark Gluon String model, BIC for Binary Cascade model and HP means High Precision Neutron model [83] [84]. The suffix "EMZ" at the end represents the accuracy of electromagnetic processes.

Dose and positron emitter distributions in GATE are acquired by attaching actors to the desired volume. The most important actors used in this thesis were *ProductionAndStopping, CrossSectionProduction* and *Dose* actor. For the determination

of number of produced β^+ particles, the *ProductionAndStopping* actor was used. The collection of produced ^{11}C and ^{15}O particles, and therefore the β^+-activity distribution, was done with both production actors, whereas dose or energy deposition have been stored by the *Dose* actor. Although both actors are able to collect activity distributions, they handle interaction processes differently. The *ProductionAndStopping* actor creates a 3D image by storing the positions of the particles where they were produced and stopped. The *CrossSectionProduction* actor on the other hand uses the flux of the particles calculated by MC, in combination with the cross-section data from experimental results [85].

For the analysis of the dose and the β^+-activity distribution results, the so called R_{50} value was used. It describes the range at 50% of the maximum number of produced positron emitter production in the distal fall off region. The R_{50} for the dose profiles, stands for the range, where the relative dose is 50% of the total dose at the distal side of the Bragg-peak [86].

3.3.2.1 PHANTOM DESIGN

The basic setup for the physics lists verification was a 100 mm × 100 mm × 400 mm PMMA phantom, irradiated with a proton beam of 10^6 particles (see Figure 23) at 110, 140 and 175 MeV. 16 different physic lists have been simulated and the number of produced β^+ particles via *ProductionAndStopping* actor investigated.

For the β^+-activity and dose distribution simulations, the data was stored with the *CrossSectionProduction* and *ProductionAndStopping* actor and the dose with the *Dose* actor. The dimension of this setup was a 90 mm × 90 mm × 300 mm phantom, which was irradiated with a proton beam with 10^7 particles at 140 MeV. Two basic versions of this phantom with varying materials were simulated. The shifting range of the Bragg-peak and R_{50} value of the ^{11}C and ^{15}O distributions was analysed. The first setup was a simplified water phantom of 50 mm thickness combined with a skull bone insert of varying thickness (i.e. 0.5, 1, 2, 3, 4, 5, 6, 7, 8, 9, 10, 20, 30, 40, 50 mm), see Figure 24. In Figure 25, a schematic illustration of the second setup can be seen. Again, the first

50 mm of the phantom consisted of water, followed by 10 mm skull bone. Behind the bone, a varying air slices was attached. The thickness of these slices varied between 0.5 and 30 mm. For ranges between 10 mm to 30 mm 5 mm steps was used, while a 1 mm step size was introduced for the ranges between 1 mm to 5 mm. The rest of the phantom (i.e. 210 – 239.5 mm) consisted of brain matter.
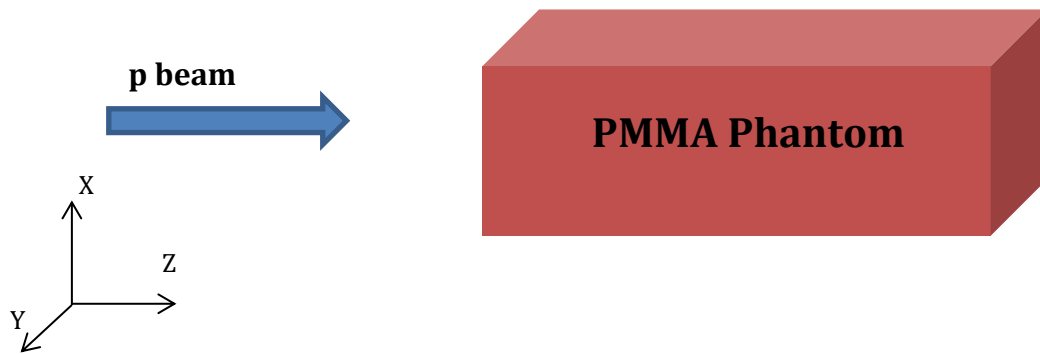
Figure 23: Illustration of PMMA phantom irradiated with a proton beam and data stored via *ProductionAndStopping* actor.
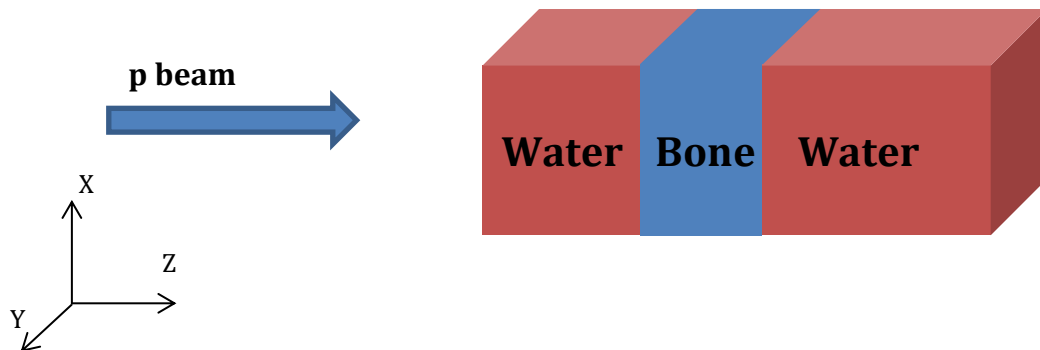
Figure 24: Water phantom with varying bone thickness from 0.5 – 50 mm irradiated by a proton beam. Activity and dose distributions saved by *ProductionAndStopping* and *CrossSectionProduction* actor.
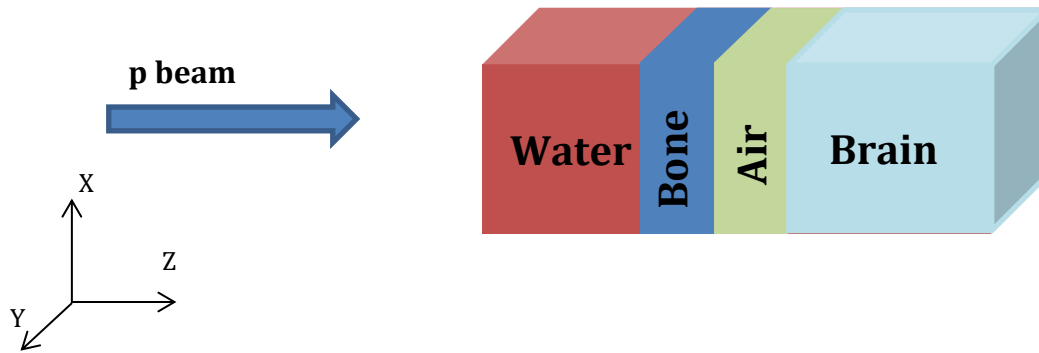
Figure 25: Simple phantom consisting of water, bone, air and brain matter. The air slices varied from 0.5 – 30 mm, affecting the thickness of the brain matter accordingly. Activity and dose distributions were saved by the "*ProductionAndStopping*" and "*CrossSectionProduction* " actor.

3.3.3 TREATMENT PLANNING SIMULATIONS IN GATE

Treatment planning (TP) simulation setups acquire additional settings and inputs, compared to simulations with homogenous phantoms. Starting with the source, a so called *TPSPencilBeam* is commonly used. It is a source-type for active beam scanning delivery techniques, to simulate real treatment plans in GATE. Furthermore, the type of particles in TP simulations can be defined, as well as the distance of the beam deflectors and the distance of the nozzle exit to the isocenter of the target. The next important preference is the treatment plan, which contains valuable information about the isocenter, gantry angle, patient support angle, number of fields, number and particle energy of scanned spots. Lastly, the irradiated CT, which contains the anatomical information of the patient, can be translated or rotated inside the regular volume of the simulation. However, it is recommended to locate the CT at the isocenter for the simulation.

3.3.3.1 FUNDAMENTAL SETTINGS IN TP SIMULATIONS WITH GATE

The basic parameter setups for TP simulations with GATE in this thesis were utilized for all TP simulations. The source type was a *TPSPencilBeam* with protons. The distance of the Nozzle to the isocenter was set to 650 mm. Important parameters in TP simulations

affecting time and simulation resource consumption of the operating system were: steps size, resolution or the voxel size of the output and the number of irradiated spots.

3.3.3.2 Single-Field TP Simulations

The main goal was to use a sufficient number of primary particles for TP simulations, to achieve reasonable statistical results. With a varying quantity of primary particles (i.e. $10^5 - 10^6$ in 10^5 steps and $10^7 - 10^8$ in 10^7 steps) the distal and lateral depth R_{50} and the R_{80} were explored for the dose and activity profiles. The resulting data was extracted from a single slice in posterior and anterior as well as in superior and inferior direction, to obtain the values of the β^+-activities.

The statistical uncertainty of the deposited dose was calculated using the formula

$$s^2 = \frac{1}{N^2} \left[N \sum_{i=1}^{N} d_i^2 - \left(\sum_{i=1}^{N} d_i \right)^2 \right]$$

(9)

where N stands for the total number of interactions and d_i the deposited energy in the i-th voxel.

Furthermore, two different Hounsfield Units (HU) scales were used. The default HU scale from GATE and the HU scale from RayStation (see Table 3). Additionally, the stored data was investigated with the *ProductionAndStopping* and the *CrossSectionProduction* actor.

GATE scale		RayStation scale	
HU	density [g/cm³]	HU	density [g/cm³]
-1000	1.21×10^{-3}	-1000	1.21×10^{-3}
-98	0.93	-992	1.21×10^{-3}
-97	0.93	-976	1.21×10^{-3}
14	1.03	-480	0.5
23	1.031	-96	0.95
100	1.119	48	1.05
101	1.076	128	1.1
1600	1.964	528	1.35
3100	2.8	976	1.6
		1488	1.85
		1824	2.1
		2224	2.4
		2640	2.7
		2832	2.83
		2833	2.87
		3096	2.87

Table 3: HU scale from GATE and RayStation.

4 RESULTS AND DISCUSSION

First, the produced β^+ particles in PMMA phantoms with the available physics lists are evaluated. The second sub-section deals with the statistical uncertainty in MC simulations. Chapter 4.3 addresses dose and activity distribution simulations with homogenous phantoms, influenced by varying material inserts. In chapter 4.4. HU scales are compared and discussed. The final chapter 4.5 deals with the final single field TP simulations.

4.1 PHYSICS LIST SIMULATIONS

The yield of β^+–emitters in a PMMA phantom simulated with different physics lists are displayed in Table 4, with the aim to obtain the best suited list for beta plus distribution simulations. Lists highlighted in red reveal good conformity to the experimental results from Parodi K. et.al. [2]. Figure 26 and Figure 27 visualizes the derivation from Table 4. The decision was made to use the QGSP_BIC_HP physics list, as it shows the best accordance at all energies and for all positron emitters.

Physics lists	110 MeV			140 MeV			175 MeV		
	^{11}C × 10^{-2}	^{10}C × 10^{-2}	^{15}O × 10^{-2}	^{11}C × 10^{-2}	^{10}C × 10^{-2}	^{15}O × 10^{-2}	^{11}C × 10^{-2}	^{10}C × 10^{-2}	^{15}O × 10^{-2}
FTF_BIC	2.12	0.15	0.69	2.87	0.23	0.97	3.79	0.33	1.33
FTFP_BERT	0.74	0.07	0.31	1.07	0.1	0.45	1.48	0.15	0.64
FTFP_BERT_HP	0.74	0.07	0.32	1.07	0.1	0.45	1.52	0.15	0.66
FTFP_BERT_TRV	0.74	0.07	0.30	1.05	0.1	0.45	1.48	0.15	0.62
FTFP_INCLXX	1.74	0.14	0.56	2.33	0.2	0.77	3.08	0.28	1.04
FTFP_INCLXX_HP	1.76	0.13	0.58	2.4	0.2	0.8	3.14	0.29	1.07
LBE	0.74	0.07	0.30	1.05	0.1	0.45	1.50	0.15	0.64
QBBC	2.13	0.15	0.7	2.91	0.23	0.92	3.77	0.34	1.32
QGS_BIC	2.15	0.15	0.69	2.90	0.23	0.99	3.82	0.33	1.33
QGSP_BERT	0.74	0.07	0.31	1.05	0.1	0.43	1.45	0.16	0.63
QGSP_BERT_HP	0.76	0.07	0.31	1.04	0.11	0.45	1.51	0.15	0.65
QGSP_BIC	2.13	0.15	0.7	2.87	0.23	0.96	3.78	0.33	1.31
QGSP_BIC_HP	2.16	0.14	0.71	2.9	0.24	0.98	3.86	0.34	1.34
QGSP_FTFP_BERT	0.74	0.07	0.31	1.06	0.1	0.44	1.49	0.14	0.63
QGSP_INCLXX	1.77	0.13	0.57	2.38	0.2	0.78	3.09	0.29	1.05
QGSP_INCLXX_HP	1.74	0.13	0.57	2.37	0.2	0.8	3.16	0.29	1.05
Experiment [Parodi K. et. al.]	2.2 ± 0.3	0.09 ± 0.3	0.8 ± 0.15	3.4 ± 0.4	0.15 ± 0.03	1.23 ± 0.18	4.7 ± 0.7	0.17 ± 0.06	1.6 ± 0.3

Table 4: Production of positron emitters, per beam-particle with available physics lists. Highlighted lists are in the tolerance range of the reference data.

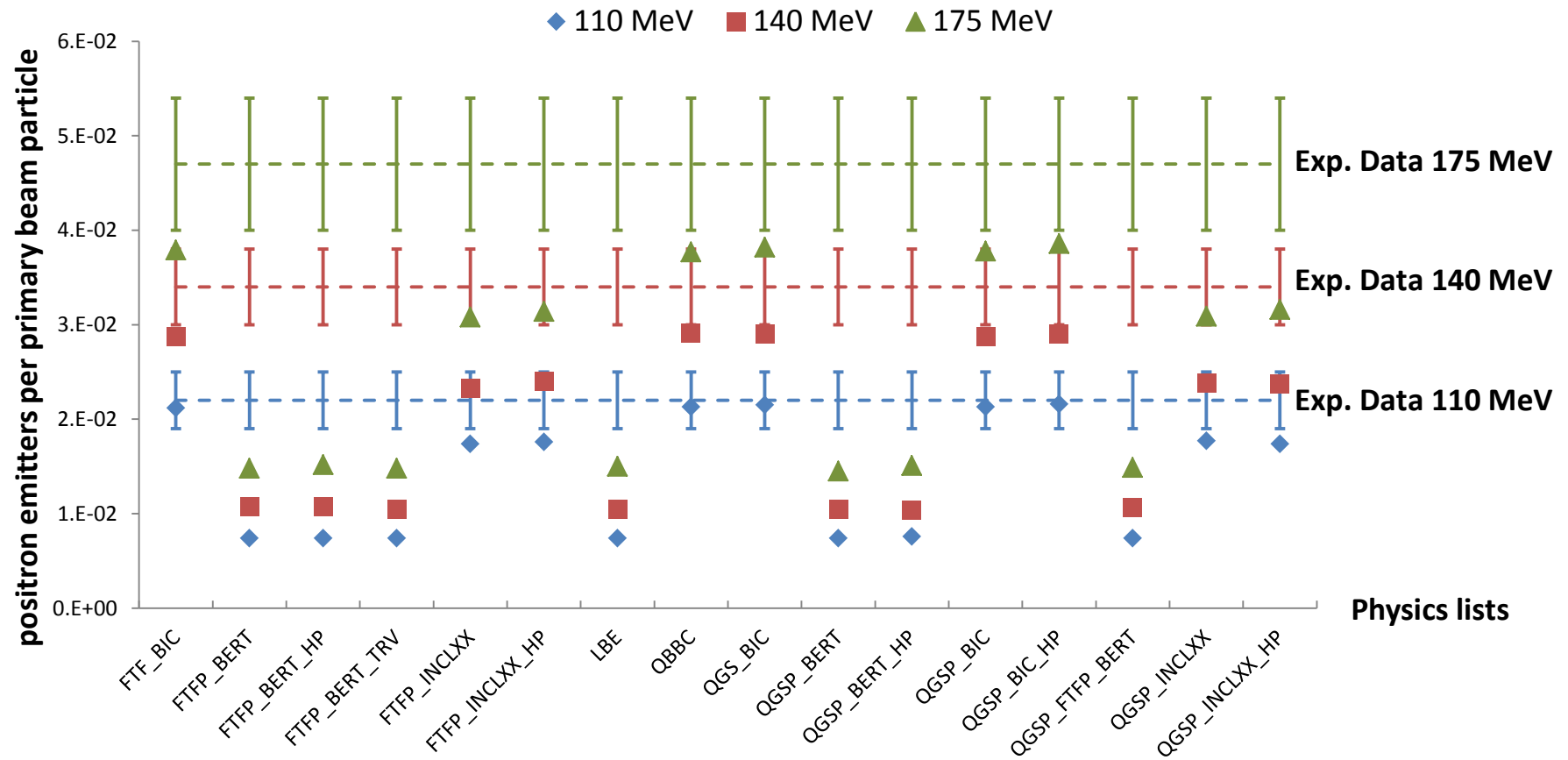Figure 26: Influence of different physic lists in a PMMA phantom irradiated with protons. The number of produced ^{11}C positron emitters at 110, 140 and 175 MeV displayed with the corresponding experimental results and their related tolerance limits.
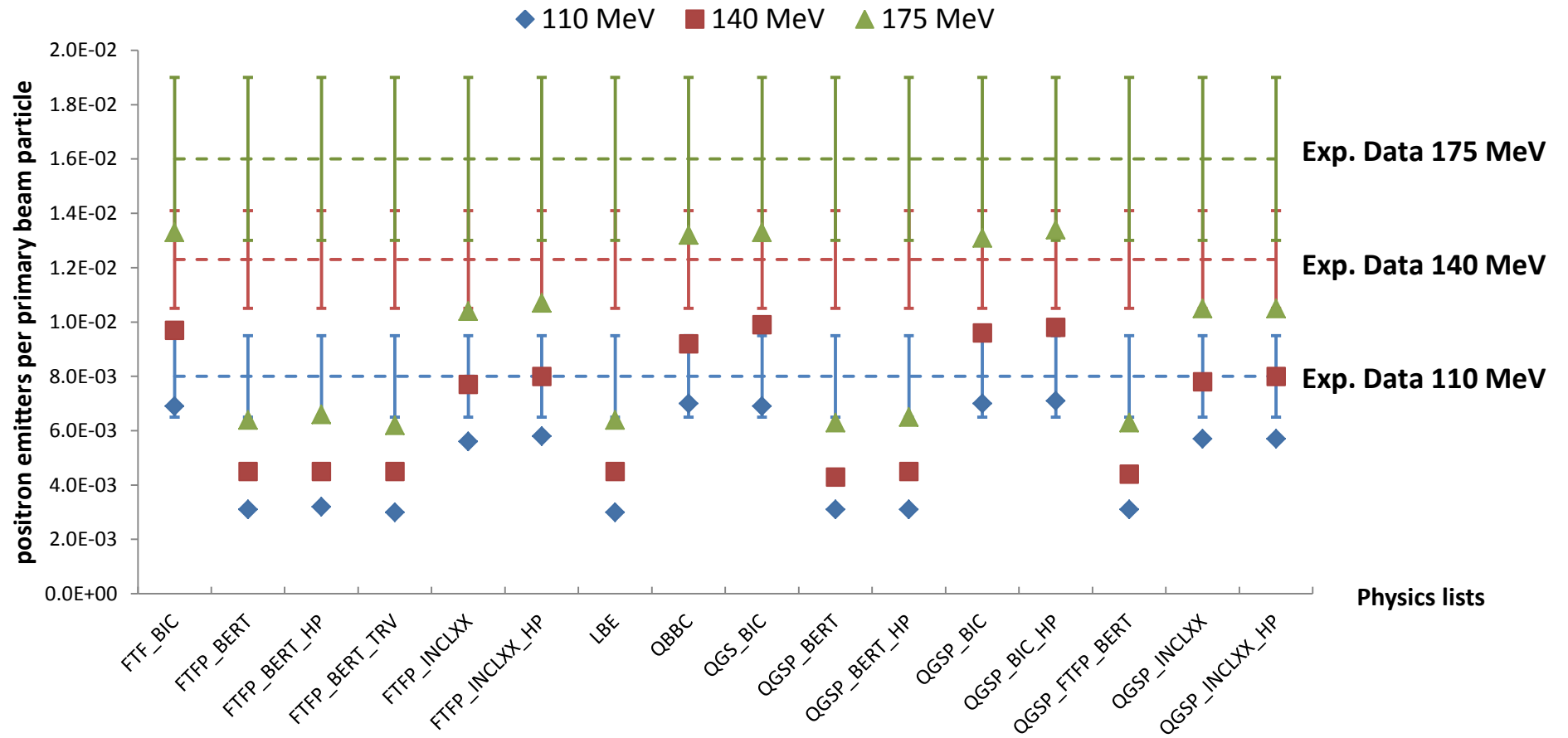
Figure 27: Influence of different physic lists in a PMMA phantom irradiated with protons. The number of produced ^{15}O positron emitters at 110, 140 and 175 MeV displayed with the corresponding experimental results and their related tolerance limits.

4.1.1 DISCUSSION

As Figure 26 and Figure 27 reveal, the aberrance to the experimental results for all physic lists increases, with increasing particle energy. The combination of the Fritiof and the Bertini Cascade models (FTFP_BERT) showed high variances reaching up to 68.1% for ^{11}C and 68.5% for ^{15}O to the mean value of the experimental results. This was caused by the fact that this model is mainly used in high energy physics such as Large Hadron Collider experiments (LHC), making the Fritiof and Bertini cascade unsuited for particle therapy simulations. The INCLXX models showed results from 19.5% at 110 MeV up to 34.3% at 175 MeV for ^{11}C particles and 28.8 – 34.4% for ^{15}O at 110 – 175 MeV. Thereof, at low energies the results deviate less than at higher ones. Similar to the FTFP_BERT models, the INCLXX model is used in high energy physics experiments. Physics lists with the implemented Quark Gluon String model (QGS) were designed for fragmentation processes and strongly depend on the addition of other models. The additionally implemented Binary Cascade model (BIC) to the QGS model, showed superior results over other physic lists, indicating physics lists with the BIC model are more suited for simulations with proton beams, as stated by the OpenGATE collaboration [83].

A deviation of 1.8 % for 110 MeV to 17.8 % for 175 MeV and for ^{15}O from 11.3 % for 110 MeV to 16.3 % for 175 MeV was measured for the QGSP_BIC_HP_EMZ physic list. Thus, it was decided to use the QGSP_BIC_HP_EMZ physic list in this thesis because, the number of produced positron emitters at different energies showed the least deviation to the experimental results, compared to the other physic lists.

The evaluation of the simulation results for ^{10}C emitter are not represented, due to the fact that the number of produced emitters is very low for all physic lists and consequently did not yield any applicable statistical results.

4.2 STATISTICAL UNCERTAINTY

In this sub-chapter, the influence of primary particles on the uncertainty distribution is displayed. Two different step sizes with different numbers of primary particles have been analysed. For the 0.1 mm step size simulations, $10^5 - 10^6$ incident particles in 100k steps and for the 0.01 mm simulations, $10^5 - 5\times10^5$ primary particles in 100k steps were evaluated. It has to be considered that, for the 0.01 mm step size simulations only $10^5 - 5\times10^5$ protons per beam were carried out, due to much longer simulation times, than with 0.1 mm step size.

A single slice (500 × 500 mm²) in a three dimensional data set was extracted approximately in the centre of the proton beam in frontal and transverse plane. Figure 28 displays the plane at which the statistical uncertainty was evaluated from. Note that, evaluating all of the remaining slices from a three dimensional data set was not necessary. With the examination of the centre slice the areas of interest were covered, which was the centre of the beam path.

The relationship between the statistical uncertainty and dose distribution is shown in Figure 29. The red line shows the SOBP of the deposited dose and the blue dots represent the statistical uncertainty throughout the patient. The simulation was carried out with 5×10^5 primary particles and a step size of 0.1 mm.
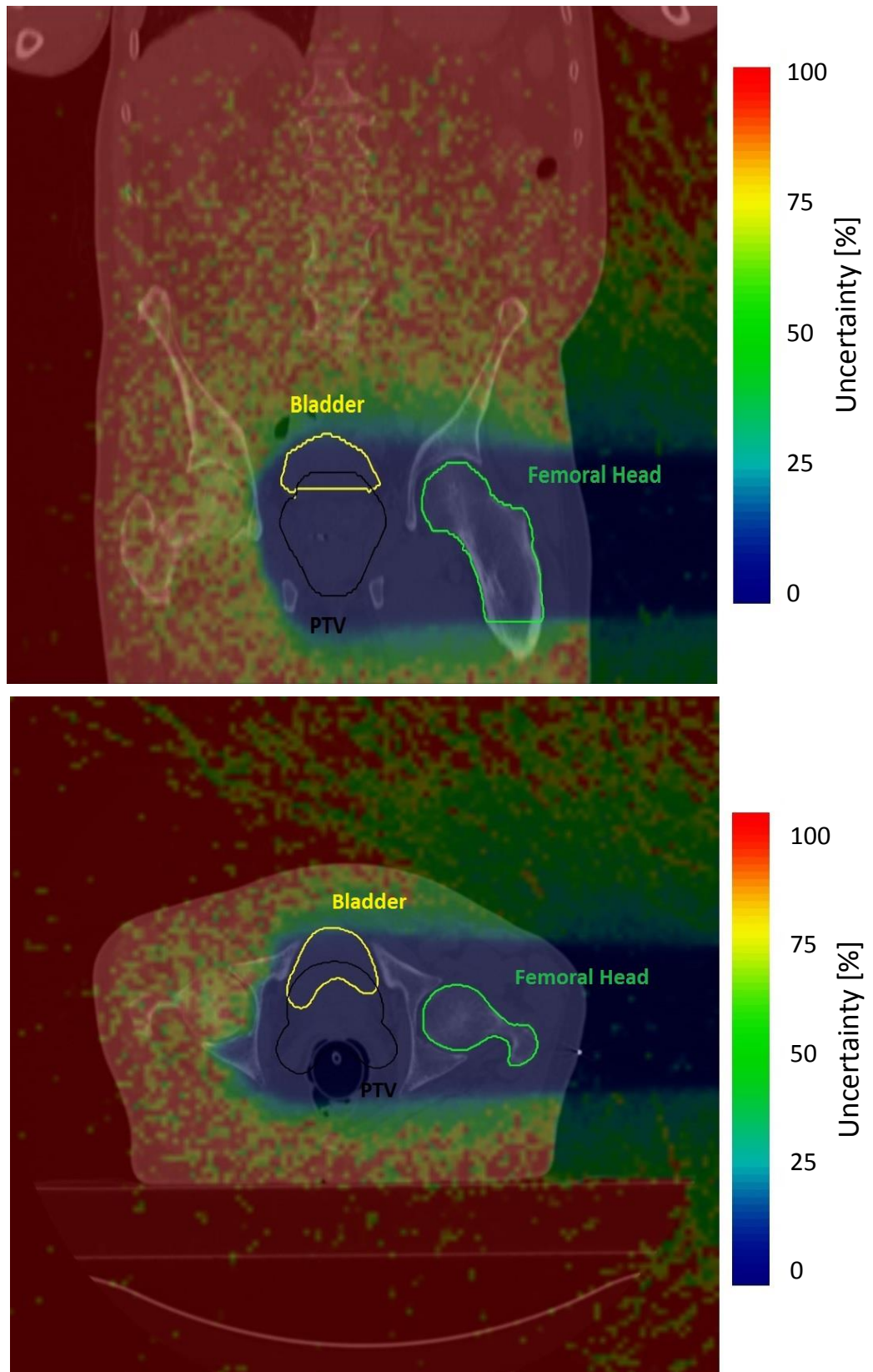
Figure 28: Frontal plane (top) and transversal plane (bottom) view of a two dimensional uncertainty distribution of a proton beam with a 0.1 mm step size and 10^6 primary particles. Contours of important organs and structures have been highlighted.
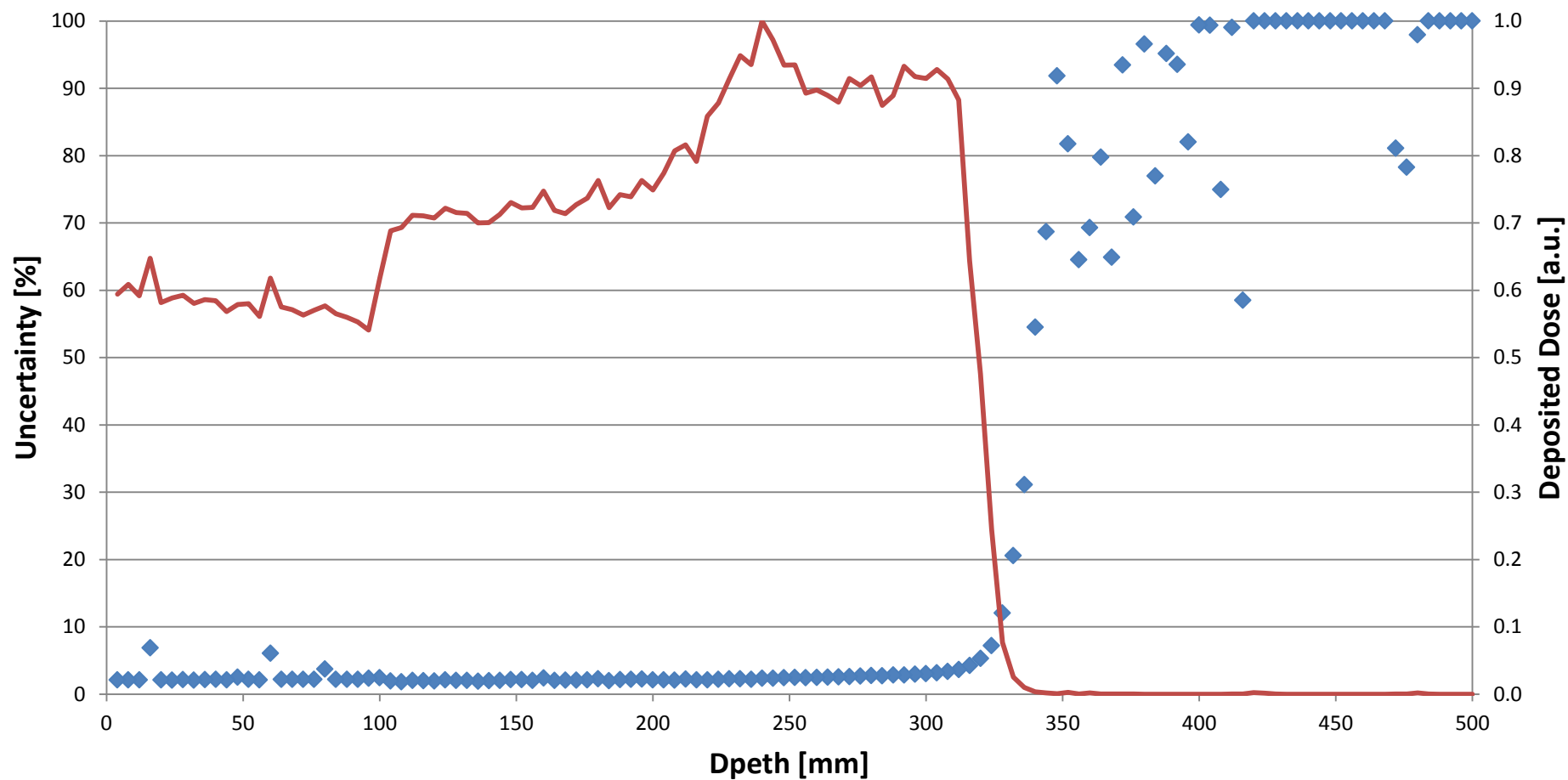
Figure 29: Uncertainty distribution of a proton beam (blue dots, left hand axis) and the associated normalized to the maximum dose deposition (red line, right hand axis). Both simulated with $5x10^5$ protons.

Figure 30 shows the reduction of the uncertainty with increasing particle numbers in a small region of the beam path. The uncertainty at the depth of 180–280 mm was chosen, because of the least statistical outliers. Table 5 lists the mean values and the tolerances of the uncertainty with the corresponding quantity of primary particles.
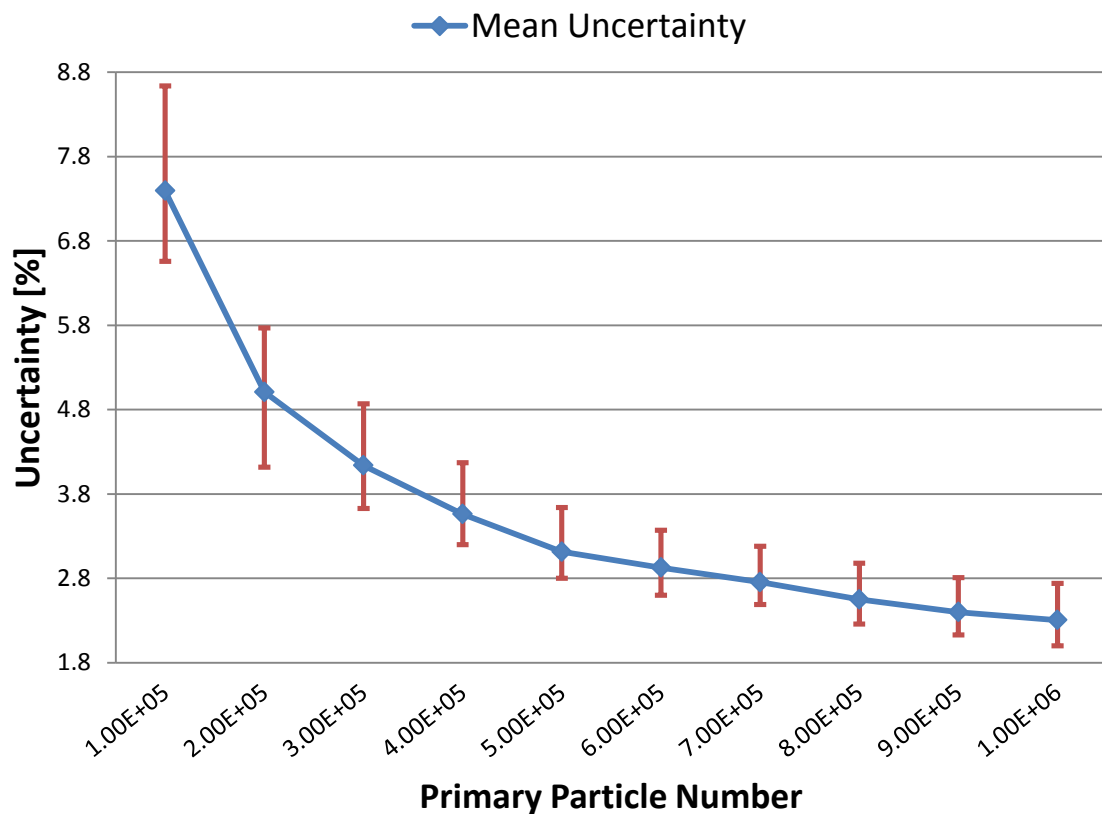

Figure 30: Mean uncertainty in a range of 180–280 mm with different quantities of protons per beam and a step size of 0.1 mm. Error bars result from the uncertainty in the range of 180–280mm.

Primary particle number	Mean uncertainty [%]	Max. uncertainty [%]	Min. uncertainty [%]
1×10^5	7.40	8.64	6.56
2×10^5	5.01	5.77	4.12
3×10^5	4.14	4.87	3.63
4×10^5	3.56	4.17	3.20
5×10^5	3.12	3.64	2.80
6×10^5	2.93	3.37	2.60
7×10^5	2.75	3.18	2.49
8×10^5	2.55	2.98	2.26
9×10^5	2.40	2.81	2.13
1×10^6	2.30	2.74	2.00

Table 5: Mean uncertainty in the range of 180–280mm with the additional tolerances and a step size of 0.1 mm.

In Figure 31 shows depth profiles of produced C^{11} particles in distal direction of the beam with different quantities of protons per beam. The figure shows the influence of primary particles on the fluctuations of produced C^{11} positron emitter.
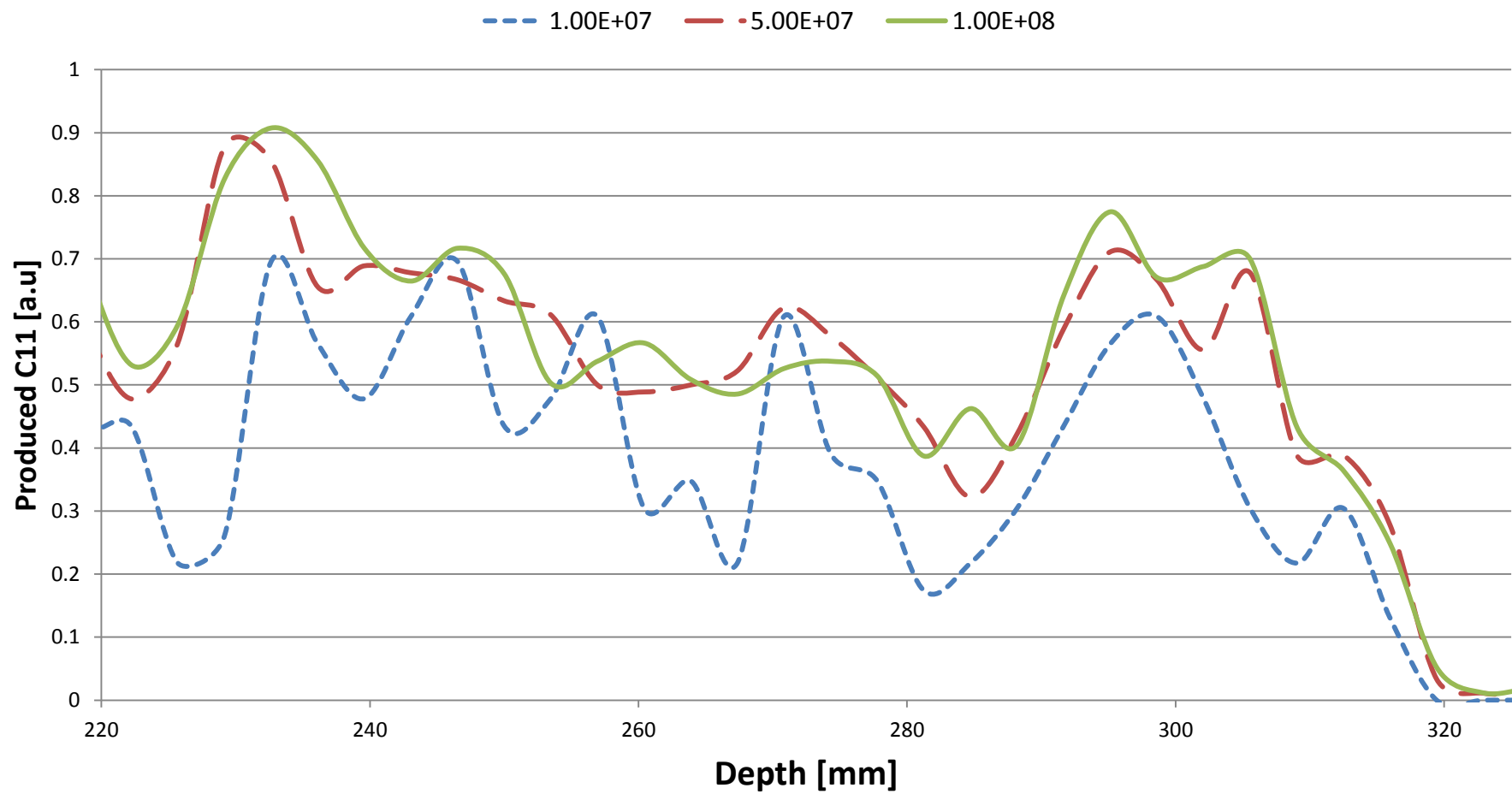
Figure 31: Comparison of produced C^{11} particles in distal direction of the incident beam with different numbers of primary particles. Values were normalized to the maximum.

4.2.1 STATISTICAL ANALYSIS

This sub-chapter focuses on the analysis of the statistical uncertainty distributions influenced by the quantity of the primary particles with a voxel resolution of 4mm. Additionally, a comparison of two step sizes, namely 0.1 mm and 0.01 mm was carried out to observe irregularities between them.

The first observation by analysing Figure 29 was the increment of the uncertainty after the distal penumbra. Before reaching this critical point, the uncertainty remains very low and constant. Behind the distal penumbra, the uncertainty experiences oscillations. The expected oscillations at greater depths results from the low number of primary particles and the consequently near-zero value of deposited dose [75].

Another confirmed expectation was that with increasing primary particle numbers the uncertainty decreased (see Figure 30). Furthermore, the uncertainty decreases from ~7% with 10^5 primary particles to ~2% with 10^6 particles. Besides the overall reduction of the uncertainty, the statistical oscillations in the beam region reduces as well, which can be seen in Table 5.

Similar uncertainty distributions, but slightly higher than those from the 0.1 mm step size simulations were observed for the 0.01 mm step size results. A decrement of approximately 7% for 10^5 primary particles to 3% for 5×10^5 protons per beam was measured. The reason for the higher uncertainty of the 0.01 mm over the 0.1 mm step size parameter is due to the fact that, primary particles interact more often over the same distance. Consequently, this leads automatically to a higher statistical uncertainty of the beam.

In the end it can be stated that an uncertainty of approximately 2.3%, results in a good compliance with other scientific results, which reported an uncertainty of 2-5% [5] [87] [88] [89]. From the comparison of the 0.1 mm and 0.01 mm step sizes, it can be concluded that the smaller step size configuration does not contribute to any improvement of the uncertainty. Moreover, simulations with 0.01 mm step size take

four times longer on a single 3.7 GHz CPU to simulate than 0.1 mm step size simulations. For the other important parameter, namely the primary particle number per beam, strong dependencies were observed. Higher quantities of protons than 10^6 would lead to a lower uncertainty than 2%, which shows the tendency in Figure 30, but would not reduce further drastically. It can be concluded that the necessary number of primary particles for reasonable statistical results is achieved with 10^6 protons per beam and higher. This can be confirmed with the reduction of the fluctuations of produced C^{11} particles in Figure 31. It leads to the expected conclusion that with 10^8 primary particles the least fluctuations were achieved. In that context a statistical uncertainty below 2% was accomplished.

4.3 DOSE AND ACTIVITY DISTRIBUTION SIMULATIONS

The *ProductionAndStopping* (PAS) and *CrossSectionProduction* (CSP) actor were used to study the change of the R_{50} values of ^{11}C and ^{15}O distributions, in relation to the position of the Bragg-peak. Additionally, correlations between those values were investigated, for different simulation setups.

4.3.1 PROPERTIES OF ACTORS IN DIFFERENT MATERIALS

In this sub chapter the behaviour of the β^+-activity distributions in different materials, with different actor, was investigated. In Figure 32 and Figure 33 the number of produced ^{11}C and ^{15}O particles in a PMMA phantom are displayed at different energies for both production actors.

The simulations were carried out at 110, 140 and 175 MeV, with 10^6 particles per beam. As the figures clearly demonstrate, the PAS actor shows an increase at the end of the range. In addition, simulations of a water phantom and a brain tissue phantom can be seen in Figure 34 and Figure 35. Figure 36 shows the deposited energy and the positron emitter production of a 110 MeV proton beam in a PMMA phantom from the literature [90]. The R_{50} values of the produced positron emitters and deposited dose, from the literature and MC simulations, are listed in Table 6. The R_{50} were evaluated with an approximation of a second order polynomial function. The measured numbers of produced positron emitters in the entrance region and at the maximum region, as well as the resulting ratio from the literature and MC simulations is listed in Table 7. Values from the literature were extracted by hand.

54

Figure 32: Activity distributions of ^{11}C particles stored with the *ProductionAndStopping* and *CrossSectionProduction* actor at 110, 140 and 175 MeV in a PMMA phantom.
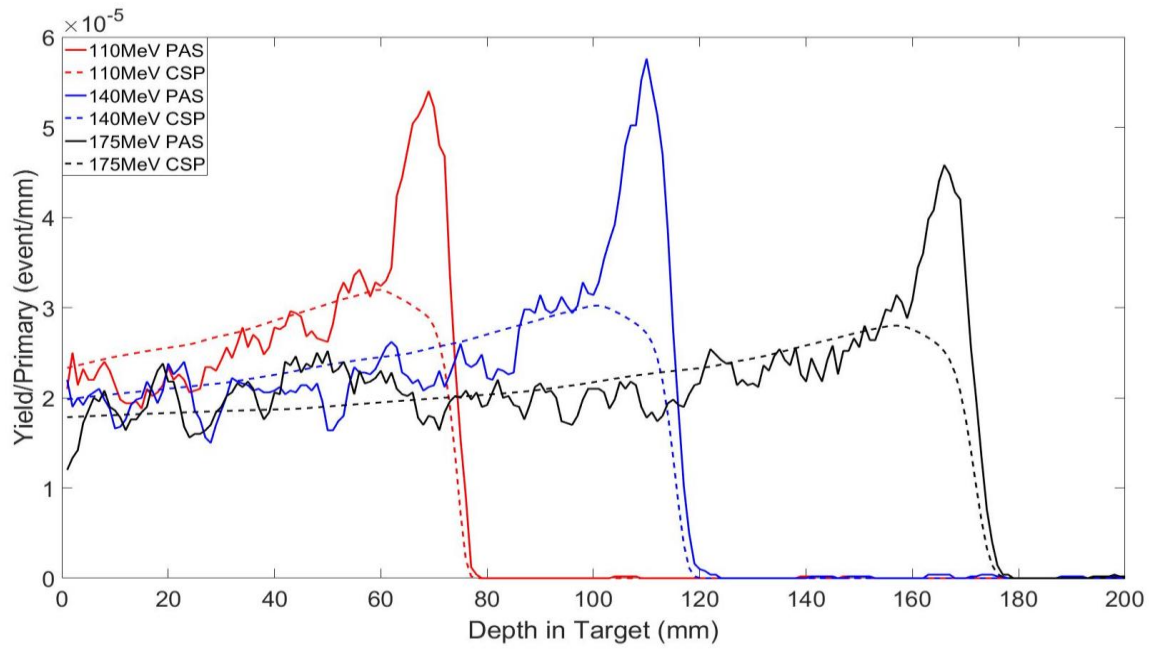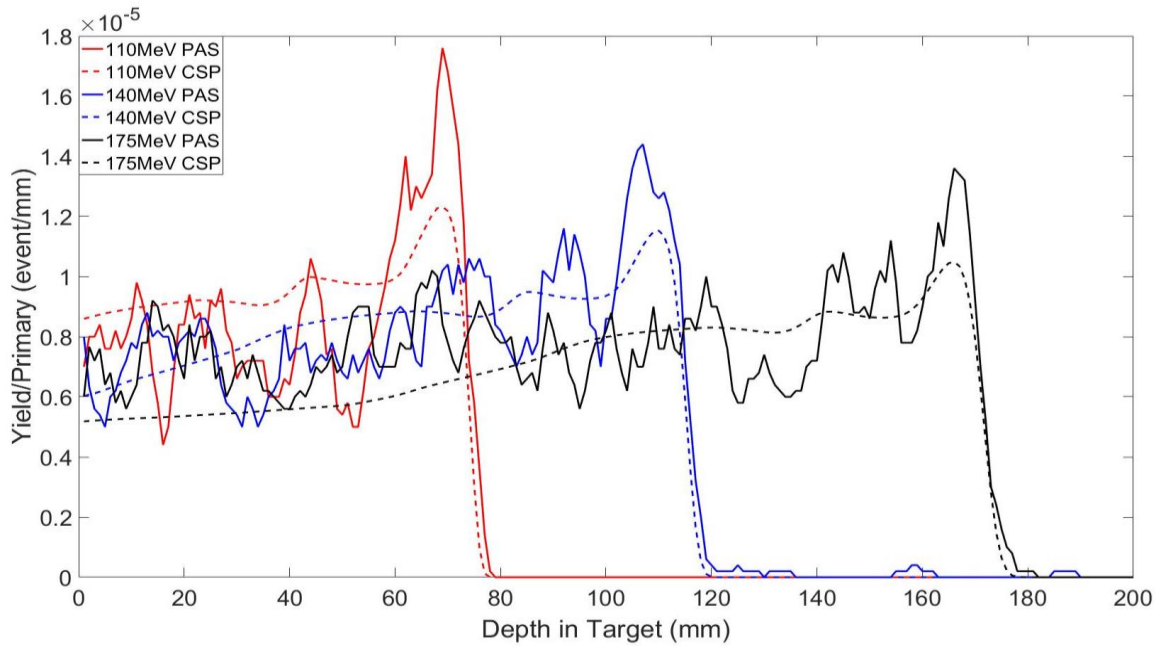

Figure 33: Activity distributions of ^{15}O particles stored with the *ProductionAndStopping* and *CrossSectionProduction* actor at 110, 140 and 175MeV in a PMMA phantom.
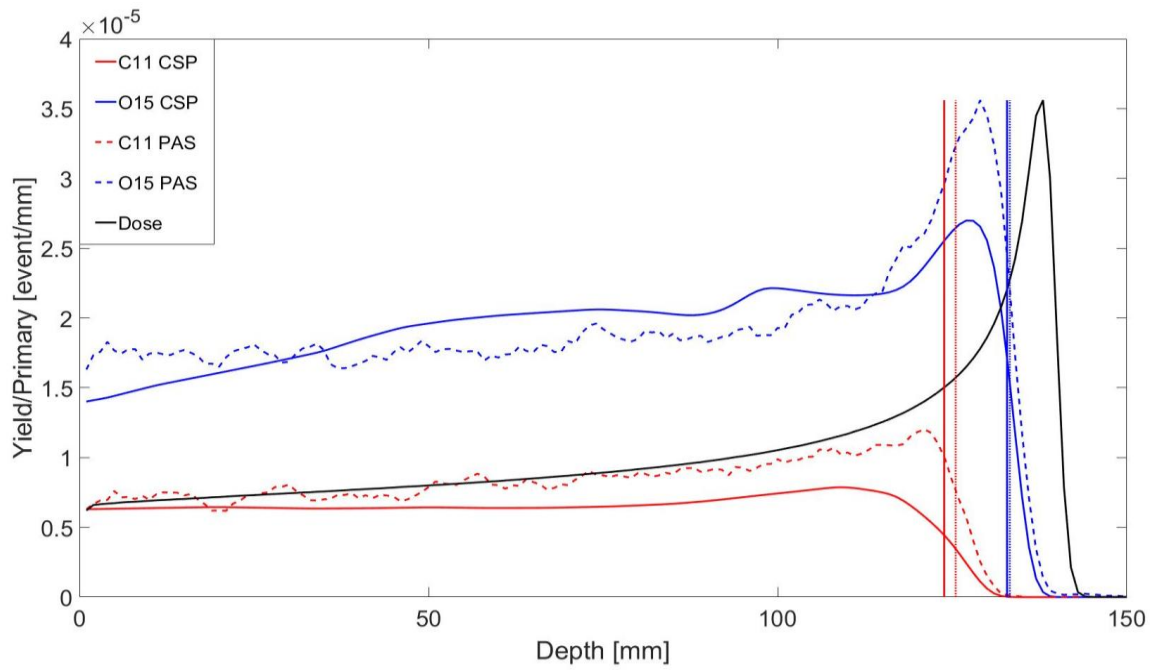
Figure 34: Positron emitter production in a water phantom with a proton beam at 140 MeV. CSP and PAS actor was used to store produced ^{11}C and ^{15}O particles. The deposited dose is shown as reference (black line). Vertical lines show the distance of the R_{50} values for each positron emitter particle.

Figure 35: Positron emitter production in a phantom consisting of brain tissue, with a proton beam at 140 MeV. The deposited dose is shown as reference (black line). Vertical lines show the distance of the R_{50} values for each positron emitter particle.

Figure 36: Depth distributions of β⁺-emitters and deposited energy for a 110 MeV proton beam in a PMMA phantom. Image referring to I. Pshenichov et. al. [90].

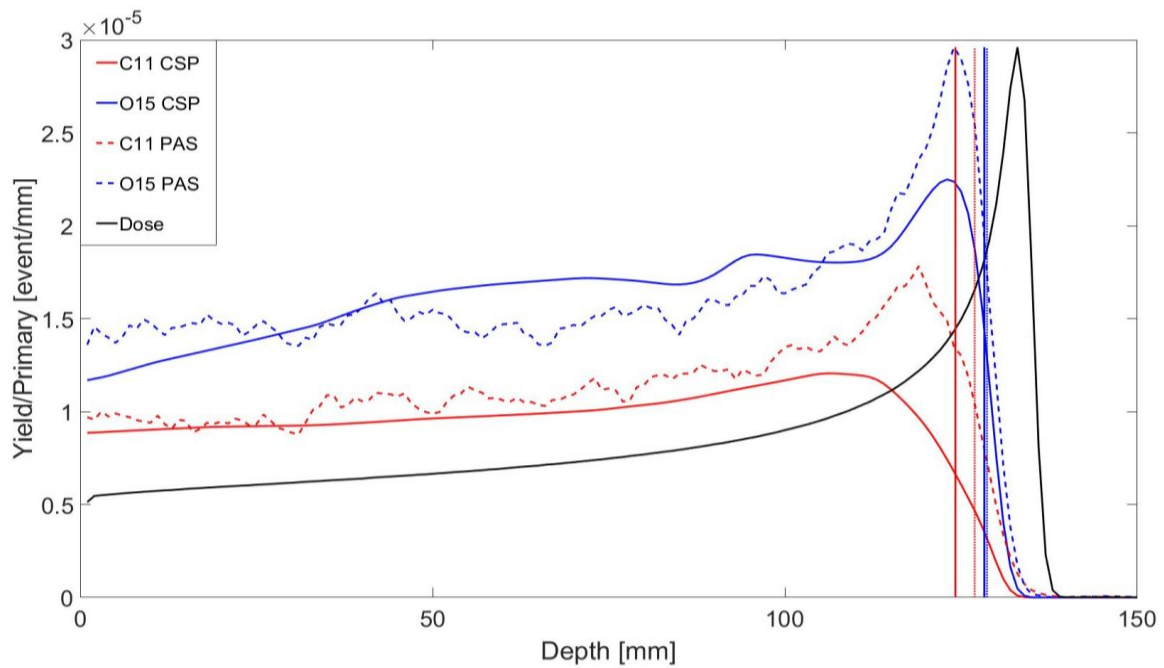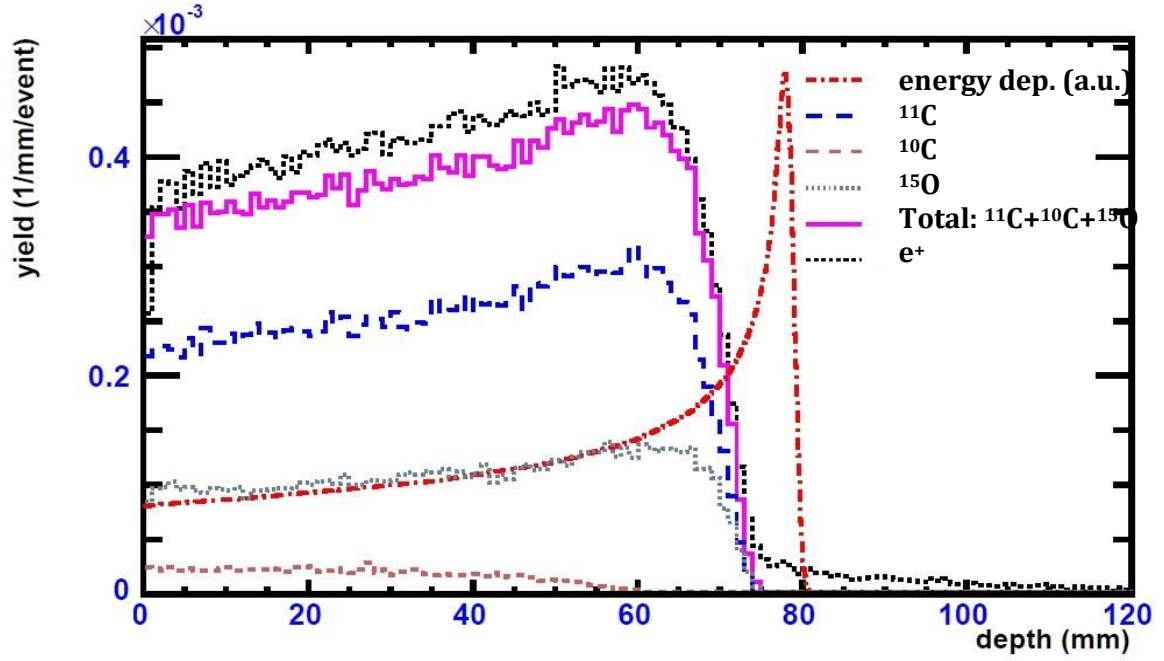| Simulation setup	R_{50} ^{11}C CSP [mm]	R_{50} ^{15}O CSP [mm]	R_{50} ^{11}C PAS [mm]	R_{50} ^{15}O PAS [mm]	R_{50} Dose [mm]
PMMA 110MeV	72.46	73.09	72.91	72.98	78.22
PMMA 140MeV	113.53	114.26	114.33	114.13	119.66
PMMA 175MeV	170.00	170.77	170.44	170.41	176.50
Brain tissue	124.20	128.31	126.93	128.68	134.37
Water	123.85	132.85	125.49	133.25	139.14
I. Pshenichov et. al.	^{11}C [mm]		^{15}O [mm]		R_{50} Dose [mm]
	69		71		78

Table 6: Values of the depth of the R_{50} distance β⁺-activity for ^{11}C and ^{15}O, and the R_{50} value of the dose, for PMMA, brain tissue and water phantom.

Simulation	Maximum region	Entrance region	Ratio
CSP ^{11}C	31.99×10^{-5}	24×10^{-5}	1:0.75
CSP ^{15}O	12.3×10^{-5}	8.8×10^{-5}	1:0.72
PAS ^{11}C	76×10^{-5}	22.27×10^{-5}	1:0.3
PAS ^{15}O	27×10^{-5}	7.82×10^{-5}	1:0.29
I. Pshenichov et. al.	Maximum activity	Entrance region	Ratio
^{11}C	0.32×10^{-3}	0.23×10^{-3}	1:0.72
^{15}O	0.14×10^{-3}	0.09×10^{-3}	1:64

Table 7: Numbers of produced positron emitters at the maximum and mean value at the entrance region (0 – 10 mm), and the resulting ratio.

4.3.1.1 Discussion

Figure 32 and Figure 33 show distributions of produced ^{11}C and ^{15}O particles in a PMMA phantom at different energies, with different production actors. From that several conclusions can be drawn.

First, the PAS actor always shows higher fluctuations than the CSP actor for all energies at all histograms. Although the bin size of the graphs was 1mm and a smoothing by a moving average filter in MATLAB was applied, the fluctuations still remained relatively high due to statistical variance. Consequently, the comparison of the β^+-activity distributions with a higher resolution of 0.1 mm was impossible. The second major observation was the strong increment of produced particles at the end of the range for the PAS actor. The last observation was that the range of maximum number of positron emitters was smaller than the range of the Bragg-peak falls off, by means of depth in the phantom [49] [91] [92].

For other materials (see Figure 34 and Figure 35), the relative number of produced positron emitters between booth actors at the end of the range remains relatively high to the number of produced particles at the entrance region of the phantom. This implies a strong material dependency for the production of positron emitters.

The fact that the number of produced ^{15}O particles is higher than those of ^{11}C particles for the brain tissue phantom results from the material composition defined in GATE. It is mainly composed of 10.7% hydrogen, 14.5% carbon and 71.2% oxygen, which causes a higher production of oxygen positron emitters due to a dominant availability of oxygen in the material. Whereas in the PMMA phantom the material is composed of 60% carbon, nearly 32% oxygen and only 0.08% hydrogen. This leads to a higher production of ^{11}C particles over ^{15}O. This lead to the conclusion that both actors showed the same behaviour for both materials. Thus, for phantoms consisting of a single material, both actors resulted to be correct. The question about behaviour of the *ProductionAndStopping* and *CrossSectionProduction* actor in phantoms with more than one material composition is discussed further below in the next sub-chapter.

The R_{50} range of produced positron emitters and deposited dose from Table 6, resulted in a better accordance with the measured values from Igor Pshenichnov et. al. for the *CrossSectionProduction* actor compared to the *ProductionAndStopping* actor. The values deviated less than 3 mm for the positron emitters and less than 1 mm for the deposited dose. It has to be taken into consideration that the values from the literature were measured by hand.

Comparing the ratio of produced particles at the entrance region (e.g. 0-10 mm depth) and at the maximum, as well as the relative distance between the maximum of produced positron emitters of ^{11}C and ^{15}O, distinct variances for the CSP and PAS actor were observed. With the experimental results from Igor Pshenichnov et. al. (see Figure 36), the ratios from the GATE simulation (see red lines in Figure 32 and Figure 33) resulted in good compliance for the CSP actor. Whereas the PAS actor yielded higher deviations from the experimental results, caused by the characteristic increment in produced particles at the end of the range. Table 7 lists the resulting ratios of the simulation and the experiment. The factor 10^2 difference in terms of produced particles is probably caused by the fact that a higher amount of primary particles were used by I. Pshenichov et. al. [90].

In the end it can be stated that the overall number of produced β^+-emitter is nearly the same, upon reaching the maximum, for both actors. The deviations between the actors results from different crosssections. However, the *CrossSectionProduction* actor shows a more accurate behaviour for the β^+-activity production at the end of the range, leading to a favouring of the CSP actor over the PAS actor.

4.3.2 PHANTOM SIMULATION WITH INSERTS

In the following sections, β^+-activity and dose distributions of phantoms with varying material inserts are illustrated. The results were explored with the different production and dose actors.

Figure 37 and Figure 38 show the occurrence of positron emitters, influenced by the varying bone slice thickness (see Figure 24). The second phantom setup contained varying air layers with a consistent bone slice and brain material at the distal side of the beam entrance (see Figure 25). The number of produced positron emitters are illustrated in Figure 39 and Figure 40, showing the impact of changing material thickness on the Bragg-peak and the ^{11}C and ^{15}O particle productions. In Table 8 and Table 9, the R_{50} of the Bragg-peaks and the range of the R_{50} distance of positron emitters for both phantom designs can be seen, which were evaluated with an approximation of a second order polynomial function. Figure 41 visualizes the increasing depth of the R_{50} values, with decreasing bone thickness, of the positron emitters and the deposited dose, which is listed in Table 8.

Figure 37: β⁺-activity distribution with different bone slice thickness, stored with CSP actor for ¹¹C activity distribution (Top) and for ¹⁵O (Bottom). The phantom design from Figure 24 was simulated.

Figure 38: Activity distribution with different bone slices stored with PAS actor for ^{11}C activity distribution (Top) and for ^{15}O (Bottom). The phantom design from Figure 24 was simulated.

Figure 39: Activity distribution with different air slices stored with CSP actor for ^{11}C activity distribution (Top) and for ^{15}O (Bottom). The phantom design from Figure 25 was simulated.
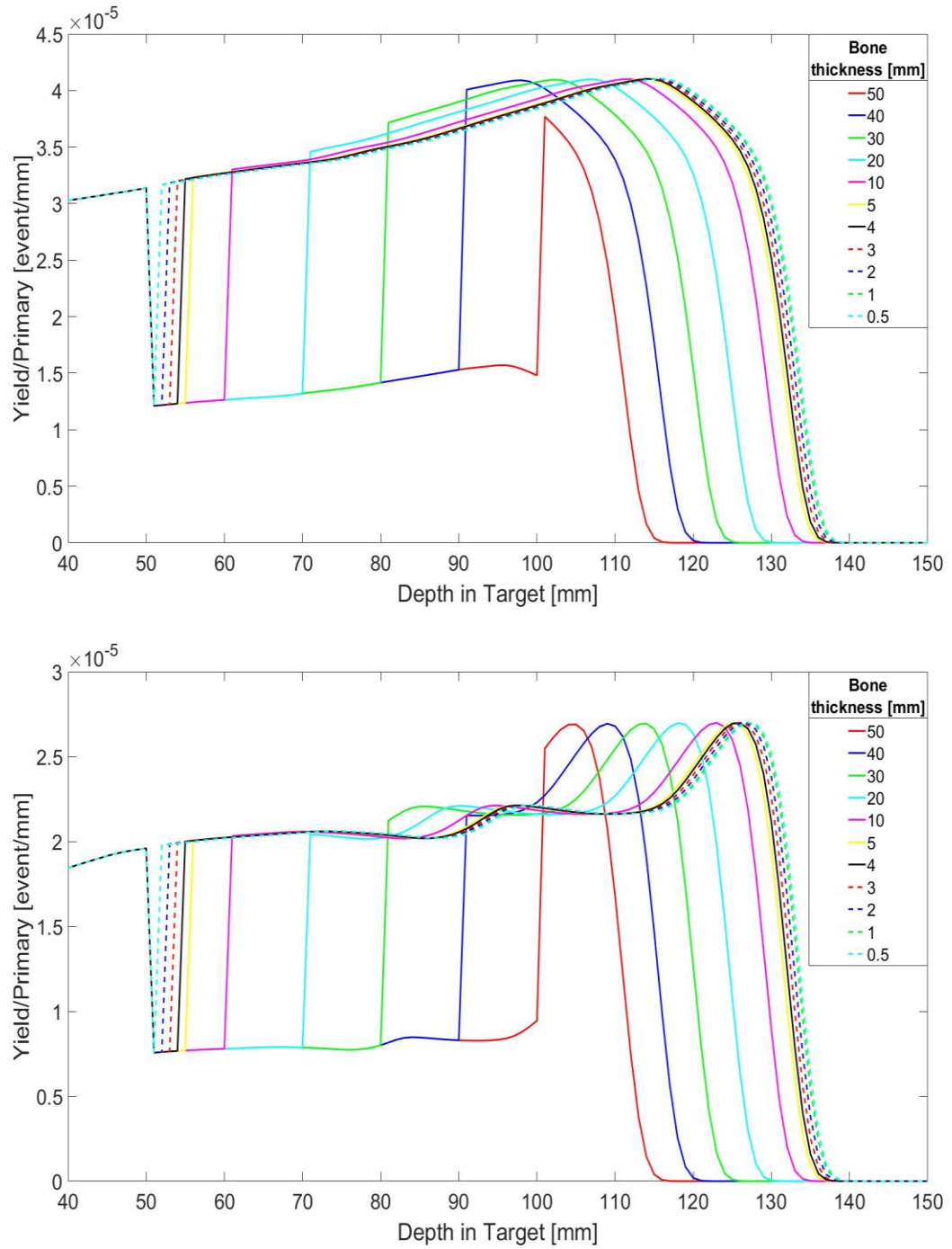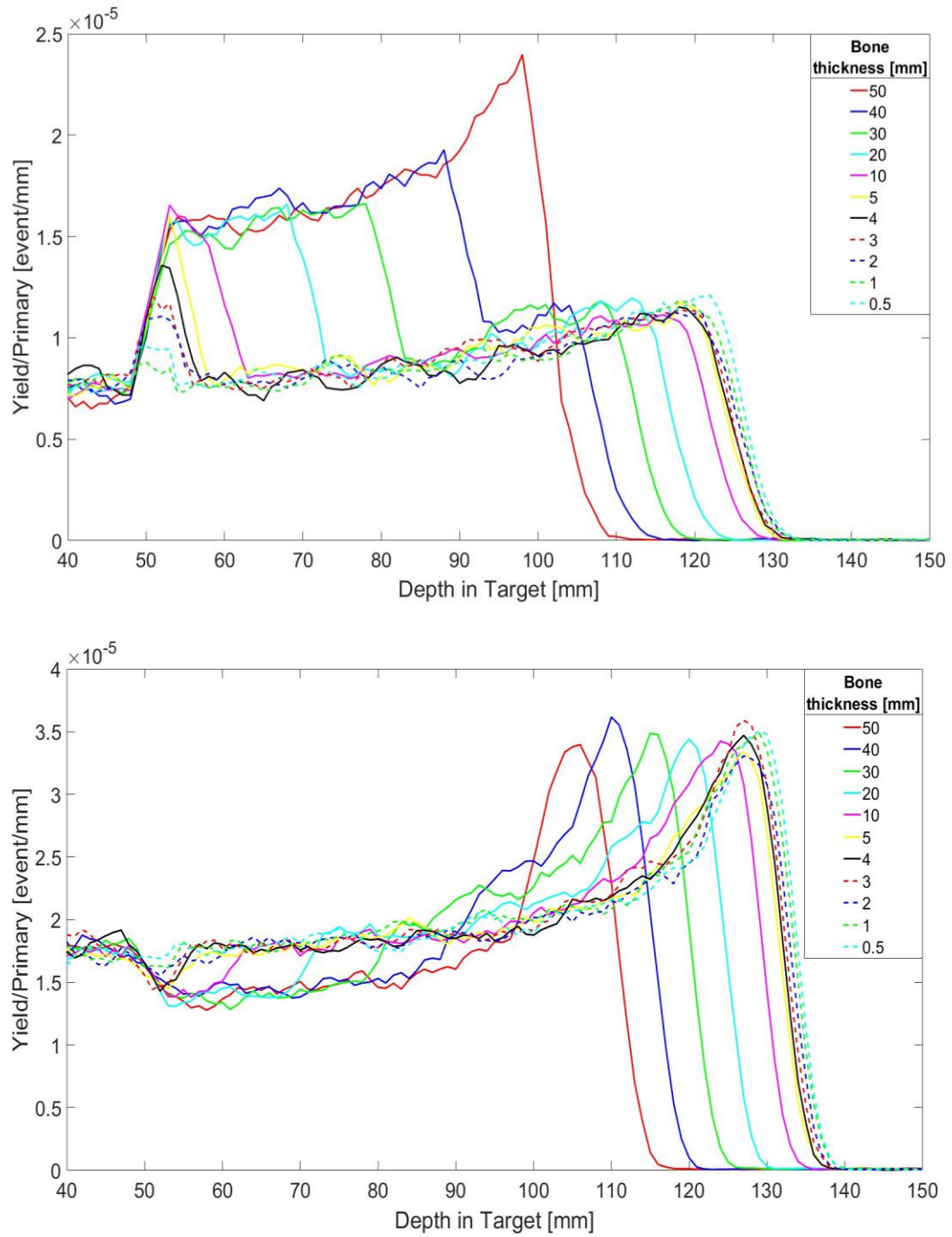
Figure 40: Activity distribution with different air slices stored with PAS actor for ^{11}C activity distribution (Top) and for ^{15}O (Bottom). The phantom design from Figure 25 was simulated.
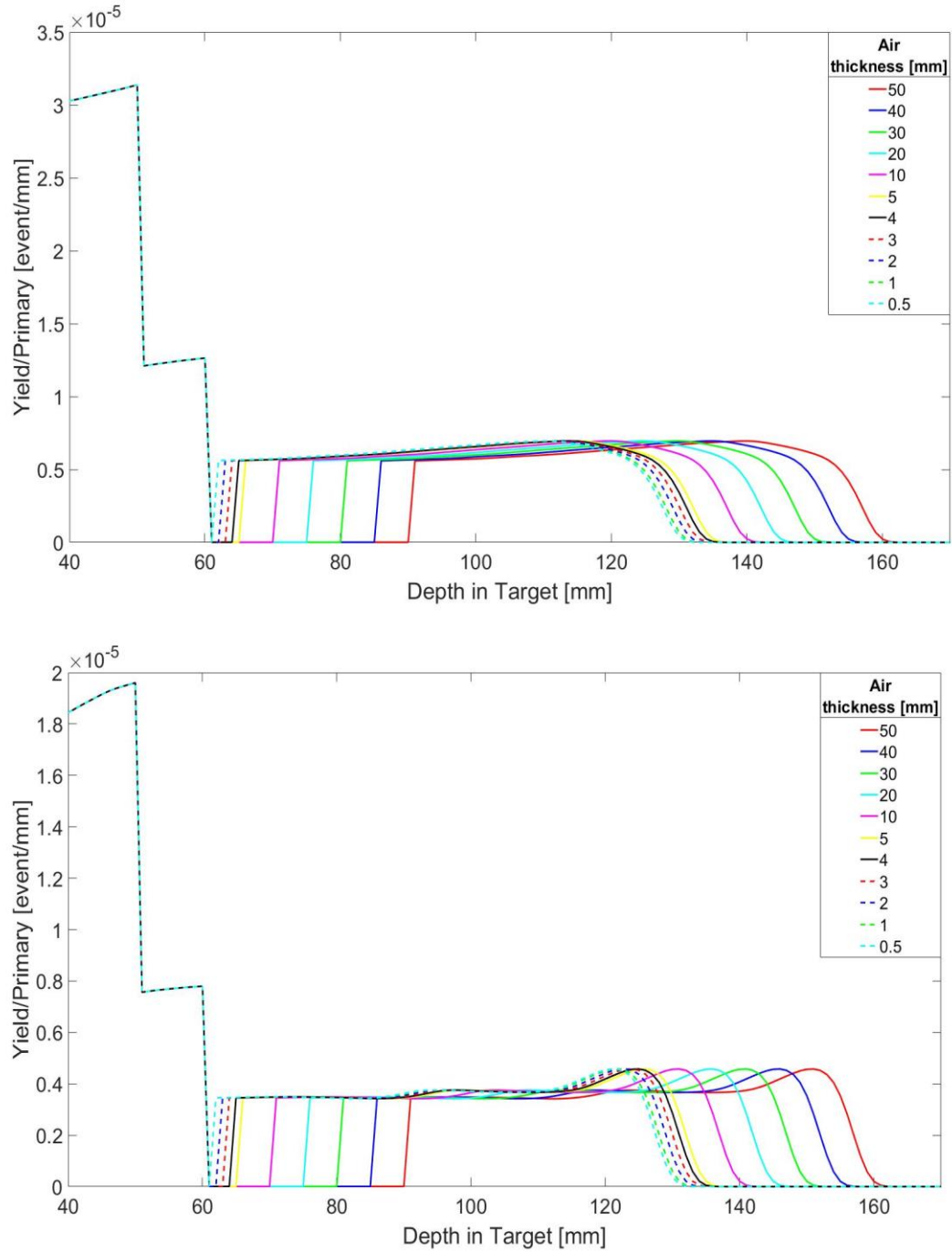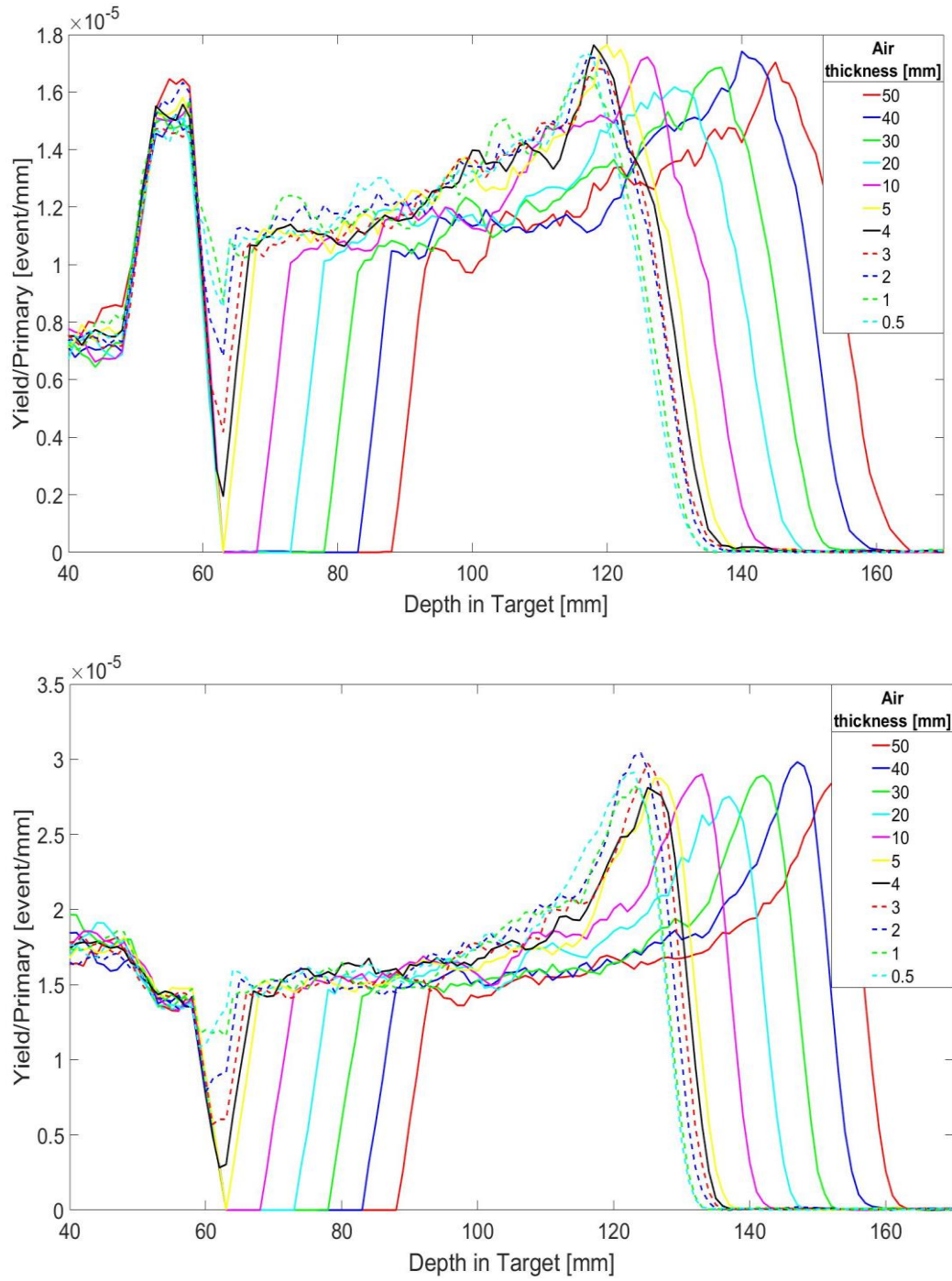
Bone thickness [mm]	R_{50} ^{11}C CSP [mm]	R_{50} ^{15}O CSP [mm]	R_{50} ^{11}C PAS [mm]	R_{50} ^{15}O PAS [mm]	Dose R_{50} [mm]
40	113.30	114.47	107.15	114.78	120.76
30	117.87	119.04	116.01	119.38	125.34
20	122.47	123.63	117.55	123.98	129.92
10	127.06	128.24	120.63	128.64	134.53
5	129.37	130.54	123.25	130.89	136.83
4	129.83	131.01	123.19	131.41	137.29
3	130.30	131.47	124.07	131.88	137.76
2	130.75	131.93	124.65	132.34	138.22
1	131.22	132.39	125.02	132.77	138.68
0.5	131.44	132.62	125.40	133.06	138.90

Table 8: Depth of the R_{50} distance of the β^{+}-activity for ^{11}C and ^{15}O, and the R_{50} value of the Bragg-peak, for a water phantom consisting of varying bone insert thickness.

Air slice [mm]	R_{50} ^{11}C CSP [mm]	R_{50} ^{15}O CSP [mm]	R_{50} ^{11}C PAS [mm]	R_{50} ^{15}O PAS [mm]	Dose R_{50} [mm]
30	155.30	156.10	154.36	156.23	161.95
25	150.30	151.10	149.48	151.21	156.95
20	145.30	146.10	144.28	146.29	151.96
15	140.30	141.10	139.85	141.17	146.95
10	135.30	136.10	134.49	136.19	141.96
5	130.30	131.10	129.70	131.31	136.97
4	129.30	130.10	128.61	130.28	135.97
3	128.30	129.10	127.85	129.17	134.96
2	127.30	128.10	126.55	128.24	133.97
1	126.30	127.10	125.43	127.29	132.96
0.5	125.80	126.60	124.97	126.73	132.47

Table 9: Depth of the R_{50} distance of the β^{+}-activity for ^{11}C and ^{15}O, and the R_{50} value of the Bragg-peak, for a water phantom consisting of varying air insert thickness.
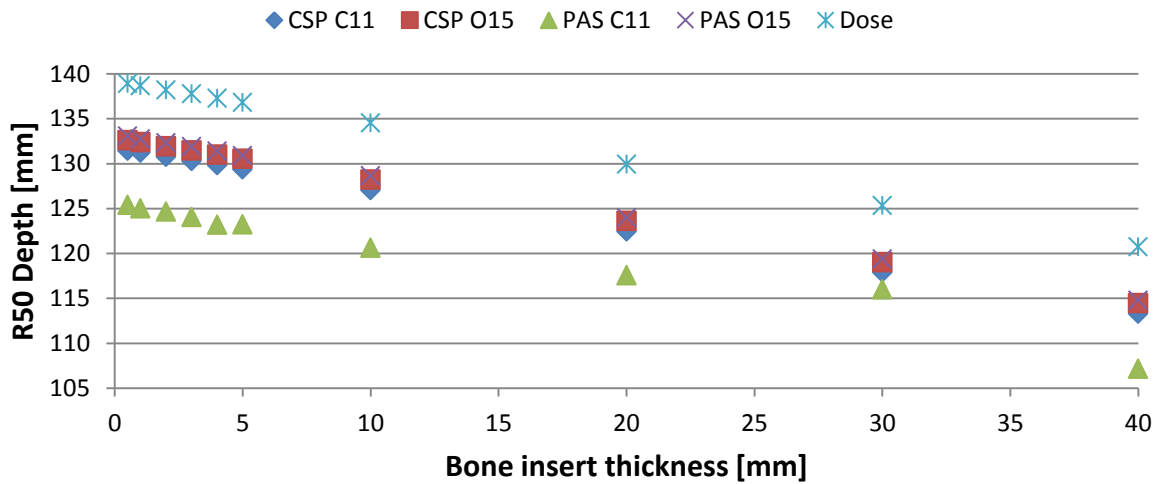
Figure 41: Range of the distal R_{50} of produced positron emitters and distal R_{50} dose for different bone inserts with varying thickness.
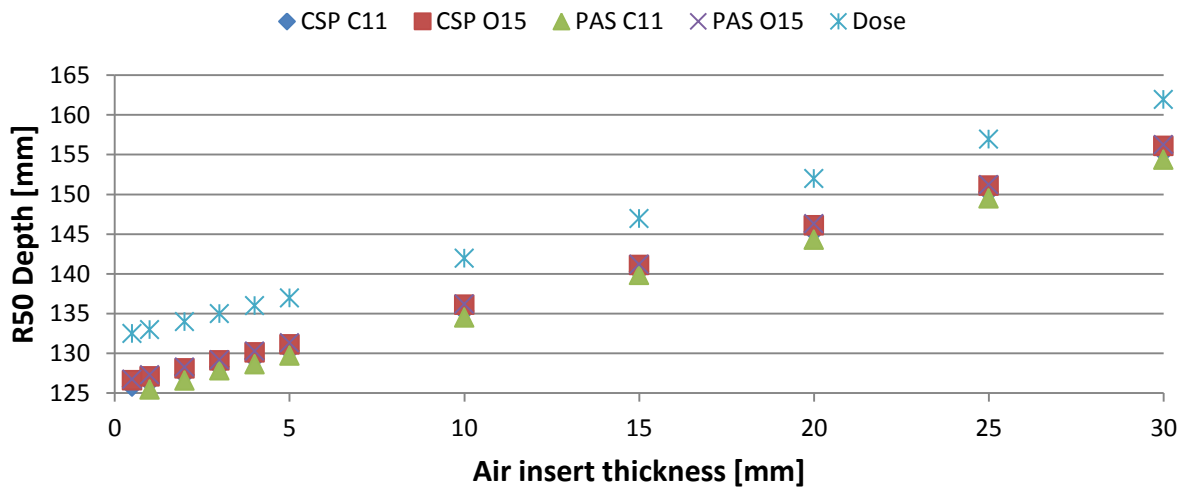

Figure 42: Range of the distal R_{50} of produced positron emitters and distal R_{50} dose for different air inserts with varying thickness.

4.3.2.1 PHANTOMS WITH BONE INSERTS OF VARYING THICKNESS DISCUSSION

Comparing the activity distributions obtained with the CSP and PAS actor from Figure 37 and Figure 38, varieties can be observed.

As already assumed, the most distinct observation was that the R_{50} values of produced positron emitters shifts to greater depths with decreasing bone thicknesses for all simulation setups. Note that the R_{50} values in the following discussions was referred to the location, distal the material inserts.

The shifting was caused by the fact that the primary particle numbers were reduced via fragmentation collisions with the bone inserts. Thus the range of the R_{50} values of produced β^+ particles decreased, depending on the material and thickness. As in the previous chapter described the PAS showed higher oscillations than the CSP actor.

Another observation was the different activity for the CSP and PAS actor, before and after the bone inserts. Evidently for the CSP actor the number of produced β^+ emitters decreased in every simulation setup in the location of the bone inserts and increased again after penetration of those. Whereas for the CSP actor, the number of produced ^{11}C particles increased in that volume and decreased afterwards. For the ^{15}O production, the numbers decreased only slightly compared to the material before the inserts. However, in distal direction the production of ^{15}O particles increased again, which created the characteristic PAS actor peak at the end of the range.

Those differences between the actors can only be explained as stated in the previous sub-chapter, namely differently used crossections.

As expected, not only the activities, but also the range of the deposited dose by the proton beam were affected by different bone inserts. In Figure 41 the shifting Bragg-peak and the range of the R_{50} values of produced β^+-emitters is illustrated. It shows a linear increment of the R_{50} distance for the produced positron emitter distributions and the deposited dose, with decreasing bone thickness. The results for the ^{11}C PAS actor showed at some points small deviations caused by the high oscillation of positron emitters at the distal region. Thus the evaluation of the results by an approximation with a second order polynomial function was difficult.

It can be stated that with each mm of bone inserts, the ranges of the values will change for approximately 0.5 mm. Furthermore, the linearity has proven that the behaviour of the proton beam is similar to commercial treatment planning systems and is assumed to be correct in this context.

4.3.2.2 PHANTOMS WITH AIR INSERTS OF VARYING THICKNESS DISCUSSION

The range of the R_{50} values of produced positron emitters and the R_{50}, influenced by different production actors were observed in Figure 39 and Figure 40. The effect of different used crossections for both actors can distinctively be observed in the distal region at the end of the range for all simulation setups. Comparing the results with those from Figure 35, the PAS actor exhibits the typical peak at the end of the range unlike the CSP actor.

The activity distributions from other publications (e.g. K.Parodi et.al. [6] or M. Studenski et. al. [93]) in brain tissue revealed an increment at the end of the range of the beam. Comparing the results from Figure 39 and Figure 40, which show the activity production in a homogenous phantom with brain tissue at the distal end of the phantom, the *ProductionAndStopping* actor showed a more conformal behaviour over the *CrossSectionProduction* actor. This behaviour of the actors results from the fact that both actors handle interaction processes differently. The *ProductionAndStopping* actor is completely MC based, whereas the *CrossSectionProduction* actor on the other hand is only partially MC based. The *CrossSectionProduction* actor uses the flux of the particles calculated by MC, in combination with the cross-section data from experimental results [85].

Both actors showed no productions of positron emitters in the air slices, which was reported by other publications as well. In some cases the cavity is replaced with HU values of e.g. 40, to simulate a filled cavity [6] [94]. PET measurements show clearly the existences of positron emitters in air cavities, which results in discrepancies compared to the activity simulations with MC and have to be taken into consideration.

As expected from the results in the previous sub-chapters, the R_{50} distance of the produced β^+ particles and the R_{50} of the dose shifted with changing air thickness. But in

this case, the ranges decreased with decreasing air insert thickness. This is caused by the fact that in air no ^{11}C or ^{15}O particles were created and therefore, the proton beam does not suffer any loses via fragmentation.

In Figure 42, a linear decrease of the range of the R_{50} values of positron emitters and the R_{50} of the deposited dose, with changing air slice thickness is illustrated.

It can be stated that with each mm of air the range of the R_{50} value for positron emitters and deposited dose, will decrease for approximately 1 mm.

In the end, the most important question was which range differences can be observed. For the *CrossSectionProduction* actor the R_{50} values of produced positron emitters can be evaluated discretionary, without limitation of insert thickness (see Figure 37 and Figure 39). Whereas for the *ProductionAndStopping* actor, the range differences of the R_{50} values of β^{+}–particles is limited to approximately less than 1mm (see Figure 38 and Figure 40). Note that in Table 8 and Table 9 the results were evaluated with a 2nd order polynomial approach, which is why precise values were available. However, it is important for a clinical system to provide range differences of 1–2mm, as well as an adequate number of primary particles [91]. The results in this chapter, which were less than 1mm and a particle count of 10^{7}, a good compliance with those from other publications and works were achieved, which were in the range of 2–4mm [1] [95] [96] [97] [98]. This leads to a favouring of the *CrossSectionProduction* actor over the *ProductionAndStopping* actor, in terms of range differentiation.

4.4 HOUNSFIELD UNIT SCALE SIMULATIONS

In this sub-chapter the influence of HU scales (see Table 3) on the range uncertainty of the distal R_{80}, R_{50}, such as the lateral R_{50} dose values are displayed. The resulting data was evaluated approximately at the centre of the beam in cranial/caudal direction for the distal values (Figure 43 red line). In the same slice the lateral values were evaluated, which is indicated in Figure 43 as the yellow line. The MC simulated dose profiles were compared with the calculated dose profiles from Raystaion.
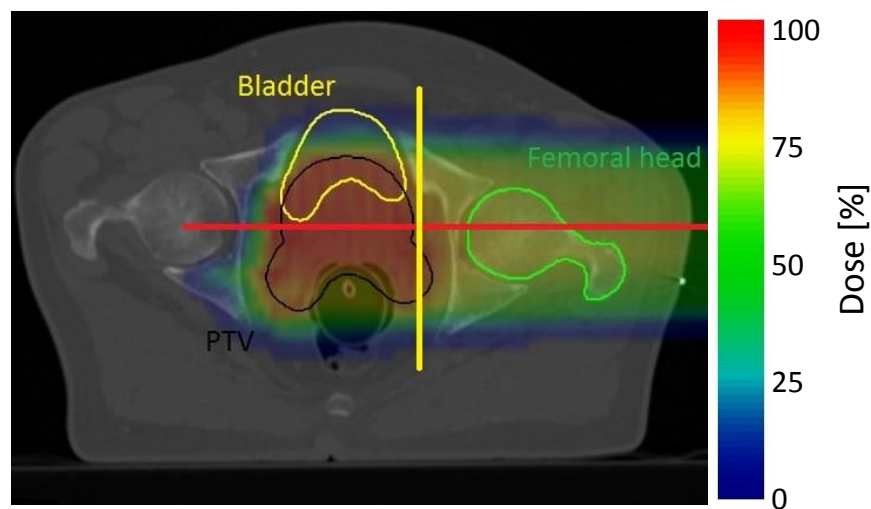

Figure 43: MC calculated dose deposition with 1×10^{8} protons. The red line indicates the evaluated slice for distal depth dose depositions and yellow for the lateral. The dose of the beam is displayed in rainbow colours and is normalized to the maximum. Blue stands for the minimum and red for the maximum dose.

The lateral dose profiles for the HU scale from GATE and Raystation can be seen in Figure 44. In Figure 45 the same setup but in distal direction of the beam is visualized. The simulations were carried out with 10^8 primary particles, a step size of 0.1 mm and the data was stored with the *CrossSectionProduction* actor. The simulation results were compared to the lateral dose profiles from the calculated TP. Evaluated distal R_{80}, R_{50} and the length R_{80}-R_{20}, as well as lateral R_{50} values for the calculated TP and MC simulations are listed in Table 10. The values were measured with a 2nd order polynomial approximation.

Figure 44:Lateral dose profiles of the calculated TP (blue line) and MC simulations with different HU scales (red dashed GATE HU scale, green dotted Raystation HU scale). Values were normalized to 1 for display purposes.
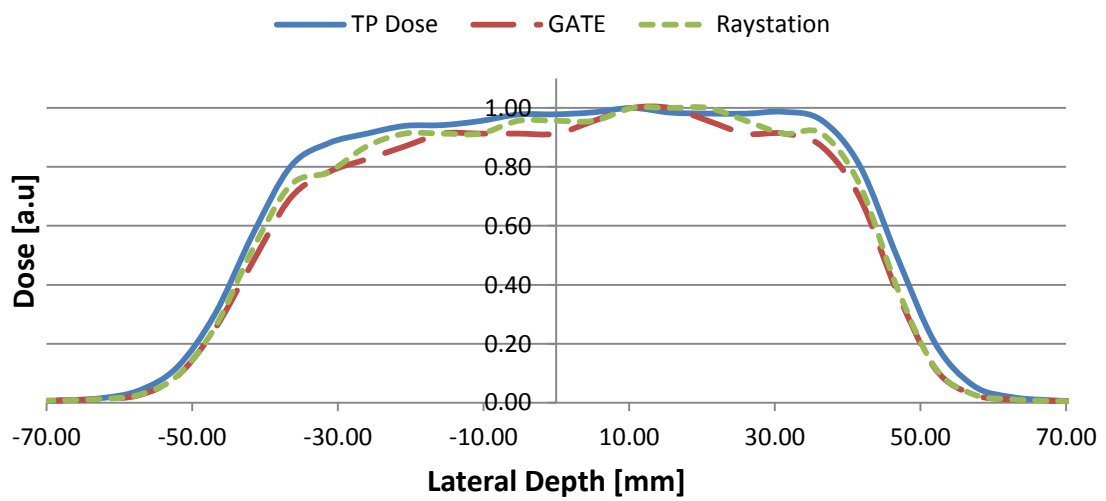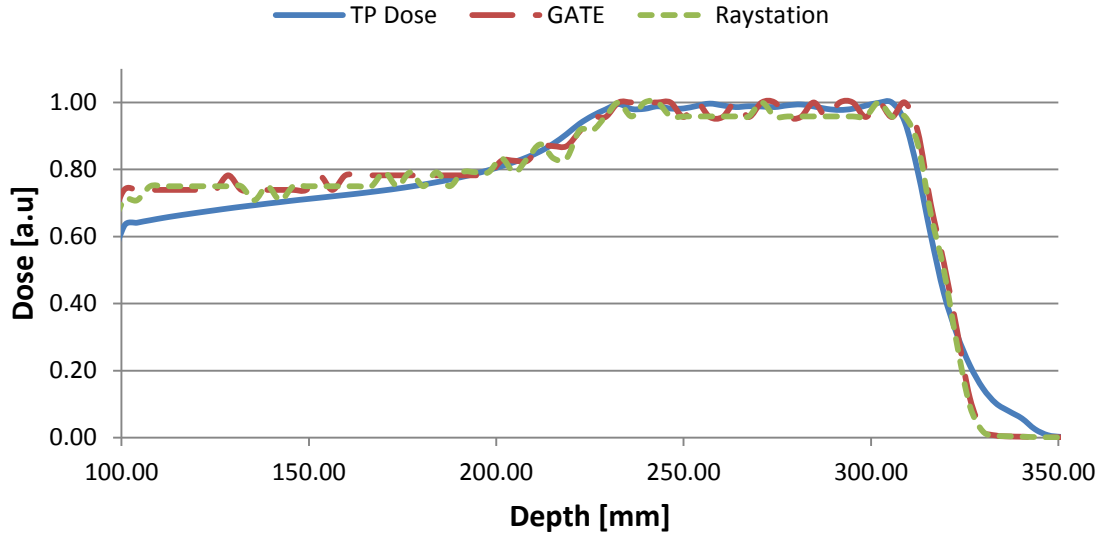
Figure 45: Distal dose profiles of the calculated TP (blue line) and MC simulations with different HU scales (red dashed GATE HU scale, green dotted Raystation HU scale). Values were normalized to 1 for display purposes.

	Distal R_{80} [mm]	Distal R_{50} [mm]	Lateral R_{50} [mm]
TP	315.95	320.95	51.63 ± 1.79
GATE	317.74	323.78	49.78 ± 1.26
RAY	317.23	323.08	50.32 ± 1.58

Table 10: Values of the distal R_{80}, R_{50} and lateral R_{50} of the calculated TP dose and MC simulations with different HU scales.

4.4.1.1 DISCUSSION

The influence of two different HU scales, namely the default GATE HU scale and the HU scale applied in the TP station Raystation (see Table 3), on the distal R_{50}, R_{80} and on the lateral R_{50} values was explored. The values were analysed and compared to the dose depositions from the TP at the same positions.

The expectation of the influence of the two different HU scales was assumed to be minimal in terms of range differences and dose depositions. In Figure 44, only small fluctuations compared to the TP dose profile were observed. This is mainly caused by the *CrossSectionProduction* actor, which was already explained in chapter 4.3.1. The biggest impact was measured for the range of the R_{50} value. For the Raystation HU scale a deviation of 1.3 mm and for the GATE HU scale a deviation of 1.85 mm was measured (see Table 10).

The distal dose profiles from Figure 45 revealed nearly the same behaviour for both HU scales, throughout the whole range. Both simulation setups showed a deviation at the entrance region and at the end of the dose fall-off compared to the TP dose profile, which is probably caused by the *CrossSectionProduction* actor. The range uncertainties in distal direction from Table 10 showed the same influence of the HU scales as for the lateral profiles. Both ranges revealed a higher uncertainty for the GATE HU scale. The R_{80} value deviated 1.79 mm for GATE HU scale and 1.28 mm for the Raystation HU scale from the TP. For the range differences of the R_{50} value the Raystation HU scale was once again lower, namely 2.13 mm and the GATE HU scale deviated 2.83 mm from TP.

Nevertheless, scientific publications from Parodi et.al. and Knopf et.al., revealed deviations of approximately 1 – 3 mm which means that both HU scales would be acceptable [3] [4] [5] [6]. However, in both beam profiles the HU scale from Raystation showed a smaller deviation of approximately 0.5 mm.

In the end it can be stated that HU scales have a minor impact on the overall distribution of the dose depositions. However in terms of range uncertainties, HU scales with higher segmentation of the different levels leads to a more precise measurement.

4.5 SINGLE FIELD TP SIMULATION

This sub-chapter shows the resulting dose and activity distributions with the final simulation parameters, measured and observed in the previous chapters. The TP dose distribution is compared to the MC simulation and the resulting β^+ – emitter distributions.

The simulations were performed with the QGSP_BIC_HP_EMZ physics list resulting from the chapter 4.1.1. From the statistical analysis in chapter 4.2.1, primary particle numbers of 10^8 and a step size of 0.1 mm was applied. For the storage of the produced particles, the *CrossSectionProduction* actor originating from the chapter 4.3.2.1 and 4.3.2.2 was applied. The final parameter analysed in chapter 4.4.1.1 was the HU scale from the planning station Raystation.

In the following figures the contours of the PTV, which is the prostate, is indicated with a black line.

Figure 46 top shows the deposited dose from the TP system Raystation in cranial/caudal direction of the patient. In comparison, the same dose deposition from the MC simulation is shown in Figure 46 bottom. The produced positron emitter distribution with C^{11} and O^{15} from the MC simulations is shown in Figure 47.
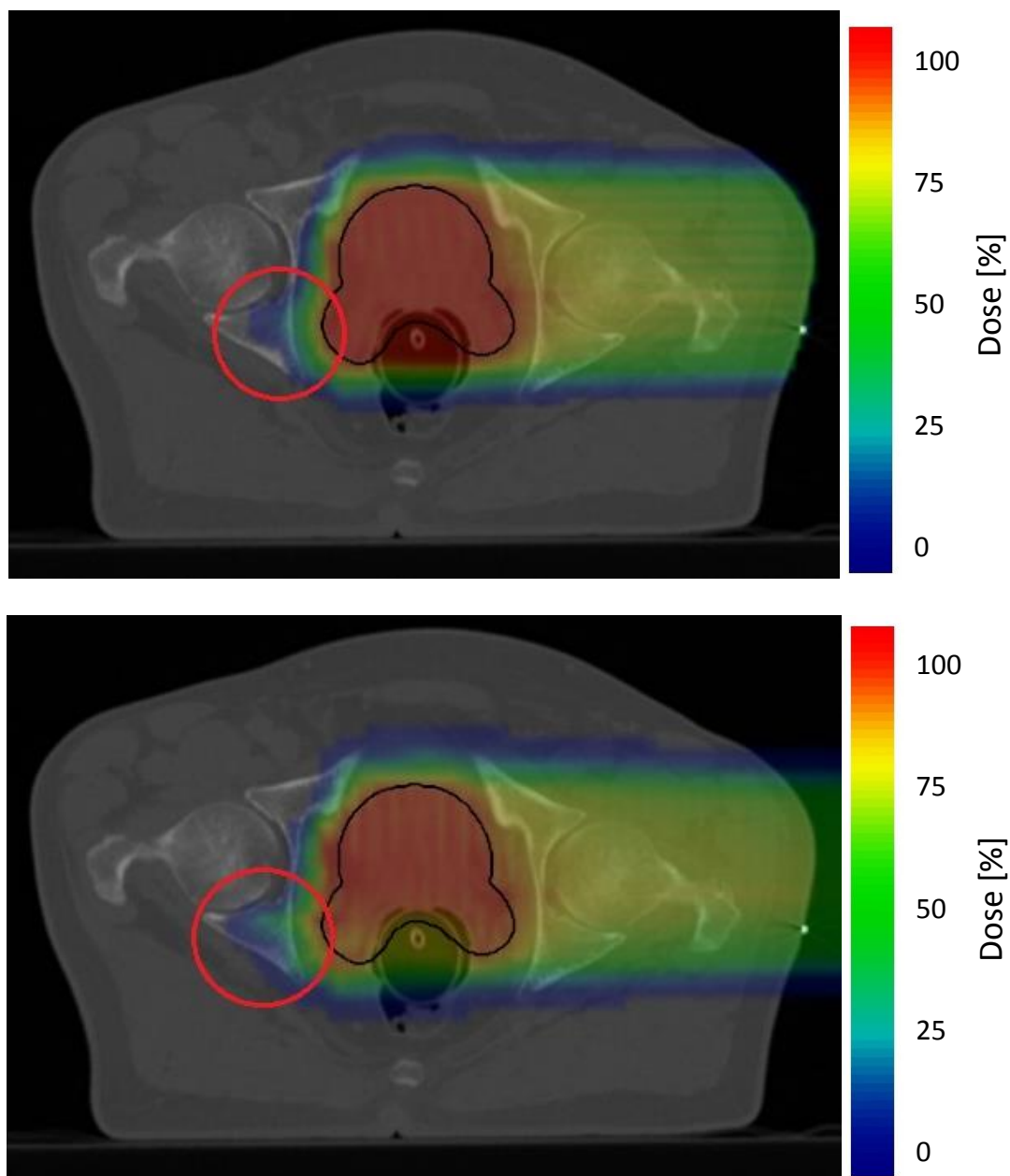
Figure 46: Calculated TP (top) and MC simulated dose distribution (bottom). The red cycle indicates changes in the depth of the dose deposition, caused by the export of the DICOM files with RayStation. The dose of the beam is displayed in rainbow colours and is normalized to the maximum. Blue stands for the minimum and red for the maximum dose.

Figure 47: C^{11} activity distribution (top) and O^{15} (bottom). The quantity of produced particles is displayed in rainbow colours and is normalized to the maximum. Blue stands for the minimum and red for the maximum amount of positron emitters.

4.5.1 Discussion

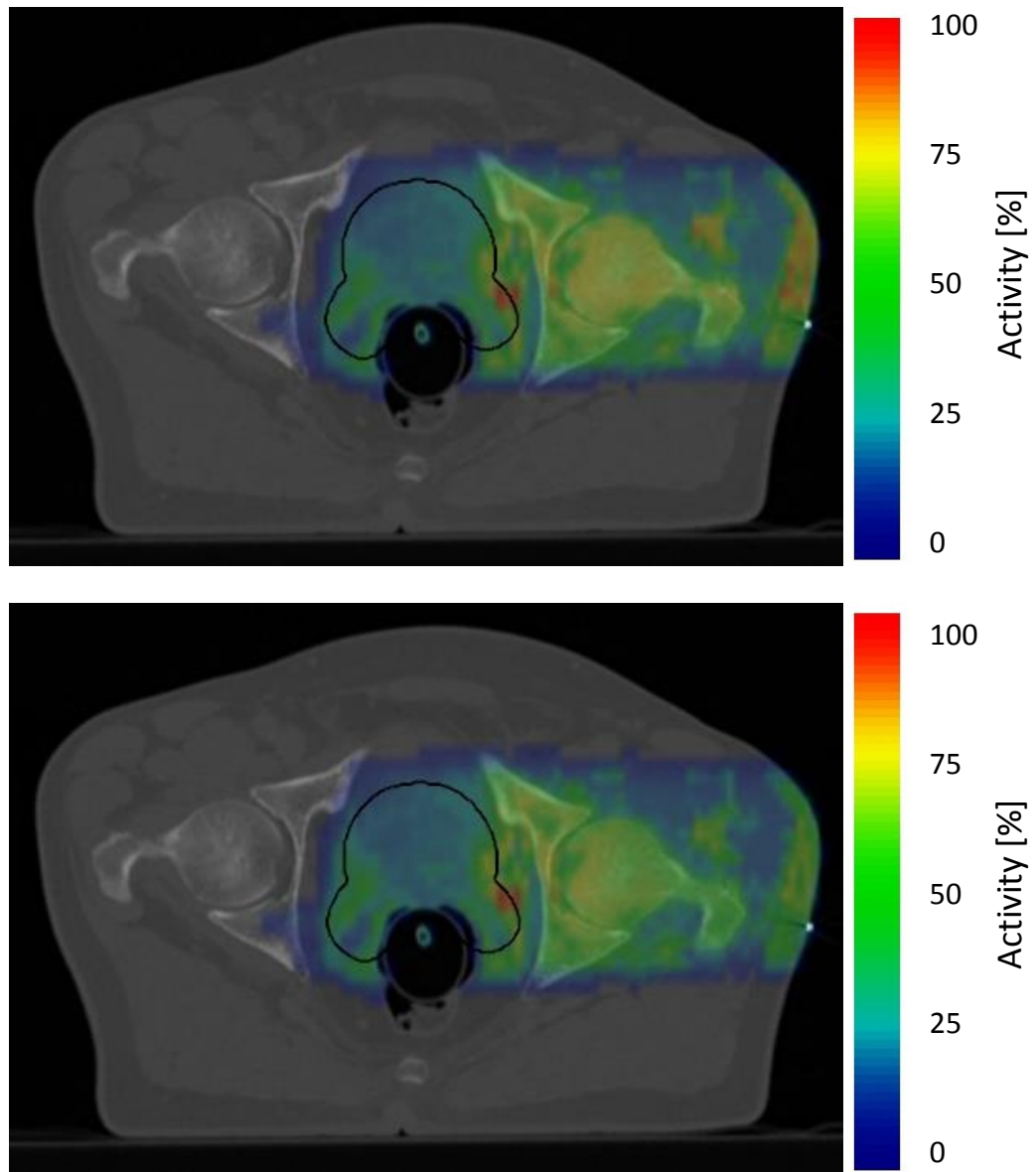The expectation of a fully functioning and precise MC simulation of a calculated TP was achieved. Comparing the dose distributions in Figure 46, on the first view very similar dose depositions can be observed. The only noticeable mismatch can be found in the fall-off region past the anal cavity, which is indicated with a red cycle. It shows a dose deposition at greater depths because of the fact that the anal cavity is filled with water in the calculation of the TP, but is applied with air in the MC simulations. This is probably caused by the export of the DICOM files with RayStation.

The behaviour at the same position can be seen in Figure 47 for the produced positron emitter distribution as well.

Compared to other publications (e.g. Parodi et.al. [6] and Knopf et.al. [3]), the positron emitter distributions from Figure 47 exhibit similar results. One of them is the lack of positron emitters in air filled regions, which is in this case the anal cavity. Normally positron emitters are produced in air cavities, which have to be taken into consideration for MC simulations. In some cases the cavity is replaced with HU values of e.g. 40, to simulate a filled cavity [6] [94].

Another expected similarity is the accumulated production of positron emitters in the entrance region, high density regions and in the volume of the PTV. This counts for the C^{11} and the O^{15} positron emitter distributions.

In the end it can be stated that the MC simulations of the dose and positron emitter distributions achieved good results with the calculated dose in Raystation, as well as with results from the literature.

6   CONCLUSION AND OUTLOOK

This work proves that the Monte Carlo framework GATE is capable of performing efficient verification simulations of β^+-activity distributions for beam applications in PT. The validation of the uncertainties in distal and lateral profiles of a proton beam, in terms of depth doses and produced β^+-activity profiles, were compared and evaluated for a treatment plan. The plan was created and the data was exchanged with the commercial treatment planning system (RayStation). The plan used a single-field proton beam irradiating the prostate.

Due to the large number of available physics lists in GATE, the best list for positron distributions caused by proton irradiations in clinical energy ranges was determinated using experimental data by K. Parodi [2]. This led to the conclusion that physics lists with the Binary Cascade model (BIC) and the additional Quark Gluon String model (QGS), more precisely the QGSP_BIC_HP physics list, showed good accordance to the experimental data [99]. A deviation of 1.8 % for 110 MeV to 17.8 % for 175 MeV and for ^{15}O from 11.3 % for 110 MeV to 16.3 % for 175 MeV was measured.

As expected, the statistical analysis showed a reduction of the uncertainty with increasing primary particle numbers. The uncertainty with 0.1 mm step size reduced from ~7% with 10^5 primary particles to ~2.3% with 10^6 primary particles. Similar but slightly higher results were achieved with 0.01 mm step size. Furthermore, with higher numbers of protons per beam, further reduction of the uncertainty could be achieved. With 10^8 primary particles a statistical uncertainty below 2% was achieved, which was demonstrated with the distinct reduction of the fluctuations of produced positron emitters.

The analysis of the data storage actors, *ProductionAndStopping* and *CrossSectionProduction*, related to the dose and β^+-activity distributions of homogenous phantoms with different bone and air inserts consisting of varying thickness, lead to several conclusions. Besides the higher fluctuation of the *ProductionAndStopping* actor, the *CrossSectionProduction* actor did not show a characteristic peak at the maximum of produced positron emitters. Nevertheless, both actors showed a shifting of the depth of R_{50} values for produced ^{11}C and ^{15}O, which was influenced by different material insert thicknesses. In terms of range uncertainty, the *ProductionAndStopping* actor revealed an

uncertainty of less than 1 mm, whereas the *CrossSectionProduction* actor was able to visualize uncertainties for any insert thicknesses. According to other theses and publications, which revealed an uncertainty of 2–4mm, the results in this thesis were in a similar range [1] [95] [96] [97] [98]. Another observation was that the produced ^{10}C particles were not sufficient enough to precisely evaluate the data. It was already assumed that ^{10}C would be impractical as verification parameter for PT–PET, due to the fact that in other publications ^{11}C and ^{15}O was mainly used in this context [5] [92] [100]. The more accurate behaviour in the target region resulted in a decision for the *CrossSectionProduction* actor.

The comparison of the HU scales with different calibrations lead to the conclusion that lower deviations can be expected, with smaller subdivisions. The deviation for the R_{80} and R_{50} values compared to the TP was below 3 mm, which is comparably to the literature [3] [4] [5] [6].

A reduction of the range uncertainties can probably be expected with a more detailed HU scale.

The by hand compared dose and activity distribution with the final simulation parameters revealed good accordance with the calculated TP and the literature. The TP simulation with a single field irradiation of a prostate was performed with 10^8 primary particles, 0.1 mm step size, HU scale from the TPS Raystation and the data was stored with the *CrossSectionProduction* actor. The main discrepancy was a missing of positron emitters in air filled cavities. This problem leads to a shifting of the deposited dose to greater depths, thus it has to be taken into consideration.

Further development and evaluation of the simulation parameters needs to be performed to increase the precision of range uncertainties for dose and β^+-activity distributions. Thus, the statistical uncertainty can be reduced as well. A more detailed analysis of the storage actors would help to improve evaluations for a higher efficiency of the simulations. The last major aspect, which should be focused on are the relativley long simulation times.

Bibliography

[1]. **X. Zhu, et. al.** *Proton Therapy Verification with PET Imaging.* s.l. : Ivysoring International Publisher, 2013. 731-740.

[2]. **K., Parodi.** *On the feasibility of dose quantification with in-beam PET data in radioterapy with 12C and proton beams.* s.l. : Ph.D. Dissertation, Technische Universität Dresden, 2004.

[3]. **A. Knopf, K. Parodi, T. Bortfeld, H. A. Shih, H. Paganetti.** *Systematic analysis of biological and physical limitations of proton beam range verification with offline PET/CT scans.* s.l. : Physics in Medicine and Biology, 2009. 54: 4477-4495.

[4]. **A. Knopf, et. al.** *Quantitative assessment of the physical potential of proton beam range verification with PET/CT.* s.l. : Physics in Medicine and Biology, 2008. 4137–4151.

[5]. **K. Parodi, et.al.** *Clinical CT-based calculations of dose and positron emitter distributions in proton therapy using the FLUKA Monte Carlo code.* s.l. : Physics in Medicine and Biology, 2007. 3369–3387.

[6]. **K. Parodi, et al.** *Patient study of in vivo verification of beam delivery and range, using positron emission tomography and computed tomography after proton therapy.* s.l. : Int J Radiat Oncol Biol Phys, 2007. 68(3): 920–934..

[7]. **A. Mesbahi, et. al.** *Monte Carlo calculation of Varian 2300C/D Linac photon beam characteristics: a comparison between MCNP4C, GEANT3 and measurements.* s.l. : Applied Radiation and Isotopes, 2005. 62:469-477.

[8]. **G. A. Pablo Cirrone, et. al.** *Implementation of a New Monte Carlo—GEANT4 Simulation Tool for the Development of a Proton Therapy Beam Line and Verification of the Related Dose Distributions.* s.l. : IEEE, 2005. 52: 0018-9499.

[9]. **J. Sempau, et. al.** *Monte Carlo simulation of electron beams from an accelerator head using PENELOPE.* s.l. : Physics in Medicine and Biology, 2001. 46:1163-1186.

[10]. **C. Robert, et. al.** *Distributions of secondary particles in proton and carbon-ion therapy: a comparison between GATE/Geant4 and FLUKA Monte Carlo codes.* s.l. : Physics in Medicine and Biology, 2013. 58:2879-2899.

[11]. **H. Paganetti, et. al.** *Clinical implementation of full Monte Carlo dose calculation in proton beam therapy.* s.l. : Physics in Medicine and Biology, 2008. 53:4825-4853.

[12]. **K. Assie, et. al.** *Monte Carlo simulation in PET and SPECT instrumentation using GATE.* s.l. : Nuclear Instruments and Methods in Physics Research, 2004. 527:180-189.

[13]. **Chang, A.E., Ganz, P.A., Hayes, D.F., Kinsella, T., Pass, H.I., Schiller, J.H., Stone, R.M., Strecher, V.** *Oncology An Evidence-Based Approach.* s.l. : Springer, 2006.

[14]. **Röntgen, Willhelm Conrad.** *Über eine neue Art von Strahlen.* 1896.

[15]. **Leopold, F.** *Ein mit Röntgen-Strahlen behandelter Fall von Neavus pigmentosus piliferus.* s.l. : Wiener Medizinische Wochenschrift, 1897.

[16]. **Wilson, Robert Rathbun.** *Radiological use of fast protons Radiology.* 1946.

[17]. **Lawrance J. H., Tobias C. A., Linfoot J. A., Born J. L., Chong C. Y.** *Heavy-particle therapy in acromegaly and Cushing's disease.* s.l. : JAMA, 1976. 2307-11.

[18]. *Particle Therapy Co-Operative Group.* [Online] [Cited: 16 01 2016.] http://www.ptcog.ch/index.php/facilities-in-operation.

[19]. **Krieger, Hanno.** *Grundlagen der Strahlungsphysik und des Strahlenschutzes.* s.l. : Tuebner Verlag, 2007.

[20]. **Gagnon, Pauline.** Quantumdiaries.org. [Online] [Cited: 08 01 2016.] http://www.quantumdiaries.org/2012/02/15/the-hidden-face-of-cern/.

[21]. **Kuess, P.** *Automated analysis of PET based in-vivo monitoring in ion beam therapy.* s.l. : Phd. Thesis, Department of Radiation Oncology, 2014.

[22]. **W. Schlegel, T. Bortfeld, A.-L.Grosu.** *New Technologies in Radiation Oncology.* s.l. : Springer Verlag, 2006. 3-540-00321-5.

[23]. **ICRU.** *ICRU Report 50: Prescribing, Recording and Reporting Photon Beam Therapy.* s.l. : Journal of ICRU, 1993.

[24]. —. *ICRU Report 62: Prescribing, Recording and Reporting Phton Beam Therapy (Supplement to ICRU Report 50).* s.l. : Journal of ICRU, 1999.

[25]. **Mitja, M.** Treatment Head of a Linac. [Online] [Cited: 31 10 2016.] http://ojs.ujf.cas.cz/~mitja/presentations/AV04/slike/posp_glava.png.

[26]. **Tatiana Wenzl, Jan J Wilkens.** *Modelling of the oxygen enhancement ratio for ion beam radiation therapy.* s.l. : IOP Publishing, 2011. 56: 3251-3268.

[27]. **Harald Paganetti, et. al.** *Relative Biological Effectiveness (RBE) values for proton beam therapy.* s.l. : Elsevier, 2002. S0360-3016(02)02754-2.

[28]. **Marco Durante, Jay S. Loeffler.** *Charged particles in radiation oncology.* s.l. : J. S. Nat. Rev. Clin. Oncol., 2010. 7: 37-43.

[29]. **Milby, Abigail Berman.** OncoLink. [Online] 21 5 2012. [Cited: 23 10 2017.] https://www.oncolink.org/conferences/coverage/ptcog/oncolink-at-ptcog-2012/reporting-from-ptcog-2012/carbon-vs.-proton-for-innovative-applications-of-particle-beam-therapy.

[30]. **Herman Suit, et. al.** *Proton vs carbon ion beams in the definitive radiation treatment of cancer patients.* 2010. 95:3-22.

[31]. **Jay Reiff, Reiner Class Stephan Mose.** *Encyclopedia of Radiation.* s.l. : Springer, 2013.

[32]. **Eric J. Hall, et. al.** *Intensity-modulated radiation therapy, protons, and the risk of second cancers.* s.l. : Int. J. Radiation Oncology Biol. Phys, 2006. 0360-3016.

[33]. **A. J. Lomax, et. al.** *Intensity modulated proton therapy: A clinical example.* s.l. : The International Journal of Medical Physics, Research and Practice, 2001. 28:317.

[34]. **K. Mertens, et al.** *In Vitro 2-Deoxy-2-[18F]Fluoro-D-Glucose Uptake:.* 2012.

[35]. **Warburg, Otto.** *On the origin of cancer cells.* s.l. : American Association for the Advancement of Science, 1956.

[36]. **Jeffrey A Fessler, John M Ollinger.** s.l. : IEEE SIGNAL PROCESSING MAGAZINE, 1997. 97:1053-5888.

[37]. **Saha, Gopal B.** *Basics of PET Imaging, Physics, Chemistry and Regulations.* s.l. : Springer, 2005.

[38]. **D. W. Townsend, et. al.** *A Rotating PET Scanner Using BOO Block Detectors: Design, Performance and Applications.* s.l. : The Journal of Nuclear Medicine, 1993. 34:1367-1376.

[39]. **Mikhail Korzhik, Andrei Fedorov, Alexander Annenkov, Andrei Borissevitch, Alexei Dossovitski, Oleg Missevitch, Paul Lecoq.** *Development of scintillation materials for PET scanners.* s.l. : NuclearInstruments and Methods in Physics Research, 2006. 571: 122-125.

[40]. **Lars-Eric A., et. al.** *Performance of a Whole-Body PET Scanner Using Curve-Plate NaI(Tl) Detectors.* s.l. : The Journal of Nuclear Medicine, 2001. 42:1821-1830.

[41]. University of Washington. [Online] [Cited: 30 March 2016.] http://depts.washington.edu/nucmed/IRL/pet_intro/intro_src/section5.html.

[42]. **B. W. Jakoby, et al.** *Physical and clinical performance of the mCT.* s.l. : Phys. Med. Biol. 56 2375–2389, 2011.

[43]. **T. Beyer, et al.** *A combined PET/CT Scanner for Clincal Oncoloy.* s.l. : J Nucl Med; 41:1369-1379, 2000.

[44]. **D. L. Bailey, D. W. Townsend, P. E. Valk and M. N. Maisey.** *Positron Emission Tomography Basic Sciences.* s.l. : Springer London, 2005.

[45]. **K. Parodi, et. al.** *PET/CT imaging for treatment verification after proton therapy: A study with plastic phantoms and metallic implants.* s.l. : American Association of Physicists in Medicine, 2007. 34: 419.

[46]. **M. Moteabbed, S. Espana, H. Paganetti.** *Monte Carlo patient study on the comparison of prompt gamma and PET imaging for range verification in proton therapy.* s.l. : Physics in Medicine and Biology, 2011. 56: 1063-1082.

[47]. **K. Parodi, T. Bortfeld.** *A filtering approach based on Gaussian–powerlaw.* s.l. : Physics in Medicine and Biology convolutions for local PET verification of proton radiotherapy, 2006. 51: 1991-2009.

[48]. **F. Attanasi, et. al.** *Extension and validation of an analytical model for in vivo PET verification of proton therapy—a phantom and clinical study.* s.l. : Physics in Medicine and Biology, 2011. 56: 5079-5098.

[49]. **K. Parodi, et. al.** *PET imaging for treatment verification of ion therapy: Implementation and experience at GSI Darmstadt and MGH Boston.* s.l. : Nuclear Instruments and Methods in Physics Research, 2007. 591: 282-286.

[50]. **K. Parodi, W. Enghardt, T. Haberer.** *In-beam PET measurements of β+ radioactivity induced by proton beams.* s.l. : Physics in Medicine and Biology, 2001. 47:21-36.

[51]. **Georgy Shakirin, et. al.** *Implementation and workflow for PET monitoring of therapeutic ion irradiation: a comparison of in-beam,in-room, and off-line techniques.* s.l. : Physics in Medicine and Biology, 2011. 56:1281–1298.

[52]. **W. Enghardt, et al.** *Charged hadron tumour therapy monitoring by means of PET.* s.l. : Nuclear Instruments and Methods in Physics Research, 2004.

[53]. **Linz, Ute.** *Ion Beam Therapy: Fundamentals, Technology, Clinical Applications.* s.l. : Springer Verlag, 2012.

[54]. **A. Tourovsky, et. al.** *Monte Carlo dose calculations for spot scanned proton therapy.* s.l. : Physics in Medicine and Biology, 2004. 50: 971-981.

[55]. **J. Herault, et. al.** *Monte Carlo simulation of a protontherapy platform devoted to ocular melanoma.* s.l. : Medical Physics, 2005. 32: 910.

[56]. **L. Grevillot, et. al.** *A Monte Carlo pencil beam scanning model for proton treatment plan simulation using GATE/GEANT4.* s.l. : Physics in Medicine and Biology, 2011. 56: 5203-5219.

[57]. **Paganetti, H.** *Range uncertainties in proton therapy and the role of Monte Carlo simulations.* s.l. : Ohysics in Medicine and Biology, 2012. 57: R99-R117.

[58]. **Teiji Nishio, et. al.** *The development and clincal use of a beam on-line PET system mounted on a rotating ganty port in proton therapy.* s.l. : Int. J. of Radiation Oncology, Biology and Physics, 2010. 277-286.

[59]. **Shakirin G., et. al.** *Implementation and workflow for PET monitoring oftherapeutic ion irradiation: a comparison of in-beam,in-room, and off-line techniques.* s.l. : Physics in Medicine and Biology, 2011. 56:1281-1298.

[60]. **Stephanie E. Combs, et. al.** *Heidelberg Ion Therapy Center (HIT): Initial clinical experience in the first 80 patients.* s.l. : Acta Oncologica, 2010.

[61]. Heidelberg Ion-Beam Therapy Center (HIT), Universitätsklinikum Heidelberg. [Online] [Cited: 03 05 2016.] https://www.klinikum.uni-heidelberg.de/About-us.124447.0.html?&L=1.

[62]. **Linz, Ute.** *Ion Beam Therapy. Fundamentals, Technology, Clinical Applications.* s.l. : Springer, 2012.

[63]. **J. Bauer, et. al.** *Implementation and initial clinical experience of offline PET/CT-based verification of scanned carbon ion treatment.* s.l. : Radiotherapy and Oncology, 2013. 107:218-226.

[64]. **K. Noda, et. al.** *New treatment facility for heavy-ion cancer therapy at HIMAC.* s.l. : Nuclear Instruments and Methods in Physics Research, 2008. B 266;2182-2185.

[65]. National Institute of Radiological Sciences. [Online] [Cited: 03 05 2016.] http://www.nirs.go.jp/ENG/core/cpt/cpt01.shtml.

[66]. **S. Surti, et. al.** *Design study of an in situ PET scanner for use in proton beam therapy.* s.l. : Physics in Medicine and Biology, 2011. 56:2667-2685.

[67]. TU-Darmstadt. [Online] [Cited: 22 11 2017.] https://www.tu-darmstadt.de/universitaet/selbstverstaendnis/profil_geschichte/kooperation/thema_kooperation_k01.de.jsp.

[68]. GSI. [Online] [Cited: 22 11 2017.] https://www.gsi.de/forschungbeschleuniger/forschung_ein_ueberblick/ionenstrahlen_im_kampf_gegen_krebs.htm.

[69]. **J. Pawelke, et. al.** *In-Beam PET Imaging for the Control of Heavy-Ion Tumour Therapy.* s.l. : IEEE Transaction on Nuclear Science, 1997. 10.1109/23.632694.

[70]. MedAustron. [Online] [Cited: 04 05 2016.] https://www.medaustron.at/en/irradiation-rooms.

[71]. TuWien. [Online] [Cited: 04 05 2016.] https://www.ac.tuwien.ac.at/2015/10/new-research-collaboration-with-medaustron/.

[72]. **H. Leeb, et. al.** International Atomc Energy Agency. [Online] [Cited: 04 05 2016.] http://www-pub.iaea.org/MTCD/publications/PDF/P1433_CD/datasets/papers/ap_ia-10.pdf.

[73]. **Maringer.** Hauptverband der Österreichischen Sozialversicherungsträger. [Online] [Cited: 04 05 2016.] http://www.erstattungskodex.at/portal27/portal/hvbportal/content/contentWindow?&contentid=10008.564558&action=b&cacheability=PAGE.

[74]. ETM Professional Control. [Online] [Cited: 04 05 2016.] http://www.etm.at/Fachartikel/PR_MedAustron_Autlook_1_2_2014.pdf.

[75]. **S. Jan, et. al.** *GATE V6: a major enhancement of the GATE simulation platform enabling modelling of CT and radiotherapy.* s.l. : Physics in Medicine and Biology, 2011. 56:881-901.

[76]. **S. Agostinelli, et. al.** *Geant4—a simulation toolkit.* s.l. : Nuclear Instruments and Methods in Physics Research, 2003. 506:250-303.

[77]. **S. Jan, et al.** *GATE: a simulation toolkit for PET and SPECT.* s.l. : Physics in Medicine and Biology, 2004. 49:4543-4561.

[78]. **Rouse, Margaret.** Techtarget. [Online] [Cited: 24 11 2016.] http://whatis.techtarget.com/definition/MATLAB.

[79]. **Benker, Hans.** *Mathematik mit MATLAB.* s.l. : Springer Veralg, 2000. ISBN 978-3-642-63540-3 .

[80]. **McAndrew, A.** *An introduction to digital image processing with MATLAB.* s.l. : Victoria University of Technology, School of Computer Science and Mathematics, 2004.

[81]. **Th. S. Rau, et. al.** *Vom seriellen Schliffbild zum DICOM-Datensatz. Hochdetaillierte 3D Bildgebung mikro-anatomischer Strukturen am Beispiel des*

humanen Innenohres. . Medizinische Hochschule Hannover, Klinik für Hals-, Nasen-, Ohrenheilkunde, Hannover, Deutschland : s.n., 2010.

[82]. The OpenGATE collaboration. [Online] [Cited: 1 12 2016.] http://wiki.opengatecollaboration.org/index.php/Users_Guide_V7.2:Cut_and_Variance_Reduction_Technics.

[83]. The OpenGATE collaboration. [Online] [Cited: 30 11 2016.] http://wiki.opengatecollaboration.org/index.php/Users_Guide_V7.2:Setting_up_the_physics.

[84]. Geant4. [Online] [Cited: 25 11 2016.] http://geant4.cern.ch/support/proc_mod_catalog/physics_lists/useCases.shtml.

[85]. The OpenGATE collaboration. [Online] [Cited: 1 12 2016.] http://wiki.opengatecollaboration.org/index.php/Users_Guide_V7.2:Readout_parameters_for_Radiotherapy_applications:_Actors.

[86]. **Siou-Yin Cai, et. al.** *Depth Dose Characteristics of Proton Beams within Therapeutic Energy Range Using the Particle Therapy Simulation Framework (PTSim) Monte Carlo Technique.* s.l. : Biomed. J., 2015. 38:408-413.

[87]. **S.B.Jiang, et.al.** *Removing the effect of statistical uncertainty on dose–volume histograms from Monte Carlo dose calculations.* s.l. : Physics in Medicine and Biology, 2000. 2151–2161.

[88]. **Jarlskog, C. Z.** *Monte Carlo simulation with Geant4 for verification of rotational total skin electron therapy (TSET).* s.l. : Clinical Sciences, Lund, 2005.

[89]. **K. Jabbari, et.al.** *A fast Monte Carlo code for proton transport in radiation therapy based on MCNPX.* s.l. : Journal of Medical Physics, 2014. 156–163.

[90]. **I. Pshenichnov, et. al.** *Distributions of positron-emitting nuclei in proton and carbon-ion therapy studied with GEANT4.* s.l. : Physics in Medicine and Biology, 2006. 6099-6112:51.

[91]. **Kraan, A. C.** *Range verification methods in particle therapy: underlying physics and Monte Carlo modeling.* s.l. : Frontiers in Oncology, 2015. 10.3389/fonc.2015.00150.

[92]. **M. Mashayekhi, et. al.** *Simulation of positron emitters for monitoring of dose distribution in proton therapy.* s.l. : Elsevier, 2016. 22:52-57.

[93]. **M. Studenski, et.al.** *Proton therapy dosimetry using positron emission tomography.* s.l. : World Journal of Radiology, 2010. 135–142.

[94]. **K. Grogg, et.al.** *Feasibility of Using Distal Endpoints for In-room PET Range Verification of Proton Therapy.* s.l. : IEEE, 2014. 3290–3297.

[95]. **Helmbrecht, S.** *On the feasibility of automatic detection of range deviations from in-beam PET data.* s.l. : Physics in Medicine and Biology, 2012. 1387–1397.

[96]. **Kuess, P.** *Using statistical measures for automated comparison of in-beam PET data.* s.l. : Physics in Medicine and Biology, 2012. 10.1118/1.4749962.

[97]. **S. Helmbrecht, et. al.** *Systematic analysis on the achievable accuracy of PT-PET PETthrough automated evaluation techniques.* s.l. : ZEMEDI, 2014. 10550.

[98]. **P. Kuess, et. al.** *Automated evaluation of setup errors in carbon ion therapy using PET: Feasibility study.* s.l. : American association of physicists in medicine, 2013. 10.1118/1.4829595.

[99]. **ENVISION.** *Status report on the Monte Carlo models actually available for hadron therapy calculations.* 2011. Envision-WP6 Report n.1.

[100]. **J. Bauer, et.al.** *An experimental approach to improve the Monte Carlo modelling of offline PET/CT-imaging of positron emitters induced by scanned proton beams.* s.l. : Physics in Medicine and Biology, 2013. 5193–5213.